Technische Universität München

Walther - Meissner - Institut für Tief - Temperaturforschung

Würth Elektronik eiSos GmbH & Co. KG

Superconducting Wireless Power Transfer at High Power Densities for Industrial Applications and Fast Battery Charging

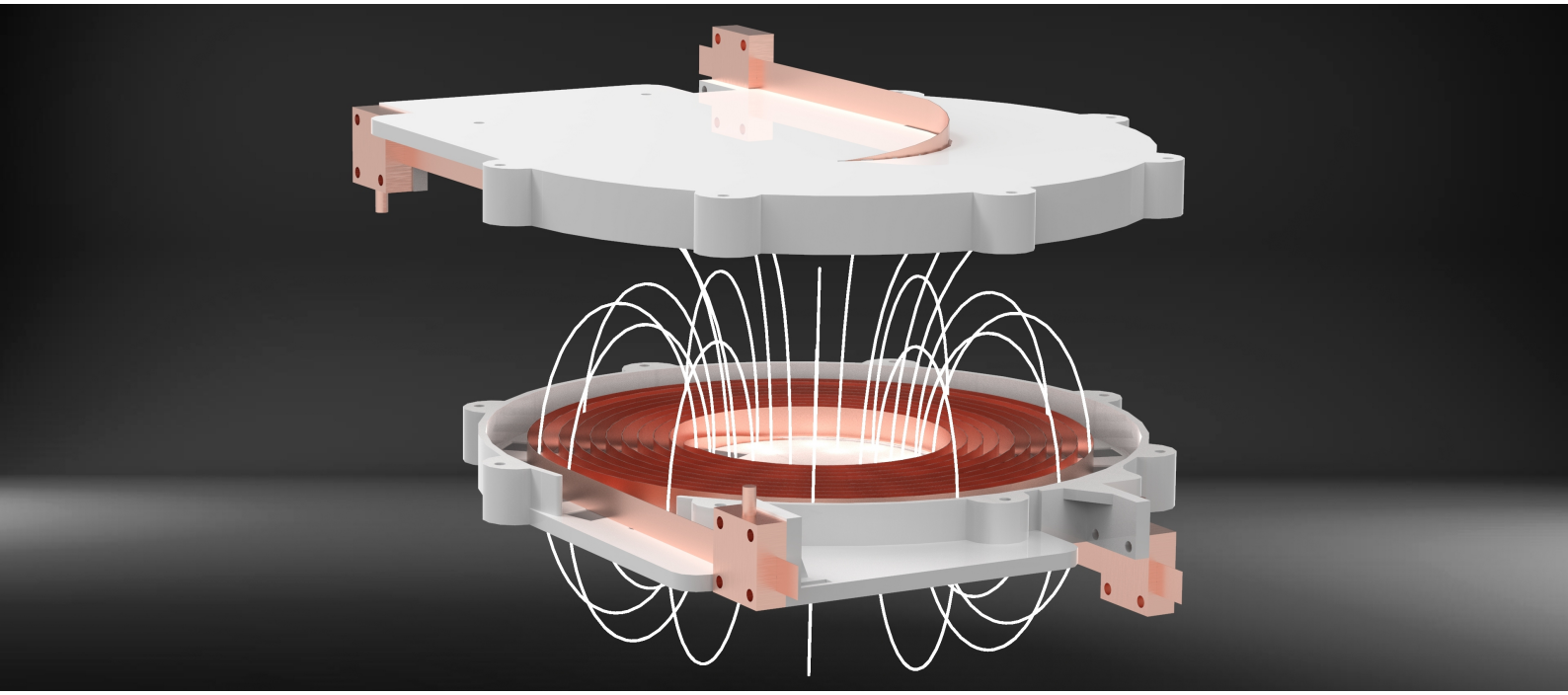

PhD Thesis

Christoph Utschick

Supervisor 1: Prof. Dr. Rudolf Gross
Supervisor 2: Dipl.-Ing. Cem Som

Munich, June 2021

Fakultät für Physik

TECHNISCHE UNIVERSITÄT MÜNCHEN

TECHNISCHE UNIVERSITÄT MÜNCHEN

Lehrstuhl E23 für Technische Physik

Walther-Meissner-Institut für Tieftemperaturforschung
der Bayerischen Akademie der Wissenschaften

Superconducting Wireless Power Transfer at High Power Densities for Industrial Applications and Fast Battery Charging

Christoph Utschick

Vollständiger Abdruck der von der Fakultät für Physik der Technischen Universität München zur Erlangung des akademischen Grades eines

Doktors der Naturwissenschaften

genehmigten Dissertation.

Vorsitzender:	Prof. Dr. Martin Zacharias
Prüfer der Dissertation:	1. Prof. Dr. Rudolf Gross
	2. Prof. Dr. Peter Böni

Die Dissertation wurde am 05.07.2021 bei der Technischen Universität München eingereicht und durch die Fakultät für Physik am 02.08.2021 angenommen.

"I do not hesitate to state [...] that flying machines and ships propelled by electricity transmitted without wire will have ceased to be a wonder in ten years from now. I would say five were it not that there is such a thing as 'inertia of human opinion' resisting revolutionary ideas."

Nikola Tesla, N.Y. World, May 1907

Abstract

With the rapid and continuously ongoing electrification of high power applications, wireless power transfer (WPT) systems have emerged as a key technology for the future charging infrastructure. Besides full system efficiency, the area- and weight-related power densities of the transmission coils are key figures of merit. This thesis presents the development, the optimization and the experimental verification of a fully functional WPT system, consisting of single pancake high-temperature superconducting (HTS) coils on the transmitter and the receiver side. Despite a compact coil size, a DC-to-DC efficiency above 97% is achieved at 6 kW output power. The proposed coil design exceeds the power density of most conventional systems and is a very promising candidate for further studies.

Kurzfassung

Mit der rasanten und stetig fortschreitenden Elektrifizierung von Hochleistungsanwendungen haben sich kontaktlose Energieübertragungssysteme als Schlüsseltechnologie für die zukünftige Ladeinfrastruktur etabliert. Neben der Gesamtsystemeffizienz sind die flächen- und gewichtsbezogenen Leistungsdichten der Übertragungsspulen wichtige Kenngrößen. In dieser Arbeit werden die Entwicklung, die Optimierung und die experimentelle Verifikation eines voll funktionsfähigen Energieübertragungssystems, bestehend aus hochtemperatur-supraleitenden Spulen auf der Sende- und Empfangsseite, vorgestellt. Dabei wird trotz einer kompakten Spulengröße bei 6 kW Ausgangsleistung ein DC/DC-Wirkungsgrad von über 97% erreicht. Mit dem vorgestellten Spulendesign wird die Leistungsdichte der meisten konventionellen Systeme übertroffen, was als sehr vielversprechender Ansatz für weitere Studien betrachtet werden kann.

Contents

Chapter 1

Introduction

More than 200 years after the invention of the combustion engine, an increased public interest in green energy and environmentally friendly technologies puts an end to the era of relentless fossil fuel consumption. Studies on global warming [1] ring the alarm. Our ecosystem is in a critical state and the increase of the global mean temperature can only be limited by an immediate reduction of the greenhouse gas emission. With a large and increasing share of renewable sources, the sector of energy generation is already on its way to become sustainable and climate neutral. The sectors of transportation, industry and agriculture, are however still dominated by combustion engines. In order to make use of the green electrical energy and to reduce the CO_2 footprint of these sectors, old machines and vehicles must be replaced by electrical ones. Initiated by political incentives [2], the automotive industry acts as a driver for new technologies. Car manufacturers have ramped up their e-mobility production at such a pace [3, 4], that the required charging infrastructure can hardly follow. In the year 2019, the world-wide stock of electric vehicles (EV) exceeded 7 millions [5]. With only 6.5 million private chargers and 850 thousand public chargers being in use in the same year [5], it became clear that significant improvements of the charging infrastructure are necessary to tackle the fundamental problem of e-mobility, the range anxiety [6]. But even in industrial environments, where enough charging points are available, the charging process itself can be a limiting factor for a general acceptance of battery powered electrical machines and vehicles. As the charging cables of high power applications are bulky, heavy and difficult to handle, the manual process of plugging them in can become an actual hurdle. Wireless power transfer (WPT) systems are in the position to simplify the charging process drastically and have therefore emerged as a key enabling technology to guarantee a high degree of machine availability [7]. They allow to charge electrical machines without the need for a physical connection cable or human interaction. Due to the simplicity of the charging process, WPT systems enable the approach of opportunity charging [8], where even short downtimes of an electrical machine are used efficiently and the charging level of the battery can be kept high throughout the day.

In the recent years, WPT systems have been studied extensively [9, 10] and many successful implementations have been reported for a broad range of applications and power classes. Starting from the wireless charging of smartphones and wearables at power levels of a few Watt, the technology has quickly matured and medium power solutions for household appliances and light

EVs have been realized [11, 12]. Car manufacturers have started to implement high power solutions into their premium segment and very recently, several WPT systems with power levels of a few 100 kW have been successfully installed on an electrical ferry and in electrical busses [13, 14]. Even charging levels of up to 500 kW have been announced for electrical drayage trucks [15]. These systems are user friendly, yield efficiencies well above 90 % and have demonstrated that the technology of WPT is not only a nice-to-have gadget, but that it is actually ready to replace conventional cable bound charging on a large scale.
Nevertheless, the area- and weight related power densities of state-of-the-art transmission coils are limited by a Pareto front where a reduction of size or weight leads to a decrease in efficiency [16]. Commercially available high power solutions are therefore large and heavy and are only applicable to heavy machinery. In order to enable WPT also for mobile electrical machines with strict limitations regarding weight and size, new approaches need to be investigated. With zero DC resistance and a very high current carrying capacity, superconducting wires are a promising candidate for high performance WPT coils [17–22]. However, the experimentally demonstrated power levels of less than 100 W [23–26] are still disappointingly low. This thesis presents the design and the operation of a WPT system with superconducting transmission coils on the transmitter and on the receiver side, and we demonstrate for the first time that such a system is able to transfer significant power levels in the kW regime at excellent efficiencies and at high power densities. Despite the fact that superconducting coils need to be cooled with cryogenic liquids, a successful application in industrial robots, autonomous transport vehicles and medical high-tech devices seems to be in reach soon.

As an introduction to the world of wireless power transmission, we present in the following subsection an overview of the already existing solutions in science and industry and we discuss the key figures of merit of these systems. In Sec. 1.2, we describe the design goals and the physical limitations of state-of-the-art systems. In Sec. 1.3, we motivate the application of superconducting transmission coils and we give the reader a first overview about the challenges that will be faced during the development. In Sec. 1.4, we present the outline of this thesis.

1.1 State of the Art - Existing Solutions in Science and Industry

In the recent years, many high power WPT systems in the kW regime have been designed and developed in academic projects. As the technology is mostly driven by the sector of e-mobility, the majority of the R&D activities focuses on static and dynamic charging of battery powered EVs. Many prototypes have demonstrated their functionality and have been tested under real-world conditions [27]. In order to compare the performance of different transmission coils, we introduce, in consistency with [28], three different power densities. The area-related power density α, the volume-related power density γ and the weight-related power density ρ, which relate the transferred power to the area, the volume and the weight of the receiver coil. We present the key parameters of the most significant R&D projects in Tab. 1.1. The results of the research teams from the Fraunhofer Institute for Solar Energy Systems ISE, the ETH Zürich and the ORN Laboratory are especially interesting, because all three of them have optimized their coil prototypes with the main objective of achieving a high power density. Despite the

fact that they have applied different coil geometries and different transmission frequencies, we observe that they have all achieved comparable power densities. Obviously, the η-α-Pareto front which has been found in [16] is valid, and limits the power density of WPT transmission coils. Based on the successful demonstration of high power WPT in laboratory environments, several companies have started to offer commercial products. The spectrum of the available solutions ranges from lower power levels of 3.7 kW, for slow overnight charging of private cars, to hundreds of kW for fast charging of heavy duty vehicles. In industrial environments, inductive charging stations for all types of electrical equipment, ranging from forklifts to autonomous transport vehicles, have been realized. Even a continuous power supply for a complete assembly-line was realized by embedding charging stripes into the floor [29]. We give an overview of commercially available solutions in Fig. 1.1 and present the key parameters of those systems next to the academic R&D projects in Tab. 1.1.

Academic R&D Projects

Institute	KAIST [30–32]	Fraunhofer ISE [33]	ETH Zürich [34]	ORN Laboratory [35, 36]
power per pickup (kW)	22	22	50	50
airgap (cm)	20.0	13.5	16.0	12.7
efficiency (%)	71.0	97.0	95.8	96.9
frequency (kHz)	20	100	85	22
coil area (cm^2)	rectangular 80×100	circular $\pi \cdot 30^2$	rectangular 41×76	double D 61×82
coil thickness (cm)	8.0	2.0	6.0	3.3
coil weight (kg)	80	11	25	52.6
α (kW/dm^2)	0.28	0.78	1.60	1.00
γ (kW/dm^3)	0.34	3.89	2.67	3.03
ρ (kW/kg)	0.28	2.00	2.00	0.95

Commercially Available Products

Company	BRUSA [37]	Wiferion [38]	Intis [39]	IPT Technology [13]
power per pickup (kW)	3.7	12	30	50
airgap (cm)	13	3	14	13
efficiency (%)	> 90	93	> 90	92
frequency (kHz)	85	n/a	20 - 90	n/a
coil area (cm^2)	33×28	37×32	88×86	110×108
coil thickness (cm)	2.5	2.0	2.5	5.5
coil weight (kg)	4	n/a	n/a	93
α (kW/dm^2)	0.4	1.01	0.40	0.42
γ (kW/dm^3)	1.6	5.06	1.58	0.77
ρ (kW/kg)	0.93	n/a	n/a	0.54

Table 1.1: Parameter overview of state-of-the-art high power WPT systems in academia and industry. Remark: The coil design of the ORN Laboratory was initially designed for 100 kW pick-up power. However, only 50 kW have been demonstrated experimentally in the cited reference.

BRUSA 3.7 kW [37]

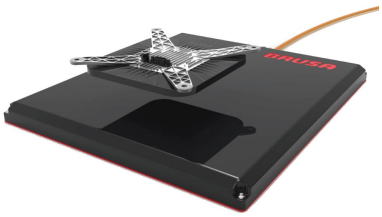

Conductix 6.6 kW [29]

Wiferion 12 kW [38]

INTIS 30 kW [39]

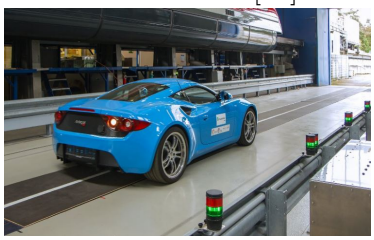

IPT Techn. 100 kW [13]

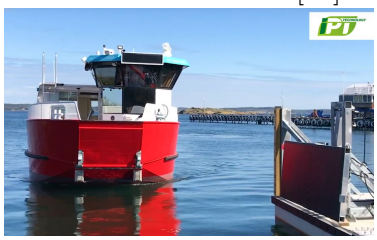

Momentum 200 kW [14]

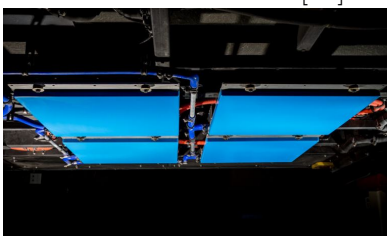

Figure 1.1: Overview of commercially available WPT solutions in the power range from 3.7 kW to 200 kW.

Tab. 1.1 shows that the power densities of commercial products remain far below the physical limits which have been found in academic projects. Mainly for the reason of reliability, commercial products are designed with a certain safety margin to keep the self-heating of the transmission coils and the required cooling measures to a minimum. The power densities of commercially available WPT coils remain below $\alpha \approx 0.5\,\mathrm{kW/dm^2}$, $\gamma \approx 1.6\,\mathrm{kW/dm^3}$ and $\rho \approx 1\,\mathrm{kW/kg}$. The 12 kW system, which was announced by Wiferion [38], seems to achieve high power densities of $\alpha = 1\,\mathrm{kW/dm^2}$ and $\gamma = 5\,\mathrm{kW/dm^3}$ at very small air gaps of 3 cm. An official data sheet is however not yet available and according to the manufacturer, field tests are still pending.
Besides the general limitation regarding the power density, state-of-the-art systems are also limited regarding the maximum amount of power that can be received by a single WPT module. For charging levels beyond 50 kW several pick-up modules need to be installed in parallel, which requires additional construction space and adds additional weight.

In order to provide a motivational use case scenario and to show the limitations of the conventional WPT technology, we discuss shortly the charging technology of an electrical Formula-E race car. According to the Fédération Internationale de l'Automobile (FIA) [40], the upcoming race car generation will include a cable bound ultra fast charging technology with a charging power of 500 kW. It will allow to recharge 4 kWh in only 30 seconds during a pit stop. If we consider to realize the same charging power with a currently available WPT system, we would need to install ten pick-up modules in parallel. In Fig. 1.2 we present the top-view of a Formula-E race car and indicate the size and the weight of a possible 500 kW WPT system. In (a), the scenario is calculated based on the parameters of the commercially available product from IPT Technology and in (b), it is calculated based on the parameters of the academic prototype from the ETH Zürich.
For the case of the commercially available product in Fig. 1.2 (a), we see that the scenario is totally unrealistic. The area and the weight of the receiver coils would exceed the area and the

weight of the car ($m_{\text{car}} = 780\,\text{kg}$ [40]). For the case of the academic prototype from the ETH Zürich in Fig. 1.2 (b), we see that the required coil area would fit below the body of the car. However, even for this fully optimized coil design, the cumulated mass of the receiver coils is still 250 kg, which corresponds to nearly a third of the total car mass and would therefore not be accepted as a suitable solution.

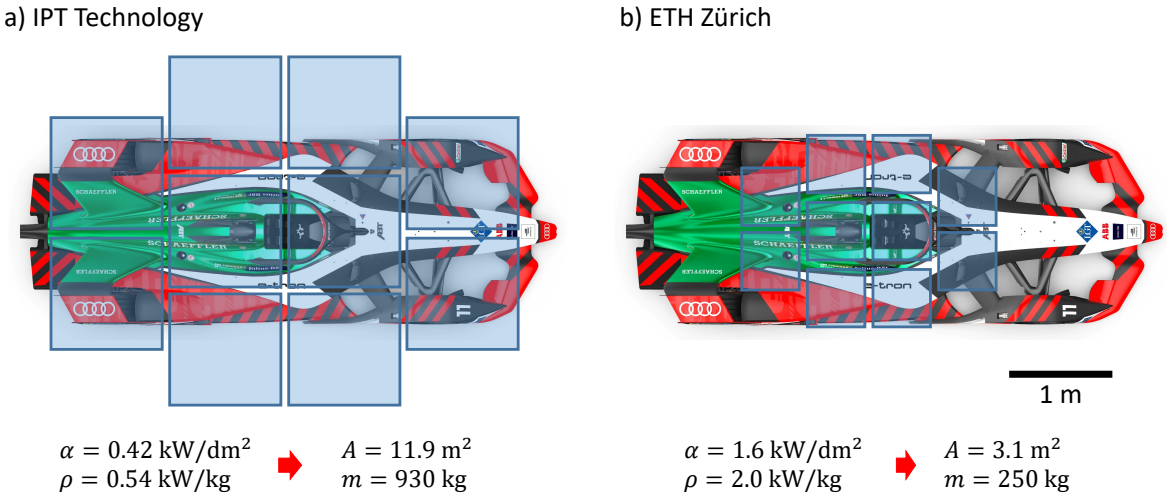

Figure 1.2: Use case scenario of a possible 500 kW WPT system for application in electrical Formula-E race cars. With state-of-the-art technology, ten pick-up modules must be installed in parallel. The area and the weight of the required pick-up modules is calculated based on the power densities of (a) a commercially available product [13] and (b) a fully optimized academic prototype [34]. With a cumulated coil weight of 250 kg, even the best case scenario would not be accepted as a suitable solution. Significant improvements of the power density are necessary to realize a successful application. The picture of the Formula-E race car is taken from [41], all dimensions are to scale.

This use case scenario shows clearly that the power density of the WPT coils must be significantly improved in order to realize a successful application of high power WPT system in high-tech areas, such as electrical race cars.

This thesis reports on a new system design, with superconducting transmission coils on the transmitter and the receiver side, which has demonstrated the successful power transfer of 6 kW at power densities of $\alpha = 1.59\,\text{kW/dm}^2$, $\rho = 5.71\,\text{kW/kg}$ and $\gamma = 7.95\,\text{kW/dm}^3$. The weight- and volume-related power densities exceed the best literature results by a factor of 2.8 and 2.0, respectively. The area-related power density exceeds all commercially available state-of-the-art systems and is comparable to the best literature value. These key figures have been obtained in the high-frequency regime, where the Q-factors of the superconducting transmission coils are reduced by eddy currents. Much better performance is expected in the low-frequency regime. The experimental verification at low frequencies remains, however, open for future work.

If our coil design proofs to be scalable to higher power levels, it would truly innovate the existing technology and would raise the performance of WPT systems to the next level.

1.2 Design Goals and Limitations of Conventional WPT Systems

In order to improve the power density of the WPT coils, we must first understand the design goals and the limitations of currently available systems. In general, WPT systems need to achieve two fundamental performance goals, a high efficiency and a high power density. Both performance goals depend on multiple design parameters, which have strong interdependencies to each other, and are therefore linked by a trade-off which is called η-α-Pareto front [16]. In the following, we review the limitations of inductively coupled WPT systems. The parameter interdependencies are visualized in Fig. 1.3.

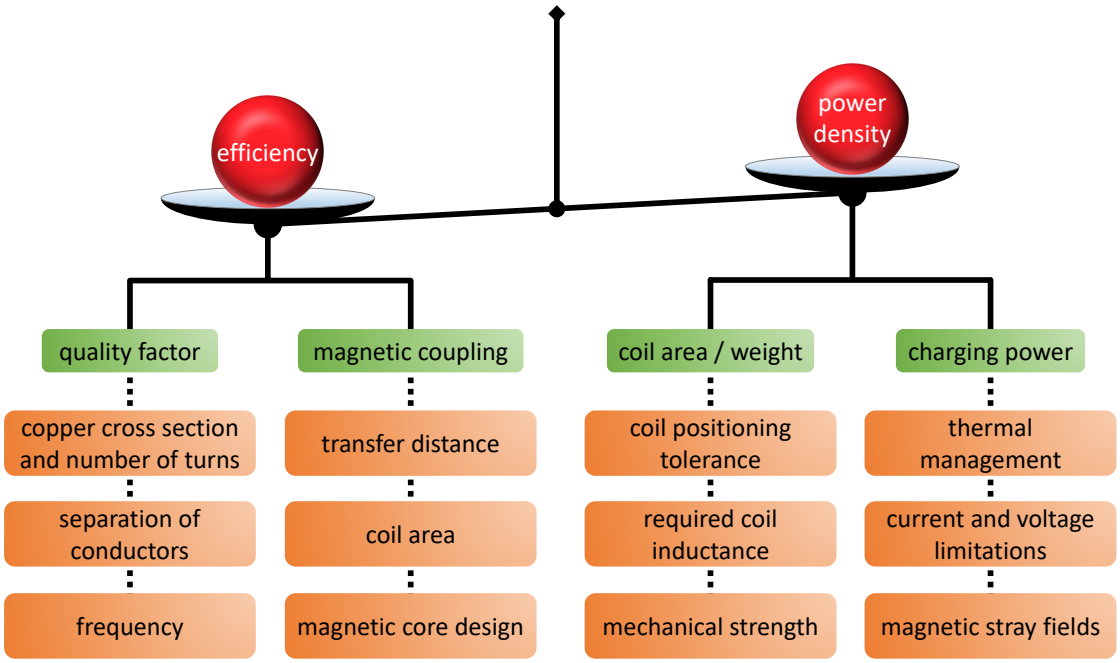

Figure 1.3: Fundamental performance goals and limitations of conventional WPT systems. The performance goals depend on multiple design parameters, which have strong interdependencies to each other, and are therefore linked by a trade-off which is called η-α-Pareto front [16]. The interdependencies are discussed in detail in the main text.

The first performance goal, a high efficiency of the WPT system, requires a well optimized coil design with high quality factor (Q-factor) and a strong magnetic coupling factor (κ) between the primary and the secondary coil.

- The Q-factor scales with $Q = \omega L / R_{\mathrm{AC}}$ and can be maximized by designing a coil with a large inductance L and a small AC resistance R_{AC}.
- The magnetic coupling factor scales with $\kappa = M / \sqrt{L_1 L_2}$ and can be maximized by designing a coil pair with a large mutual inductance M.

However, finding the best winding scheme for a given available winding space and a given required transmission distance is not straight forward. As the exact coil design depends on

multiple free design parameters, such as the inner- and the outer coil radius, the number of turns, the conductor cross section and the separation of the individual conductors, a sophisticated coil analysis is necessary.
Generally, best Q-factors can be obtained by filling the coil area from the outside towards the center with closely spaced copper conductors of large cross section [16]. Nevertheless, we have to consider that closely spaced conductors add a parasitic capacitance which lowers the self-resonance frequency of the coil and imposes an upper limit for the operating frequency [16]. If the available winding space is completely filled with copper and a higher inductance is still needed, a magnetic core can be used at the cost of a large increase in weight. As the additional AC loss in the core is small compared to the gain in inductance, a magnetic core increases the Q-factor in most cases.
Best coupling factors can be obtained by making the area of the coils as large as possible and by choosing an identical coil geometry on the primary and on the secondary side. The coupling factor can further be increased by applying a magnetic core to guide the magnetic flux. With increasing transmission distance, the mutual inductance however drops strongly and the influence of the magnetic core decreases. The requirement of achieving a certain coupling factor across a given air gap imposes a lower limit for the coil area.
We summarize that the first performance goal, achieving a high efficiency, requires large and heavy transmission coils.

The second performance goal, achieving a high power density, requires exactly the opposite. Large power levels must be transferred with coils of small size and low mass. As a reduction of coil size leads directly to a reduction of Q and κ, an increase in power density always goes along with a decrease in system efficiency. Even if the lower efficiency can be tolerated with regard to the energy cost, multiple challenges arise in the system design.
The coil area and the coil weight are limited by the following restrictions:

- Systems with a small coil area are less tolerant to coil misalignment. This is especially critical in applications where a perfect coil positioning cannot be guaranteed but a system failure is not tolerable.

- With decreasing coil size, the thermal management becomes increasingly challenging. The power loss, which is dissipated in the transmission coils, leads to self-heating of the coils and needs to be removed with a suitable cooling method. The thermal limit of WPT coils with forced-air convection cooling is typically reached at a surface related power loss density of $p_{\mathrm{surf}} = 0.2\,\mathrm{W/cm^2}$ [28]. The negative effect of a decrease in coil size is twofold. First, the power loss density increases because the power loss is simply dissipated in a smaller coil area. Second, the total power loss in the coils itself increases, because Q and κ of the coils decrease with decreasing coil size.

- In a small winding space, the required coil inductance can often only be achieved by introducing a winding scheme with multiple layers. Such a coil design suffers from enhanced proximity losses which additionally reduce the Q-factor.

- A reduction of the magnetic core volume and a removal of the shielding material allows

to reduce the coil weight but results in increased magnetic stray fields and can cause electromagnetic interference (EMI) problems.

- In order to obtain a sufficient mechanical strength, the reduction of the coil weight is further limited by the required weight of the housing and the fixtures.

Lastly, and most importantly, a WPT system can only reach a high power density if all the individual components of the power conversion chain are perfectly matched to each other. Due to strong parameter interdependencies between the coil inductance, the coupling factor and the operating frequency, even small variations of the system parameters can lead to a strong increase of the current or voltage levels. A WPT system in the high power regime is always designed for a specific application. Deviations from the anticipated design parameters result, in most cases, in a reduced charging power and in a reduced power density. This is especially critical, if the exact coupling strength and the best operating frequency are not known during the design phase.

1.3 Chances and Challenges of Superconducting Transmission Coils

A coil design that aims to overcome the η-α-Pareto front must realize a large coil inductance with a small AC resistance in a small winding space. Taking into account that state-of-the-art WPT coils already apply copper wires with an optimized litz structure, an improvement of the coil performance seems nearly impossible. Copper is highly conductive and the litz structure suppresses the high-frequency AC losses strongly. Since the discovery of superconductivity, however, new materials are available that exceed the current carrying capacity of copper by more than a factor of 200 [42]. As long as three critical parameters, the current density, the temperature and the external magnetic field, remain below their material specific values, a superconductor can transport electrical current with zero DC resistance, i.e. free of loss. Among all available superconductors, the so-called high-temperature superconductors (HTS) are most suitable for application in WPT systems. Their transition temperature is above 77 K and therefore a cheap cooling technique, based on liquid nitrogen, is sufficient to bring them into the superconducting state. HTS are fabricated as thin tapes and are commercially available in lengths of several 100 meters.
The promising approach of using these HTS tapes to improve the performance of WPT coils has been discussed in literature for more than 10 years [17–22]. The expected properties of superconducting coils are summarized in the following:

- The Q-factor of WPT coils scales with $Q \propto 1/R$ and diverges for $R \to 0$. When a superconducting winding with zero resistance is applied, the Q-factor is only limited by the remaining AC loss and can reach very large values.

- Typical HTS tapes have a thickness of only 0.1 mm and allow to realize foil windings with a very large power density in a small winding space.

- The current carrying capacity of the best-in-class HTS tapes exceeds 1000 A. With typical

system voltages of 600 V, charging powers of up to 600 kW can be expected. The technology could possibly even be scaled up to higher power levels by applying several tapes in parallel.

With such a high performance coil, most of the limitations of conventional WPT systems could be removed. In particular, the large Q-factors allow to avoid the sharp drop in efficiency, which normally comes along with a decrease of the coupling factor. A superconducting coil can compensate a weak coupling configuration with an increased current carrying capacity and nearly zero power losses. Due to the fact that the power losses in the coils are small, we can additionally expect that the power density is no longer limited by the problems of self-heating and heat removal.

Nevertheless, also for superconducting WPT coils, plenty of design challenges and parameter trade-offs need to be considered. Only a few research groups have published successful system designs [23–26] and none of them was able to transfer significant power levels beyond 100 W.

The fundamental challenges of superconducting transmission coils are the following:

- The current transport in superconductors is only free of loss under DC conditions. At AC frequencies, a fraction of the transmitted power is inevitably dissipated in the superconductor. Even though the AC loss is small and does not necessarily influence the system efficiency, it increases the surface temperature of the superconductor and can result in a breakdown of the superconducting state. As the AC loss increases with the current amplitude and with the frequency, the operation of superconducting coils at high frequencies and at high power levels is challenging.
- In commercially available HTS tapes, the superconducting layer is coated with several layers of normal conducting metals, which can cause eddy current losses [43]. Even though a few recent publications have studied the high-frequency AC loss in multi-layered HTS tapes [44–46], the exact loss behavior in the kHz regime is not yet fully understood.
- The superconducting layer in HTS tapes is very brittle and any mechanical stress during the fabrication or during a thermal cycle can lead to a local damage. Even the smallest damage can result in a local hotspot, which then expands into undamaged regions and leads to a breakdown of the superconducting state in the complete coil.
- The HTS coils need to be cooled permanently with cryogenic liquids like nitrogen. Even though, liquid nitrogen is available in cheap abundance, the practical realization of such a complicated cooling system might be an obstacle for a broad application. This is especially critical as the technology of WPT is generally considered to be free of maintenance. The requirement of regular access to a liquid nitrogen supply will only be accepted by the market if the performance of the superconducting system is truly outstanding compared to the conventional technique.
- In order not to distort the magnetic field between the transmitting and the receiving coil, the cryostats of both coils must be completely non-metallic. Such a cryostat design is currently not commercially available and will require significant engineering efforts.

- The market of WPT systems is strongly prize competitive. As the cost of HTS tapes is much larger than the cost of an equivalent copper wire and the required cooling system constitutes an additional investment, HTS coils are only suitable for leading edge technology in the areas of medicine and high-tech industry. Application in the sector of e-mobility for the charging of personal or public electrical cars seems rather unlikely.

This thesis investigates the performance of different HTS coil designs and tries to overcome the η-α-Pareto front of conventional systems, despite all the difficulties that must be solved.

1.4 Outline of this Thesis

The content of this thesis is structured into 9 chapters. In **Chap. 2** and **3**, we introduce the fundamentals of wireless power transfer and the fundamentals of superconductivity. Both chapters are intended to provide an easy access to these very special topics from the fields of electrical engineering and low temperature physics. In **Chap. 4**, we introduce and discuss the different loss mechanisms in copper wires and in HTS tapes. We introduce, for both conductor types, complete analytical models to calculate the AC losses under different working conditions. The analytical model allows us to clarify under which conditions the application of HTS tapes will be useful. In **Chap. 5**, we introduce and discuss the different loss mechanisms in ferromagnetic core materials. We focus on the properties of magnetically soft power ferrites and we discuss in detail their temperature dependence. With the aim of predicting the power loss in the core of superconducting WPT coils, we present an experimental low temperature characterization of one selected power ferrite. First, we introduce the experimental methods and then we present the obtained results. In **Chap. 6**, we design and optimize the superconducting WPT coils. We introduce the fundamental winding scheme of single pancake coils and we show how to maximize the quality factor in a limited winding space. We use two different calculation methods to determine the AC loss in the HTS winding and we find difficult parameter interdependencies between the coil inductance, the intertape spacing and the quality factor. Based on our results, we define two optimized coil designs for the operation of the WPT system at high- and at low-frequencies. In **Chap. 7**, we present the fabrication techniques, which have been applied to manufacture the superconducting WPT coils. In detail, we show how to fabricate single pancake coils with intertape spacing, and how to embed such coils into a potting compound. In **Chap. 8**, we present our experimental results. First, we characterize two of our fabricated coils under DC conditions, to verify that the fabrication process produces functional prototypes. Second, we measure the low-frequency AC loss and we verify that our loss calculations from Chap. 6 are correct. Finally, we apply the fabricated coils to our fully functional WPT system. With the main objective of demonstrating the transmission of high power levels at excellent efficiencies, we perform experiments with different coil designs, at different frequencies and at different load conditions. In **Chap. 9**, we summarize all results and give an outlook to further interesting research topics.

Chapter 2

Fundamentals of Wireless Power Transfer

The principle of using electro-magnetic fields to transmit electrical power without cables has been known since Nikola Teslas early experiments in the 19^{th} century [47]. Tesla demonstrated for the first time that energy can be transferred wirelessly across distances of several meters by applying high AC voltages to inductively coupled coils [48]. Based on his findings, he developed large scale experiments in the megavolt regime and he hoped to establish a worldwide wireless power distribution network, where power and information could be received at any point of the earth with very little power loss [47]. According to his theories [49], strong electromagnetic pulses from grounded Tesla-coils could excite field oscillations over large areas of the surface of the earth. His effort of building a large scale demonstrator, the famous Wardenclyffe Tower, was however never finished. Due to a lack of funding, the project was completely stopped in the year 1902 and Teslas (false) idea was abandoned. Since then, the technology of WPT has however matured and plenty of different transfer methods for every kind of possible application have been developed.
In this chapter, we introduce the fundamentals of wireless power transfer. In Sec. 2.1, we give an overview of the available WPT methods. In Sec. 2.2, we discuss shortly the importance of standardization and interoperability between different WPT systems. In Sec. 2.3, we review in detail the characteristics of an inductively coupled magnetic resonant system. In Sec. 2.4, we give an overview of the design and the operation principle of the power electronics and we estimate the losses in the semiconductor switches.

2.1 Introduction to Wireless Power Transfer

A WPT system transfers electrical energy from a transmitter to a receiver, without a physical connection cable. Besides for the obvious advantages of comfort and convenience, such a contactless system brings true innovation in plenty of use cases. The most significant reasons to implement WPT into an application are listed in the following.

- The receiving devices don't need plug sockets and can therefore be completely sealed, enabling enhanced water and dust protection.

- A WPT system does not contain any mechanical connectors. In conventionally charged devices these connectors are subject to wear and tear and are one of the most probable reasons for machine failure [50]. Frequent mating and un-mating results in erosion and corrosion of the electrical contacts and in physical wear-out of the connector shell, leading to an increased interface resistance, which further accelerates the degradation of the contact [51]. Therefore, the absence of mechanical connectors increases the lifetime and reduces the maintenance cost of electrical devices.
- The fact that WPT powered devices do not have open electrical contacts eliminates the risk of spark discharge, which allows operation in harsh environments where explosion hazards may exist.
- Expensive slip rings, which transfer power in rotating machines, can be replaced by a WPT system [52, 53].
- Magnetic levitation devices can be powered without any physical contact [54].

In the following, we give a short classification of different WPT systems.
First, we distinguish between stationary and dynamic WPT systems. In stationary systems, the receiving device is placed at a defined position on top of the charging unit and cannot be moved during the charging process. Such systems are especially favorable for electrical devices which have regular downtimes like consumer electronics, electrical tools, industrial machines and electrical vehicles. The required effort to build the necessary charging infrastructure for stationary WPT systems in private and public areas is relatively low.
In dynamic systems on the other hand, the receiving device is charged while moving. Such systems are mostly suitable for road- or rail-bound vehicles with a predefined regular travel route [7]. The financial effort to realize the infrastructure of large scale dynamic systems is very high and a feasibility study [55] has shown that dynamic charging is only reasonable in the case of low speed scenarios, where the amount of transmitted energy per meter of infrastructure is high. Furthermore, a large percentage of the travel route should be equipped with charging areas. Otherwise the amount of energy gathered in the charging area is small compared to the length of the travel route and the range of the vehicle would not be significantly extended. For the case of industrial machines inside factory buildings, e.g. automatic storage systems, assembly lines and elevators, a dynamic solution is in most cases beneficial and commercial solutions are available [29, 56].

Second, WPT systems can be classified according to their transmission range into far field and near field applications (compare Fig. 2.1). In far field systems, the power is transmitted across long distances of several meters by radiated fields at wavelengths ranging from the optical to the radio regime. Such systems can only be operated safely and efficiently, if the radiated power is focused into a beam and pointed towards the receiver. Recently, a solution based on infrared lasers [57] has demonstrated the ability of supplying hand-held devices like smartphones or laptops wirelessly with power levels of up to 2 W across distances of several meters. The major drawback of far field systems is, that a foreign object in the direct line of sight between transmitter and receiver might interrupt the power transfer and is exposed to the full amount of the radiated power. Thus, in order to keep the field exposure below the allowed limits [58], the

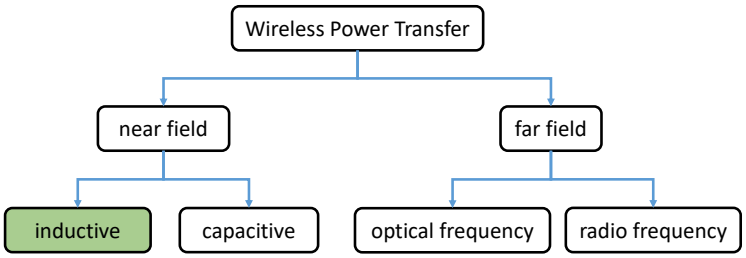

Figure 2.1: Classification of WPT systems according to their transmission range. This thesis is focused on the development of new coil designs for inductively coupled near field systems, because these systems have evolved as state-of-the-art for high power applications.

accessible power levels in far field systems are restricted to a few Watts.
In near field systems, on the other hand, the power is transmitted across distances of only a few centimeters. The transmitter and the receiver units are close to each other and foreign objects in the vicinity of the system are only exposed to the stray fields. Regarding the physical coupling mechanism in near field systems, we distinguish between inductive coupling, where coil windings are coupled by the B-field and capacitive coupling, where capacitor plates are coupled by the E-field. Capacitively coupled systems generally offer the advantage of better misalignment tolerance due to the non-canceling characteristics of the E-field compared to the B-field [7]. Further, electric stray fields do not create eddy current loss in foreign metallic objects, which weakens safety issues and simplifies the certification of the WPT system [7]. Nevertheless, the capacitive coupling mechanism is limited to very small airgaps of a few mm, even if large capacitor plates are applied. With inductive coupling, much larger transfer distances in the order of the coil radius can be achieved. Because a sufficiently large transmission distance is of great importance, the inductive coupling mechanism is therefore often preferred over other methods, and has evolved as state-of-the-art in the field of high power applications.

Taking the advantages and disadvantages of all methods into account, we have decided to focus in this thesis exclusively on inductively coupled near field systems. Such a system can in principle be realized stationary or dynamic. The physical principles and coupling mechanisms in both system types are very similar. Due to the fact that a large scale dynamic system is however difficult to realize in a lab environment, we restrict ourselves to the experimental verification of a stationary system.

2.2 Standardization and Interoperability

For a successful integration of WPT systems into the public charging infrastructure, standardization and interoperability are key challenges. WPT systems from different manufacturers must be compatible to each other and public charging points must be able to supply different power levels. Besides a generally defined transmission frequency and standardized spatial dimensions of the transmission coils, a broad interoperability requires also a standardized communication protocol

between the transmitting and the receiving device. As WPT is a relatively new technology, the process of standardization is still ongoing and several system designs compete to become the leading standard.
In the low power class of 5 - 15 W, the Qi-standard introduced by the Wireless Power Consortium (WPC) [59], seems to have made the race. With more than 600 board members and more than 7000 Qi-certified products, the interoperability between different chargers and smartphones is ensured. In the year 2019 more than 382 million WPT devices with Qi-certification have been shipped and the forecast predicts further growth [60]. A medium power standard for laptops and power tools with charging powers of 30 - 200 W [61] as well as a cordless kitchen standard for home appliances with charging powers of 100 - 2200 W [62] are currently in development.
For EV charging, the Society of Automotive Engineers (SAE) has defined the standard J2954 [63]. This standard introduces 4 power classes with charging levels of 3.7 kW, 7.7 kW, 11.1 kW and 22 kW. The working frequency must be in the range $81\,\text{kHz} < f < 90\,\text{kHz}$ and the efficiency must be $\eta > 80\,\%$. The communication is defined by the protocols J2836/6, J2847/6 and J2931/6.
Beyond 22 kW the currently existing industry solutions are proprietary and do not follow a standard. To close this gap and to accelerate the development of high power applications, the SAE works on a new standard J2954/2 [64], which is expected to define the specifications of heavy duty applications with charging levels of up to 500 kW.

As the physical behavior of superconducting coils differs strongly from the conventional technology, the best operating conditions of superconducting coils are most likely not within the limitations of the existing standard. Therefore, we allow ourselves to analyze the parameters of the new system design without any constraints regarding the coil geometry, the operating frequency or the magnetic field exposure limits. We generally expect that no interoperability between superconducting and normal conducting systems will be given. Nevertheless, a possible compliance with existing standards can be checked at a later stage, once a full understanding of the new technology has been obtained.

2.3 Inductively Coupled Magnetic Resonant WPT System

The equivalent circuit diagram of an inductively coupled magnetic resonant WPT system is very similar to the one of an isolated DC-DC transformer. In contrast to the transformer, the primary and the secondary inductance of the WPT system do however not share a common magnetic core. The transmission coils are separated by an air gap and are only weakly coupled. In the following, we introduce all components of the WPT system and discuss its fundamental characteristics. An overview of the complete system is depicted in Fig. 2.2.

The power conversion chain consists of the following devices. A DC source, which supplies the power from the 3-phase mains. A DC/AC inverter, which converts the DC voltage into an AC voltage. The primary and the secondary transmission coils with an inductance L_1 and L_2, an internal series resistance R_1 and R_2, a mutual inductance M and a coupling factor $\kappa = M/\sqrt{L_1 L_2}$, which transmit the power across the air gap. An AC/DC rectifier, which converts the AC

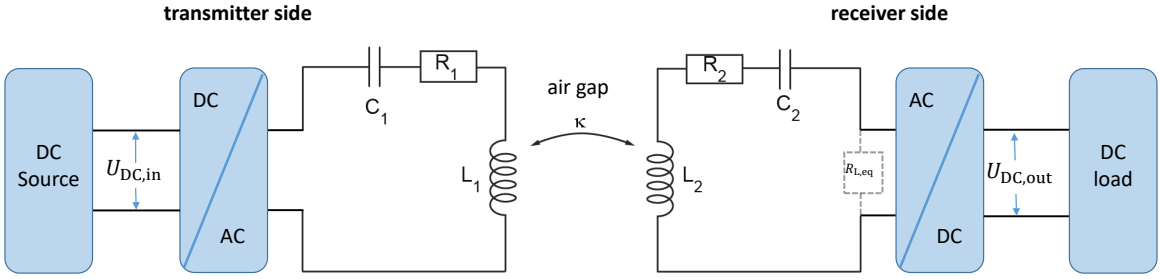

Figure 2.2: Overview of an inductively coupled magnetic resonant WPT system. The complete power conversion chain, including all components from the DC source to the DC load, is shown.

voltage back into a DC voltage and finally a DC load, with resistance R_L, which dissipates the transmitted power. As the DC load is positioned behind the rectifier, the circuit analysis can be simplified by introducing an equivalent resonant load with $R_\mathrm{L,eq} = 8R_\mathrm{L}/\pi^2$ [65]. The transmission coils are connected to resonance capacitors, C_1 and C_2 to form LC-resonators with identical resonance frequency f_r. The capacitors compensate the large leakage inductance and increase the efficiency of the system by introducing resonance phenomena. They can generally be connected in series or in parallel to L_1 and L_2. A series-series compensation scheme (as depicted in Fig. 2.2) offers the benefit that the resonance frequency does not shift with a change in load or magnetic coupling [66]. It further offers the highest efficiency during partial load conditions and is therefore preferred over other compensation schemes [66].

2.3.1 Current-Voltage Characteristics

The current-voltage characteristics of the WPT system are derived with a circuit analysis. By assuming an ideal voltage source with zero internal resistance, the impedances of the transmitter and the receiver side are

$$Z_1 = i\omega L_1 + \frac{1}{i\omega C_1} + R_1\,, \tag{2.1}$$

and

$$Z_2 = i\omega L_2 + \frac{1}{i\omega C_2} + R_2 + R_\mathrm{eq}\,. \tag{2.2}$$

Due to the magnetic coupling, a part of the receiver impedance is reflected back into the transmitter circuit, resulting in the input impedance [67]

$$Z_\mathrm{in} = Z_1 - \frac{Z_\mathrm{M}^2}{Z_2}\,, \tag{2.3}$$

where $Z_\mathrm{M} = i\omega M$ is the mutual impedance. With the input impedance being known, the input current on the transmitter side is given by

$$I_\mathrm{in} = \frac{U_\mathrm{DC,in}}{Z_\mathrm{in}}\,, \tag{2.4}$$

and the output current on the receiver side can be expressed as

$$I_{\mathrm{out}} = \frac{I_{\mathrm{in}} Z_{\mathrm{M}}}{Z_2} \,. \tag{2.5}$$

The voltage gain from the source to the load is then given by

$$|G| = \left| \frac{U_{\mathrm{DC,out}}}{U_{\mathrm{DC,in}}} \right| = \left| \frac{I_{\mathrm{out}} R_{\mathrm{L,eq}}}{U_{\mathrm{DC,in}}} \right| \,. \tag{2.6}$$

With this very simple set of equations, the system is fully described and we can study the current-voltage characteristics at different frequencies, load conditions and coupling factors. In Fig. 2.3, we show the voltage gain of an exemplary system with $L_1 = L_2 = 30\,\mu\mathrm{H}$, $C_1 = C_2 = 84.4\,\mathrm{nF}$ and $f_{\mathrm{r}} = 100\,\mathrm{kHz}$ as a function of the drive tone frequency. In 2.3 (a) the load resistance is varied at a fixed coupling factor $\kappa = 0.5$ and in 2.3 (b), the coupling factor is varied at a fixed load resistance $R_{\mathrm{L}} = 10\,\Omega$.

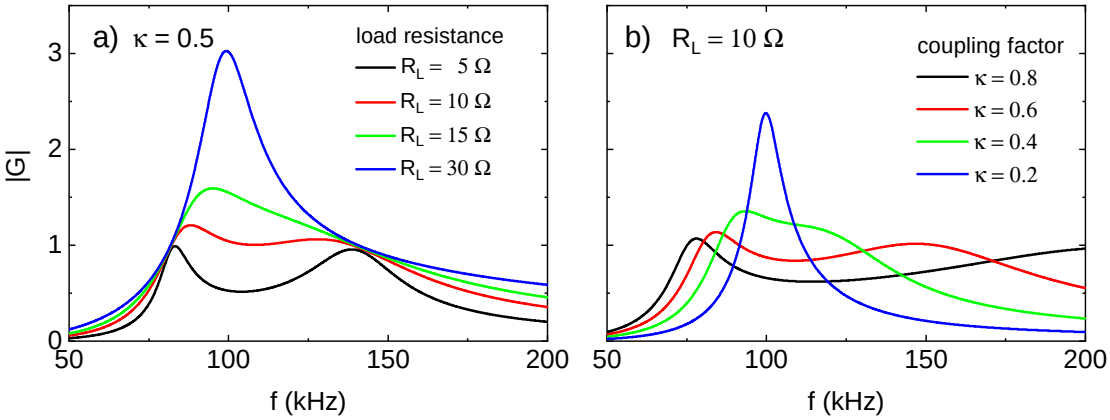

Figure 2.3: Voltage gain of an exemplary WPT system with $L_1 = L_2 = 30\,\mu\mathrm{H}$, $C_1 = C_2 = 84.4\,\mathrm{nF}$ and $f_{\mathrm{r}} = 100\,\mathrm{kHz}$ as a function of the drive tone frequency for (a) a coupling of $\kappa = 0.5$ at different load conditions and (b) a load resistance of $R_{\mathrm{L}} = 10\,\Omega$ at different coupling conditions. At a critical coupling condition we observe the onset of a pole splitting. Depending on the working point, even small variations of κ or R_{L} can lead to a large increase of the current or the voltage amplitude.

We observe that the single resonance peak of the weakly coupled system starts to separate into two individual peaks, if κ is increased beyond, or R_{L} is decreased below a critical value. This phenomenon is known as pole splitting in literature [68]. It appears in any type of coupled harmonic oscillators as soon as the coupling rate $\kappa\omega_{\mathrm{r}}$ exceeds the internal loss rate R/L of the coupled system. For the circuit depicted in Fig. 2.2, it can be shown [28] that the condition for an appearance of pole splitting depends on the load factor

$$\gamma = \frac{R_{\mathrm{L,eq}}}{\omega_{\mathrm{r}} L_2} \,. \tag{2.7}$$

If $\gamma > \kappa$, the system is under-coupled and no pole splitting is present. If $\gamma = \kappa$, the system is in the critical coupling state, where pole splitting starts to appear due to the interaction of the LC-resonators. If $\gamma < \kappa$, the system is over-coupled and strong pole splitting is present.
Due to this dependency, the voltage gain changes strongly with f, R_L and κ. In order to be able to operate the system at the desired voltage and current levels, the parameter interdependencies must be carefully considered during the system design. Furthermore, it becomes clear that an unintentional change of κ or R_L during operation, can result in a strong change of the current and voltage amplitude. Such a fault current must be avoided as it might damage the power electronics and the transmission coils.

2.3.2 Efficiency Characteristics

The efficiency limit of the WPT system, as depicted in Fig. 2.2, has been derived in Refs. [16, 69] and is reviewed in the following.
We generally assume that no metallic objects are in the direct vicinity of our system, so that the magnetic stray fields do not cause losses in the surroundings of the transmission coils. If we further neglect the power losses in the inverter and in the rectifier, then the system efficiency is only limited by the losses in the LC-resonators. As the conductive and the magnetic losses in L_1 and L_2 are typically much larger than the dielectric losses in C_1 and C_2, the quality factor of the LC-resonators is dominated by the transmission coils and is given by

$$Q_\mathrm{i} \approx 2\pi \times \frac{\text{stored energy}}{\text{energy loss per cycle}} = 2\pi \times \frac{L_\mathrm{i} I_\mathrm{rms}^2}{R_\mathrm{AC,i} I_\mathrm{rms}^2 / f_\mathrm{r}} = \frac{\omega_\mathrm{r} L_\mathrm{i}}{R_\mathrm{AC,i}}\,, \tag{2.8}$$

where i = 1,2 stands for the transmitter and the receiver side respectively, $R_\mathrm{AC,i}$ is the equivalent AC resistance of the coil, and $\omega_\mathrm{r} = 2\pi f_\mathrm{r}$ is the angular resonance frequency.
The loss factor, which relates the total power loss of both resonators to the output power, depends on Q_1, Q_2, κ and γ and is given by [69]

$$\lambda = \frac{P_\mathrm{loss}}{P_\mathrm{out}} = \frac{1}{\gamma Q_1 \kappa^2} \left(\gamma + \frac{1}{Q_2}\right)^2 + \frac{1}{\gamma Q_2}\,. \tag{2.9}$$

The transfer efficiency is given by

$$\eta = \frac{1}{1+\lambda}\,. \tag{2.10}$$

Derivation of η with respect to γ shows that the efficiency takes a maximum for one specific load condition [16]

$$\gamma_\mathrm{opt} = \frac{1}{Q_2}\sqrt{1 + \kappa^2 Q_1 Q_2} \approx \kappa\,, \tag{2.11}$$

where the approximation $\gamma_\mathrm{opt} \approx \kappa$ is valid if $Q_1 \approx Q_2$ and Q_1,$Q_2 \gg 1$.
With Eq. (2.7) we can write the optimum load condition as

$$R_\mathrm{L,eq} = \kappa \omega_\mathrm{r} L_2. \tag{2.12}$$

If Eq. (2.12) is satisfied, a perfect impedance matching between the source and the load is guaranteed and the WPT system is operated at the physically achievable efficiency maximum [16]

$$\eta_{\max} = \frac{\kappa^2 Q^2}{\left(1 + \sqrt{1+\kappa^2 Q^2}\right)^2} \approx 1 - \frac{2}{\kappa Q}\,, \tag{2.13}$$

where the system quality factor $Q = \sqrt{Q_1 Q_2}$ was introduced.
For a better understanding of the physical efficiency limit, we analyze the system performance for different values of Q. The best case scenario, where all materials are perfect and all losses are removed from the system, is modeled with a Q-factor of 10000. Conventional systems with copper coils are modeled with Q-factors ranging from 50 to 1000.
We plot $\eta_{\max}$ as a function of κ in Fig. 2.4 (a) and we see that η decreases strongly with decreasing κ. This is mainly due to the fact that larger coil currents are required to transmit the same amount of power if the coupling strength is reduced. With increasing current amplitude the losses in the transmission coils increase and the efficiency decreases.
In Fig. 2.4 (b), we plot η as a function of R_L for a fixed coupling factor of $\kappa = 0.5$. In this example with $\omega_\mathrm{r}/2\pi = 100\,\mathrm{kHz}$ and $L_2 = 30\,\mu\mathrm{H}$, the optimum load value is $R_{\mathrm{L,opt}} = 11.6\,\Omega$. As expected we see that η reaches $\eta_{\max}$ if $R_\mathrm{L} = R_{\mathrm{L,opt}}$ is satisfied, and that η decreases strongly if R_L is tuned away from its optimum value. This is mainly due to the fact that the impedance mismatch at non-optimum load condition results in reactive currents, which do not contribute to the power transfer but cause additional power losses in both transmission coils.
For sufficiently large Q-factors, however, both restrictions can be removed an η becomes nearly independent of κ and R_L. The Q-factor of the transmission coils is therefore the figure of merit for the performance of WPT systems and should be optimized.

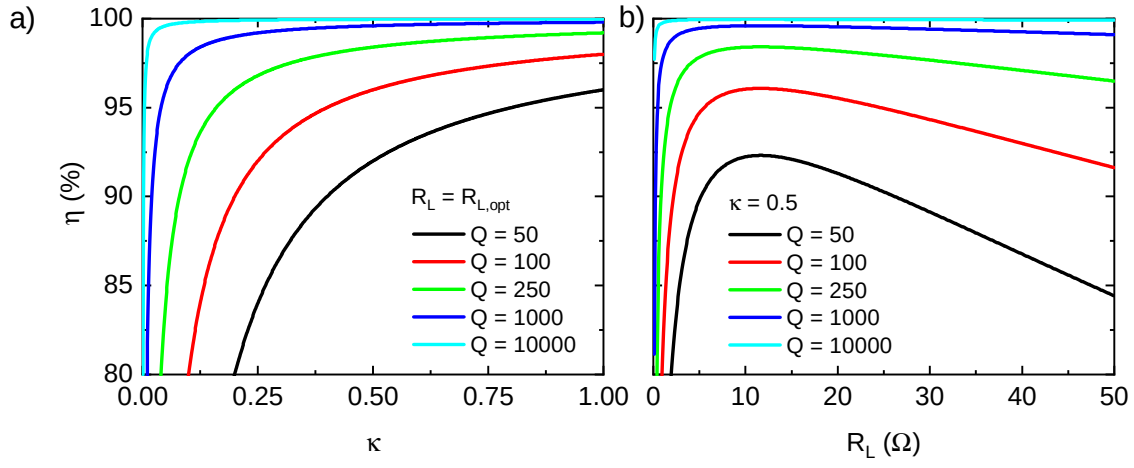

Figure 2.4: Efficiency analysis of an inductively coupled magnetic resonant WPT system under the assumption that the losses in the power electronics, in the resonant capacitors and in the system environment can be neglected. In (a), the physical efficiency limit $\eta_{\max}$ at the optimum load condition ($\gamma = \kappa$) is shown as a function of κ. In (b), η is shown as a function of R_L at a fixed coupling factor of $\kappa = 0.5$. The performance increase with increasing Q-factor can be observed in both subfigures.

2.3.3 Design Considerations for Optimum Efficiency Operation

Taking into account the current-voltage characteristics and the efficiency characteristics derived above, a design guideline for the inductance of the transmission coils L_1 and L_2 can be defined. We have seen that the load factor γ is the fundamental design parameter of the WPT system. In order to avoid frequency splitting, $\gamma \geq \kappa$ should be satisfied. At the same time, $\gamma = \kappa$ ensures perfect impedance matching and results in the highest efficiency. The secondary inductance should therefore be chosen according to [28]

$$L_2 = \frac{R_{\mathrm{L,eq}}}{\omega_{\mathrm{r}}\kappa}\,. \tag{2.14}$$

For a voltage gain of $|G| = 1$ at the nominal working point, the inductances of the transmitter and the receiver coil should be identical, i.e. $L_1 = L_2$.
Equation (2.14) introduces a complex parameter interdependency between the coupling strength, the load resistance, the operating frequency and the coil inductance. The load resistance $R_{\mathrm{L}} = U_{\mathrm{DC,out}}/I_{\mathrm{DC,out}}$ is fixed by the desired current and voltage amplitudes at the output and may differ from application to application, depending on the requirements. A reasonable choice of target parameters for an output power of 11 kW would be for example $U \approx 300\,\mathrm{V}$ and $I \approx 36\,\mathrm{A}$, which fixes the load resistance at the receiver side to $R_{\mathrm{L}} \approx 8.5\,\Omega$ ($R_{\mathrm{L,eq}} = 6.7\,\Omega$).
The coupling factor κ depends on the coil size and the transfer distance. Before being able to calculate the value of L_2 for a given application, the exact geometry of the transmitter and the receiver coils must be known and κ must be estimated with simulation tools.
With R_{L} and κ being fixed, Eq. (2.14) leaves a design trade-off between the frequency and the coil inductance. Low-frequency systems require a high coil inductance and vice-versa. In the design process of a conventional WPT system the working frequency is defined by the standardization and the choice of L_2 is straight forward. In the framework of this thesis, the dependency between the coil inductance and the working frequency poses however a large challenge. As the high frequency behavior of superconducting coils has not yet been studied in literature, the best working frequency is not known and it would be of great interest to test our coil prototypes in a broad range of frequencies. But, in order to keep the system in the working point with optimum efficiency, a change of ω_{r} requires a change of R_{L} or κ by the same factor. This means that a coil prototype is always fabricated for a specific nominal frequency and only small variations will be possible by adapting R_{L} and κ. Even if the current and voltage limitations of the power electronics would allow to change ω_{r} on a large scale, the results at different frequencies could hardly be compared to each other, because the losses in the superconducting transmission coils depend strongly on the current amplitude. So in order to compare the performance at different frequencies, while maintaining the current and voltage levels constant, we will fabricate and test two different pairs of superconducting coils in Chap. 7 and 8. We will build one pair of coils with a small inductance, for operation at high frequency and one pair of coils with a large inductance for operation at low frequency.

2.4 Power Electronics

Even though we intend to keep the focus of this work on the design and the experimental study of superconducting transmission coils, at least a minimum understanding of the involved power electronics is necessary to discuss the results of our WPT experiments. Therefore, we give in the following a short overview of the design and the operation principle of the inverter and the rectifier. Both devices have been built by the company Würth Elektronik eiSos and are based on silicon carbide (SiC) technology. They allow to operate our WPT system at power levels of up to 11 kW and at frequencies of up to 1 MHz.

2.4.1 Inverter

The inverter is based on an active full-bridge design with two discrete SiC MOSFET half-bridge modules (Infineon, FF11MR12W1M1P_B11), which have a voltage rating of $U_{\mathrm{DS}} = 1.2\,\mathrm{kV}$ and a current rating of $I_{\mathrm{DS}} = 100\,\mathrm{A}$. The DC input voltage is buffered by a bank of DC-link capacitors with a total capacitance of $C_{\mathrm{DC,link}} = 540\,\mu\mathrm{F}$. The current through the MOSFETs can be measured directly on the circuit board with a CKSR-50 current transducer. A photograph of the fabricated prototype, with the circuit board being mounted onto an aluminum heat sink, is shown in Fig. 2.5 (a).

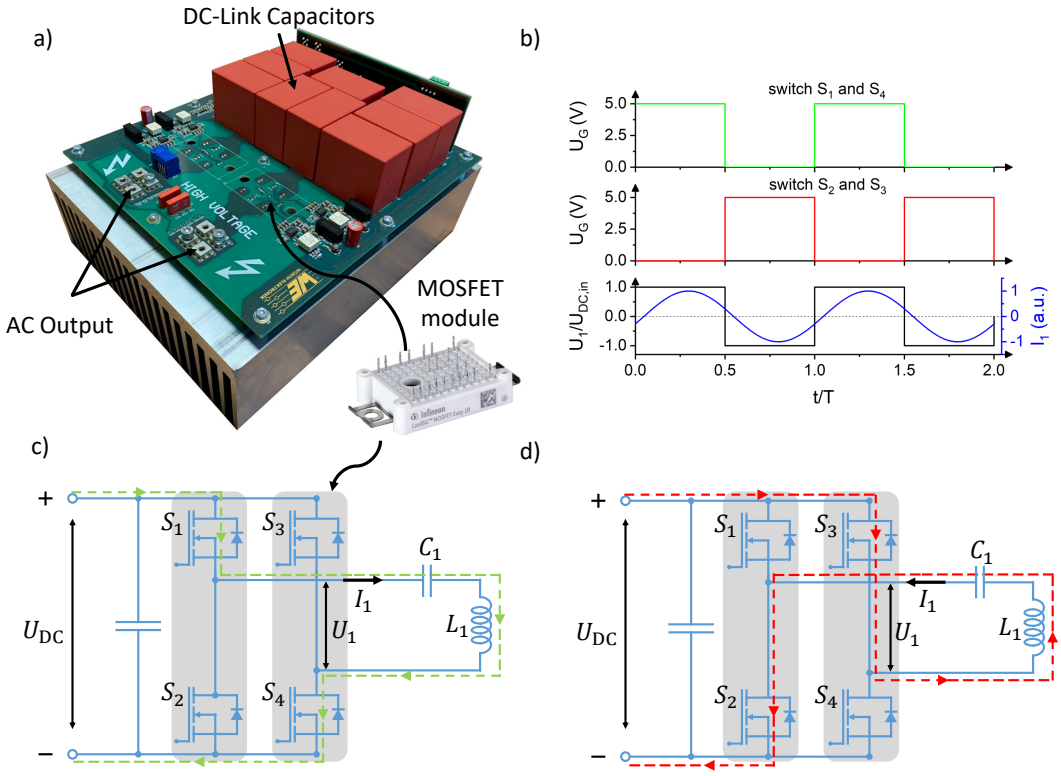

Figure 2.5: Overview of the design and the operating principle of the inverter module. A photograph of the fabricated prototype is shown in (a), the gate signals and the resulting current and voltage waveforms, U_1 and I_1, are shown in (b), the equivalent circuit diagram, including the current paths during the positive and the negative half-wave, are shown in (c) and (d), respectively.

The gate voltages for the MOSFET switches are supplied by an internally synchronized two-channel frequency generator. Channel 1 controls the switches S_1 and S_4, channel 2 controls the switches S_2 and S_3. Both channels generate rectangular voltage pulses with a phase difference of 180° at a duty cycle of 50 %. Due to the fact that the switch-off time of the MOSFETs is shorter than the switch-on time, a short deadtime is always given and the full-bridge is naturally protected against a short circuit. The resulting AC output voltage U_1 has a rectangular shape, with a peak to peak voltage of $2 \times U_{\mathrm{DC,in}}$. Due to the filter characteristics of the LC circuit, the resulting AC output current I_1 is approximately sinusoidal at the fundamental frequency. We show the gate signals and the resulting waveforms of U_1 and I_1 in Fig. 2.5 (b). The phase difference between U_1 and I_1 generally depends on the working point of the system. If the phase angle of Z_{in} is positive/negative, the input characteristics are inductive/capacitive and the current lags/leads the voltage. In order to minimize the switching losses in the MOSFETs, the output current should always lag the voltage. If such a lag is given, a small amount of positive current still flows through both bridge legs at the moment when the MOSFETs are switched. The remaining current charges the internal capacitances of the MOSFETs and is then taken over by the body diodes of the switches, which are about to be turned on. This allows that the switching takes place at zero voltage across the junction, i.e. at zero loss. For further details on zero-voltage switching (ZVS), we refer the reader to [28, 70, 71].
In our WPT system, a positive phase angle of Z_{in} requires two conditions [28]. The transmission coils must be weakly coupled so that no pole splitting is present ($\gamma > \kappa$) and the switching frequency must be above the resonance frequency of the LC-resonators ($f_{\mathrm{sw}} > f_{\mathrm{r}}$). Both conditions can be easily met.

Loss Approximation
The total loss in the inverter consists of switching losses and conduction losses. As we always operate the inverter under ZVS conditions, and due to the fact that the working frequencies in the kHz regime are relatively low, for SiC based semi-conductors, we assume that the switching losses are small compared to the conduction losses and neglect them.
The conduction losses in the inverter can be approximated by considering the current paths in the equivalent circuit diagram, as depicted in Fig. 2.5 (c) and (d). We see that during both half-waves, two MOSFETs are in the blocked state and two MOSFETs are simultaneously conducting. As the conduction resistance of a single MOSFET junction in the on-state is given by $R_{\mathrm{DS,on}} \approx 11.3\,\mathrm{m\Omega}$, the equivalent resistance of the complete inverter is given by $R_{\mathrm{inv}} = 2 \times R_{\mathrm{DS,on}} \approx 22.6\,\mathrm{m\Omega}$. The power loss in the inverter is given by

$$P_{\mathrm{loss,inv}} = I_1^2 R_{\mathrm{inv}}\,. \tag{2.15}$$

2.4.2 Rectifier

The rectifier is based on a passive diode bridge design, where each of the bridge elements is realized by four parallel SiC Schottky diodes (Infineon, IDW40G120C5B). Each of the diodes has two legs, which makes a total amount of eight parallel Schottky junctions per bridge element. The diodes have a voltage rating of $U_{\mathrm{DS}} = 1.2\,\mathrm{kV}$ and a current rating of $I_{\mathrm{DS}} = 110\,\mathrm{A}$ (55 A

per leg). The strong parallelization results in small current amplitudes through the individual junctions and intends to reduce the power loss. In order to obtain a smooth DC output, the rectified voltage is buffered by a bank of DC-Link capacitors with a total capacitance of $C_{\mathrm{DC,link}} = 300\,\mu\mathrm{F}$. A photograph of the fabricated prototype, with the circuit board being mounted onto an aluminum heat sink, is shown in Fig. 2.6 (a).

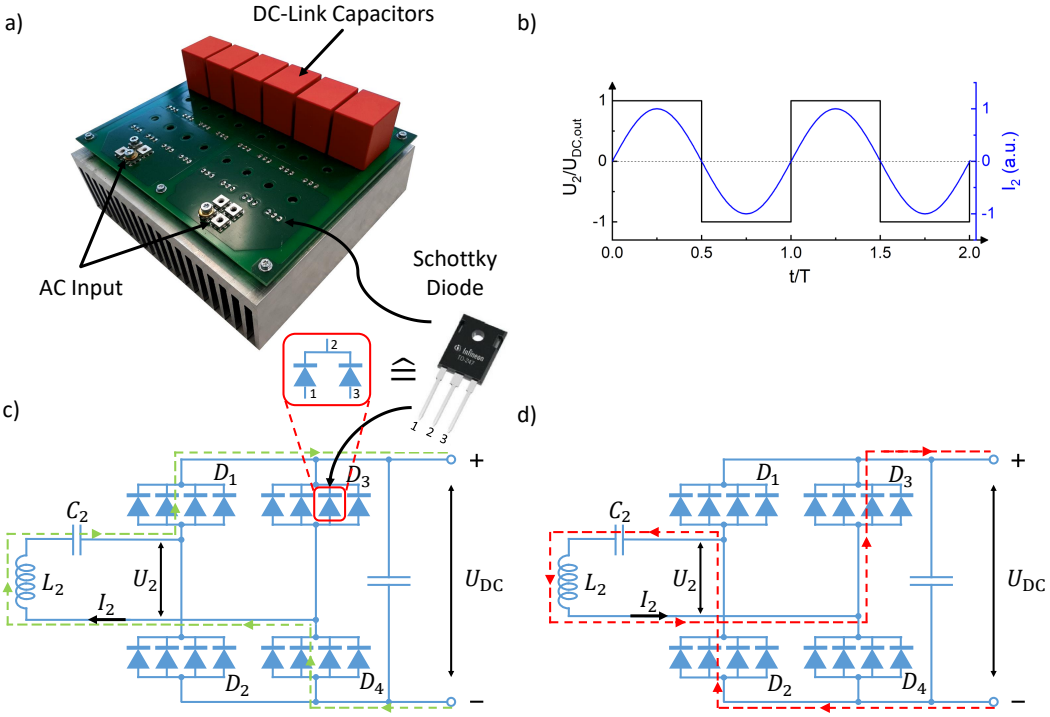

Figure 2.6: Overview of the design and the operating principle of the rectifier module. A photograph of the fabricated prototype is shown in (a), the current and voltage waveforms, U_2 and I_2, are shown in (b), the equivalent circuit diagram, including the current paths during the positive and the negative half-wave, are shown in (c) and (d), respectively. For better visibility, the Schottky diodes, which have two legs each, are represented by a single diode symbol. Therefore, four parallel diode symbols actually represent eight parallel diode junctions.

Identical to the transmitter side, the AC current I_2 in the receiver coil L_2 is approximately sinusoidal and the AC voltage U_2 is rectangular. Due to the fact that the diodes are passive elements, the switching occurs naturally at zero current and the phase difference between U_2 and I_2 is zero. The waveforms of U_2 and I_2 at the fundamental frequency are depicted in Fig. 2.6 (b).

Loss Approximation

Due to the fact that zero-current switching (ZCS) is always ensured in the rectifier, the switching losses in the diodes are small and can be neglected. We approximate the power loss by considering only the conduction loss through the diodes. The current paths, depicted in Fig. 2.6 (c) and (d) reveal that during both half-waves, two bridge elements are conducting and two are blocked. As each bridge element is realized by 8 parallel Schottky junctions, a total amount of 16 Schottky

junctions are conducting simultaneously and each of the junctions carries a current amplitude of $I_{\mathrm{DS}} = I_2/8$. In contrast to the MOSFET junctions, where the drain-source resistance in the on-state is constant, a diode has a strongly nonlinear current-voltage behavior. In order to calculate the power loss of the inverter as a function of the current I_2, we need to study the U-I-characteristics of the diodes in detail.
The forward current through a diode junction can be described with the Schockley equation [72]

$$I_{\mathrm{F}} = I_{\mathrm{s}} \left(e^{eU_{\mathrm{F}}/mk_{\mathrm{B}}T} - 1 \right) , \tag{2.16}$$

where U_{F} is the applied forward voltage, I_{s} is the reverse bias saturation current, $k_{\mathrm{B}}T/e$ is the thermal voltage and m is a correction factor which accounts for the fact that the diode behaves not ideal. In the conductive regime, where $eU_{\mathrm{F}} \gg k_{\mathrm{B}}T$, Eq. (2.16) can be simplified to $I_{\mathrm{F}} = I_{\mathrm{s}} \exp(eU_{\mathrm{F}}/mk_{\mathrm{B}}T)$. Solving for U_{F} gives $U_{\mathrm{F}} = mk_{\mathrm{B}}T \ln(I_{\mathrm{F}}/I_{\mathrm{s}})/e$. Due to the fact that the current path through an actual diode also contains resistive elements, we add an ohmic loss contribution to the Schockley equation. The total forward voltage drop across the diode at a forward current I_{F} is then given by

$$U_{\mathrm{F}} = \frac{mk_{\mathrm{B}}T}{e} \ln\left(\frac{I_{\mathrm{F}}}{I_{\mathrm{s}}}\right) + R_{\mathrm{res}} I_{\mathrm{F}} \, . \tag{2.17}$$

In Fig. 2.7 (a), we show the U-I-characteristics of the Infineon IDW40G120C5B Schottky diode, obtained from the datasheet [73]. We fit the measurement data numerically with Eq. (2.17) and see that the fit agrees excellently with the data. The fit parameters are $m = 1.09$, $I_{\mathrm{s}} = 2.7 \cdot 10^{-15}\,\mathrm{A}$ and $R_{\mathrm{res}} = 21\,\mathrm{m\Omega}$.
With the voltage drop across the junction being known, we can calculate the power loss of a single junction $P_{\mathrm{loss}} = U_{\mathrm{F}} I_{\mathrm{F}}$. We plot the power loss as a function of the forward current in Fig. 2.7 (b) and we observe that we can distinguish two regimes.

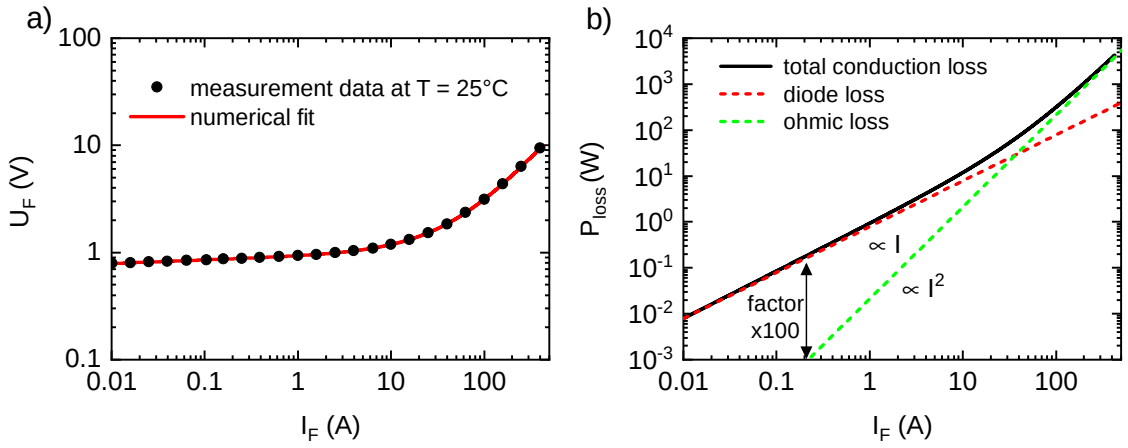

Figure 2.7: Characterization of the Schottky diodes. The subfigures show (a) the forward voltage drop, and (b) the power loss, across a single Schottky junction at $T = 25\,^{\circ}\mathrm{C}$. The black dots in (a) correspond to the measurement data, obtained from the datasheet [73]. The red line corresponds to the numerical fit according to Eq. (2.17). In (b), we see that the total conduction loss is dominated by diode losses at small current amplitudes and by ohmic losses at large current amplitudes.

At small current amplitudes ($I_\mathrm{F} < 20\,\mathrm{A}$), the total conduction loss is dominated by the voltage drop of the Schottky barrier and scales linearly with I_F. At large current amplitudes ($I_\mathrm{F} > 20\,\mathrm{A}$), the total conduction loss is dominated by ohmic losses and scales with I_F^2.
Considering the parallelization of the diodes, the power loss of the complete rectifier is given by

$$P_\mathrm{loss,rect} = 16 \cdot I_2/8 \cdot U_\mathrm{F}(I_2/8) = 2 I_2 U_\mathrm{F}(I_2/8)\,. \tag{2.18}$$

We see immediately that the parallelization of the diodes has practically no effect in the low current regime. As long as $I_2 < 20\,\mathrm{A}$, the approximation $U_\mathrm{F}(I_2/8) \approx U_\mathrm{F}(I_2)$ is valid and the power loss in a single junction is identical to the total power loss of eight parallel junctions. At current amplitudes $I_2 > 20\,\mathrm{A}$, where the rectifier is intended to be operated during WPT experiments, the parallelization is however necessary to reduce the ohmic loss and the design approach is reasonable. Nevertheless, for the case of a low current operation, e.g. during a frequency sweep or during a power sweep, we need to keep in mind that the Schottky barrier in the diodes dissipates up to a factor of 100 more power than the pure ohmic resistance in a MOSFET device.
We use Eq. (2.15) and (2.18), to evaluate and compare the power losses in the inverter and in the rectifier for two exemplary operating conditions.

- At low current amplitudes, the power loss in the rectifier is much larger than the power loss in the inverter and imposes an upper limit to the total system efficiency. At a working point with $I_2 = 3.6\,\mathrm{A}$, $U_\mathrm{DC,out} = 30\,\mathrm{V}$ and $P_\mathrm{out} = 110\,\mathrm{W}$, the power losses in the inverter and in the rectifier are given by $P_\mathrm{loss,inv} = 0.29\,\mathrm{W}$ and $P_\mathrm{loss,rect} = 6.5\,\mathrm{W}$. In this state, the losses in the power electronics account for 6 % of the transmitted power. Even if the transmission coils were completely free of loss, the efficiency of the WPT system would not exceed 94 %.

- At large current amplitudes, the losses in the inverter and in the rectifier become similar and are generally small compared to the transmitted power. At a working point with $I_2 = 36\,\mathrm{A}$, $U_\mathrm{DC,out} = 300\,\mathrm{V}$ and $P_\mathrm{out} = 11\,\mathrm{kW}$, the power losses in the inverter and in the rectifier are given by $P_\mathrm{loss,inv} = 29\,\mathrm{W}$ and $P_\mathrm{loss,rect} = 76\,\mathrm{W}$. In this state, the losses in the power electronics account for less than 1 % of the transmitted power. If the transmission coils were completely free of loss, the efficiency of the WPT system could actually exceed 99 %.

Chapter 3

Fundamentals of Superconductivity

In order to bridge the knowledge gap between electrical engineers and low temperature physicists, we introduce in the following the fundamental properties and the nomenclature of superconductivity. Hereby we restrict ourselves to the phenomenological model, which describes the behavior of superconducting materials correctly, without explaining the microscopic origin of superconductivity. We note that even though a microscopic model for type I superconductors has already been found in 1957 [74], the exact description of the microscopic mechanisms remains in some type II superconductors such as the high temperature cuprate superconductors still challenging.

In Sec. 3.1, we introduce the difference between type I, type II, low-temperature and high-temperature superconductors, and we present the most important superconducting materials and their applications. In Sec. 3.2, we introduce the fundamental equations to explain the macroscopic phenomenon of superconductivity and we discuss the mechanisms of current transport in type II superconductors. In Sec. 3.3 we introduce the properties of commercially available HTS tapes and discuss their magnetic field dependence. In Sec. 3.4, we give a short literature review of successfully developed superconducting large scale devices (rotating AC machines, transformers, fault current limiters, power cables). We will put special focus on the question, for what reasons, only very few of these fully developed superconducting devices are actively used in the power grid.

3.1 Introduction to Superconductivity

Superconductivity is a phenomenon that appears in certain materials when cooled below a characteristic critical temperature T_c typically well below room temperature. At T_c, a thermodynamic phase transition from the normal conducting into the superconducting (Meissner) state takes place. In this state, the electrical resistance is unmeasurably small and the sample is perfectly diamagnetic, expelling all magnetic flux from its volume. The Meissner state is not only limited by the critical temperature, it also breaks down above the material specific thermodynamic critical field B_c and above the material specific critical current density J_c. Above B_c, the work required by a superconductor for field expulsion exceeds the condensation energy

gained by entering the superconducting state. In the optimum case, the critical current density is given by the depairing current density, at which the kinetic energy of the charge carriers exceeds the condensation energy. However, there are various mechanisms reducing the critical current density well below this value.
Superconducting materials can be classified according to their field dependence into two types. In type I superconductors, the breakdown of superconductivity occurs abruptly when T, B or J reach its critical value. Type I materials show perfect conductivity and can carry persistent currents. The critical temperature T_c of type I materials is typically around a few Kelvin and the critical field B_c is around a few mT, which makes them unsuitable for power applications. Type I superconductivity is mostly found in elementary metals, e.g. aluminum, gallium, mercury or lead [72]. In type II superconductors, two critical fields $B_{c,1}$ and $B_{c,2}$ exist. Below $B_{c,1}$, type II materials behave identical to type I. Above $B_{c,1}$, however, for type II superconductors it is energetically more favorable to not fully expel the magnetic flux but to let it partly enter, forming a so-called mixed state where superconducting and normal conducting regions coexist. As part of the magnetic flux density can enter, the type II superconductor is saving flux expulsion work. It therefore can stay superconducting up to the upper critical field $B_{c,2}$ which can be much larger than the thermodynamic critical field B_c. With typical values of the upper critical field $B_{c,2}$ being in the order of several Tesla, type II superconductors are well suited for the use in power applications, where high magnetic fields and high transport currents are necessary. The most relevant groups of type II superconductors are metal alloys, like NbTi and Nb_3Sn, and complex oxide ceramics, which are known as cuprates [75].

Besides the classification of superconductors according to their field dependence, into type I and type II, they can also be classified according to their transition temperature T_c, into low temperature superconductors (LTS) and high-temperature superconductors (HTS).
As typical transition temperatures of LTS are below 20 K, expensive liquid helium cooling is necessary for those materials. Many LTS materials even exhibit transition temperatures below the boiling point of liquid helium, which requires complex cryogenic cooling technology. Therefore, LTS have only been established in a few power applications, where the use of superconductivity truly enables new technology. Since its discovery in 1961 [76], Nb_3Sn, which has a transition temperature of $T_c = 18\,\mathrm{K}$ and a current density of $J_c > 10^5 \mathrm{A/cm^2}$ at 8.8 T and 4.2 K, has emerged as state of the art for high field magnets in science and medicine [75]. It is produced industrially with a market share exceeding US$3 billion per year [75]. Besides those leading-edge technologies, however, LTS cannot compete with classical copper wires and are usually not applied in conventional power electronics.
In 1986, superconductivity was found in LaBaCuO at $T_c = 25\,\mathrm{K}$ [77], which led to the discovery of plenty of high-T_c cuprates. The most relevant HTS are YBaCuO and GdBaCuO with $T_c = 92\,\mathrm{K}$ [78, 79], BiSrCaCuO with $T_c = 105\,\mathrm{K}$ [80] and HgBaCaCuO with $T_c = 130\,\mathrm{K}$ [81]. We note that YBaCuO and GdBaCuO have very similar properties and are therefore often summarized under the acronym REBCO, where *RE* stands for the rare earth element (Y/Gd).
As the transition temperatures of these HTS are well above the boiling point of nitrogen, and liquid nitrogen is available in cheap abundance, the cooling cost is no longer the limiting factor for superconducting power applications. Consequently, since the discovery of HTS, many industrial

and scientific projects have explored the possibilities of replacing Cu and Fe by HTS in large scale devices. We will provide an overview of the most recent developments in Sec. 3.4. Nowadays, more than 10 different manufacturers worldwide, provide commercially available HTS tapes based on BiSrCaCuO (Bi-2223) or REBCO. Most of them are able to produce the tapes on length scales of hundreds of meters with critical current densities up to $J_c = 1\,\mathrm{kA/mm^2}$ at 77 K in self-field [42].

3.2 Macroscopic Description of Superconductivity

3.2.1 The London Equations

The phenomena of zero resistivity and perfect diamagnetism can be described macroscopically by the London equations [82]. Based on the Drude-theory for electrical transport, we start from the equation of motion for charge carriers under the action of an electrical field

$$m_\mathrm{s}\left(\frac{d}{dt}+\frac{1}{\tau}\right)\vec{v_\mathrm{s}} = q_\mathrm{s}\vec{E}\,, \tag{3.1}$$

where $m_\mathrm{s} = 2m_\mathrm{e}$, $q_\mathrm{s} = -2e$ and v_s are the mass, the charge and the velocity of a Cooper pair [83], respectively. We model perfect conductivity by using an infinite scattering time $\tau \to \infty$ (vanishing friction). We insert the general expression for the supercurrent density $J_\mathrm{s} = n_\mathrm{s} q_\mathrm{s} v_\mathrm{s}$, where $n_\mathrm{s} = n/2$ is the Cooper pair density, into Eq. (3.1) and find the first London equation [72]

$$\frac{\partial\left(\Lambda\vec{J_\mathrm{s}}\right)}{\partial t} = \vec{E}\,, \tag{3.2}$$

where the London coefficient $\Lambda = m_\mathrm{s}/(n_\mathrm{s}q_\mathrm{s}^2)$ was introduced. The first London equation relates the time derivative of the current to the electrical field. This shows that persistent currents can exist for zero electrical field. This is identical to the statement that the current transport in superconductors is free of loss.
The second London equation is found by inserting Eq. (3.2) into the Faraday law of induction. Together with the condition that the magnetic flux inside the superconducting volume is zero, we find [72]

$$\vec{\nabla}\times\left(\Lambda\vec{J_\mathrm{s}}\right)+\vec{B} = 0\,, \tag{3.3}$$

which relates the electric current to the magnetic field. By reformulating Eq. (3.3) we find [72]

$$\nabla^2\vec{B} = \frac{1}{\lambda_\mathrm{L}^2}\vec{B}\,, \tag{3.4}$$

where $\lambda_\mathrm{L} = \sqrt{m_\mathrm{s}/(\mu_0 n_\mathrm{s} q_\mathrm{s}^2)}$ is the London penetration depth, which typically ranges between 10 nm and 1 µm. Equation (3.4) is a characteristic shielding equation, which defines the length scale, on which magnetic field can penetrate into the superconductor. It shows that an external magnetic field is shielded by screening currents, which flow in a thin layer of thickness λ_L at the surface of the superconducting volume. The inside of the superconductor is free of both, current and field (Meissner-Ochsenfeld effect).

For type I superconductors above the thermodynamic critical field B_c, the field expulsion energy becomes larger than the condensation energy, which was gained in the phase transition from the normal conducting into the superconducting state. The superconducting state is no longer favorable in terms of energy minimization and consequently, it breaks down. We can relate a critical current density to the critical field by [72]

$$J_c = \frac{B_c}{\mu_0 \lambda_L} . \tag{3.5}$$

Both, the critical field and the critical current generally show a temperature dependence that can be described by the Gorter-Casimir-Model [72].

3.2.2 Current Transport in Type II Superconductors

Due to perfect flux expulsion, in type I superconductors the supercurrent flow is restricted to a thin surface layer of thickness λ_L, leading to a very small critical current of a technical conductor even at high critical current density of the superconducting material. In type II superconductors, magnetic flux starts to penetrate the superconducting volume in the form of periodically spaced flux vortices, if $B > B_{c,1}$. This state, where superconducting and normal conducting regions exist next to each other in the sample volume, is called mixed state. At $B_{c,2}$ all of the sample volume is penetrated by magnetic flux and the superconductivity breaks down. An exact determination of the lower and upper critical fields $B_{c,1}$ and $B_{c,2}$ requires a microscopic description and will not be discussed here. As $B_{c,2}$ of most conventional HTS tapes is in the order of 10 T, we can however assume that the magnetic fields, which are present in our WPT system, are $B_{c,1} < B \ll B_{c,2}$. Due to the penetration of flux vortices into the superconducting volume, the current flow is no longer restricted to a thin surface layer of thickness λ_L, which increases the current-carrying cross-sectional area and enables the transport of high currents [72].
Unfortunately, the presence of flux vortices also introduces a loss mechanism as shown in Fig. 3.1 (a). If a transport current density J_{tr} is applied to a type II superconductor in the mixed state, a Lorentz force acts on the flux lines, which results in a movement of flux lines with velocity v_L perpendicular to the applied current as soon as the Lorentz force exceeds a certain threshold [72]. According to

$$\vec{E} = \vec{B} \times \vec{v_L} , \tag{3.6}$$

the flux line movement causes an electric field parallel to the transport current, which in turn causes dissipation of energy [72]. In an ideal superconductor, which is free of point defects, the pinning force vanishes and the flux vortices are no longer bound to a specific position. In this case power dissipation sets in even at vanishing current amplitudes [84]. Therefore, ideal type II superconductors cannot carry persistent currents and are useless for applications. Lossless current transport can only exist if pinning centers are introduced into the superconducting volume. In such a pinning center, the condensation energy is reduced and the flux line is trapped in a potential well. The force which is required to remove a single flux line from its pinning center is called pinning force and defines the critical current that can be applied to the sample

[85]. A type II superconductor with strong pinning centers is called a hard superconductor [84]. The current-voltage characteristics of such a hard superconductor can be described by an empirical power law [86]

$$E = E_c \left(\frac{J}{J_c} \right)^n , \tag{3.7}$$

where $E_c = 1 \cdot 10^{-4}\,\mathrm{V/m}$ is the characteristic electric field, J_c is the critical current density and n is an empirical power exponent. We plot Eq. (3.7) in Fig. 3.1 (b) and discuss the different regimes of flux motion in the following.

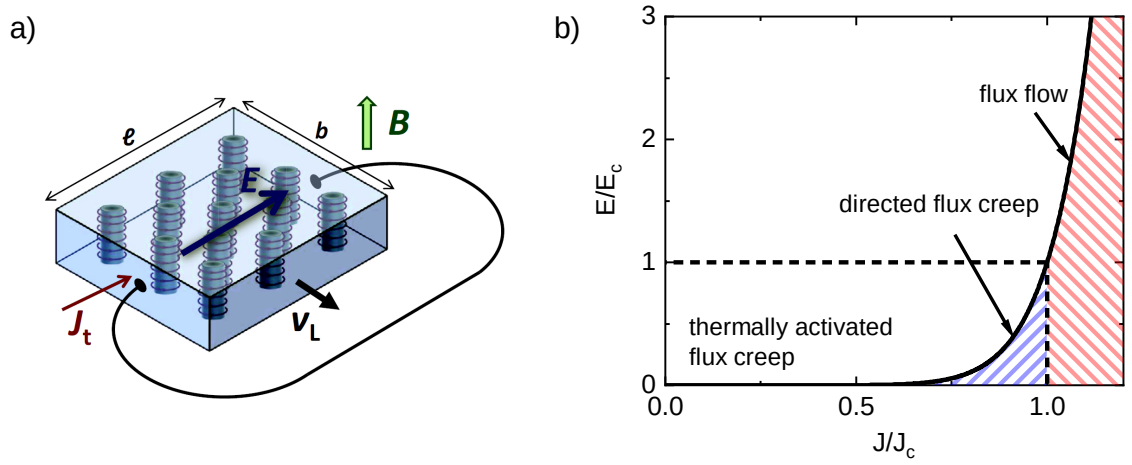

Figure 3.1: (a) Illustration of the formation of electric field in type II superconductors in the mixed state. Due to the Lorentz force, an applied transport current density $J_{tr} > J_c$ results in a flux flow perpendicular to J_{tr}. The movement of flux vortices results in an electrical field parallel to the current. Figure taken from [72]. (b) Current-Voltage characteristics of a technical hard superconductor. The different regimes of flux motion are indicated. Below J_c, the Lorentz force is small compared to the pinning force and flux vortices are bound to their pinning centers. Flux lines can only hop statistically from one pinning site to another due to thermal activation [84]. Above J_c the Lorentz force exceeds the pinning force and the flux lines begin to flow, resulting in large dissipation.

Below J_c, the Lorentz force is smaller than the pinning force and the flux vortices are bound to their pinning centers. Due to thermal activation, flux lines can hop statistically from one pinning site to another. This type of flux movement is called flux creep. It results in very small ohmic dissipation and is only relevant for persistent current applications [84]. With increasing current, the statistical flux creep gets directed, resulting in a voltage drop and significant power dissipation along the wire [84]. Above J_c the Lorentz force exceeds the pinning force and the flux lines begin to flow. In this regime, the large dissipation leads to heating of the superconductor and consequently to a breakdown of superconductivity (quench). For coils and magnets, which are operated at high currents, a quench inevitably leads to the destruction of the device and must be avoided.

The above discussion has shown that a movement of the flux lines results in energy dissipation. Under DC conditions, the flux lines are static and significant flow appears only if $J_{tr} > J_c$. Under

AC conditions however, the transport current and the magnetic field change periodically and the flux lines must adapt continuously to the externally imposed conditions. With this consideration it becomes clear that the movement of flux lines in AC applications causes significant power loss, even if $J_{tr} < J_c$. Due to the fact that the transmission coils in WPT systems are always operated under AC conditions, the minimization of the AC loss will be one of the main challenges in this thesis. We will discuss the AC loss mechanism in detail in Chap. 4.

3.3 HTS REBCO Tapes

Commercially available HTS are fabricated as thin and wide tapes. The tapes consist of a substrate, a very thin superconducting REBCO layer, a silver coating and an optional copper stabilization. A cross-sectional view of typical HTS tapes is depicted in Fig. 3.2.

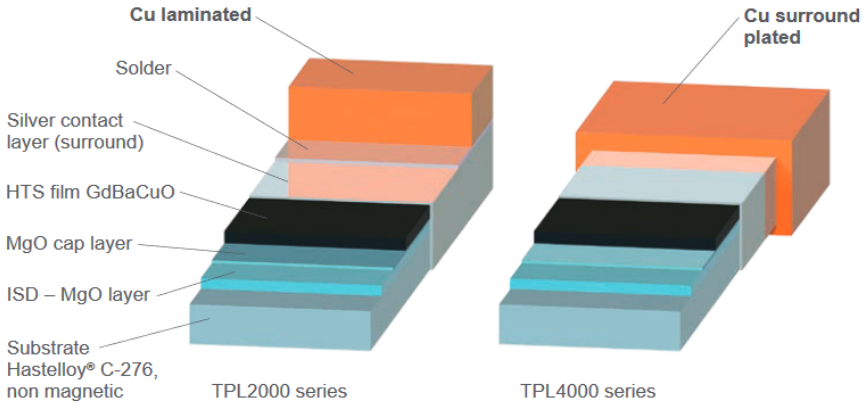

Figure 3.2: Cross sectional view of typical HTS REBCO tapes manufactured by Theva Dünnschichttechnik GmbH. The superconducting GdBaCuO layer is deposited onto a non magnetic substrate and coated by a protective silver layer. The optional copper stabilization is laminated on top of the tape or plated surround the tape. Figure taken from [87].

The exact manufacturing process to deposit the REBCO layer onto the substrate differs from supplier to supplier. Generally, the substrate needs to be polished and preprocessed with complex buffer layers. Then, the REBCO layer is grown on the substrate by electron beam evaporation (Theva), ion beam-assisted deposition (Bruker, SuperPower) or metal-organic deposition (American Superconductor).
REBCO tapes are considered as second generation (2G) HTS tapes, because they overcame many drawbacks of the first generation (1G) Bi-2223 tapes. The manufacturing cost was strongly reduced by minimizing the required amount of noble metals and by increasing the production throughput [88].
As the performance of the tapes from different manufacturers is very similar, we do not compare them against each other. All prototypes that will be presented in this thesis are built with tapes from the company Theva Dünnschichttechnik GmbH. We present the parameter range of the available Theva tapes in Tab. 3.1 [89].

Property	Formula Symbol	Value
Tape width	w	4 - 12 mm
Critical sheet current density at 77 K in self-field	J_c	up to 500 A/cm
Critical current at 77 K in self-field	$I_c = J_c w$	up to 600 A
Substrate thickness	t_{substr}	50 - 100 µm
HTS (GdBaCuO) thickness	t_{HTS}	≈ 3 µm
Silver coating	t_{Ag}	≈ 1.5 µm per side
Copper surround coating	t_{Cu}	0 - 20 µm per side
Copper lamination thickness	t_{Cu}	0 - 100 µm
Min. bending diameter	-	40 - 60 mm
Recommended max. handling force	-	50 - 100 N

Table 3.1: Parameter range of commercially available HTS tapes from the manufacturer Theva Dünnschichttechnik GmbH [89]. The critical current of thin HTS tapes is typically given as a critical sheet current density J_c in units of (A/cm). The critical current of a tape with width w is given by $I_c = J_c w$

In conventional DC applications, the choice of tape is straight forward. The width is chosen according to the required nominal current amplitude and the thickness of the stabilizer is chosen according to the expected maximum over-current. Under nominal operating conditions, i.e. DC current in the superconducting state, the copper layer has no negative influence on the performance of the tape and is therefore typically chosen as thick as possible. Under AC conditions, the situation is more tricky. Both, a large width and a thick metallic layer, can lead to significant AC loss. In order to chose the best tape for WPT coils, a detailed analysis of the loss mechanisms in different layers of the HTS tape is necessary. Considering the possibility that it might be necessary to remove the copper stabilizer for a successful application under AC conditions, we can already warn the reader that such a non-stabilized tape has no protection in the case of a quench. In the moment when the superconductivity breaks down, the current is forced to flow through the thin silver layer and causes an immediate and irreversible damage to the tape.

This is especially critical, because the superconducting REBCO layer is very brittle and it is likely that small defects appear if the tape is not handled very carefully. Even the smallest crack in the HTS layer, can reduce the local current carrying capacity and acts as a hot spot during operation. One single defect, on a tape length of hundreds of meters, can cause a quench of the complete device.

So clearly, the minimum bending diameter and the maximum handling force, which are defined by the manufacturer, should never be exceeded. First, this requires a fully optimized tape handling during the fabrication process of WPT coils. Second, mechanical stress and strain during thermal cycles must be avoided. Therefore, the thermal expansion coefficients of all materials must be matched to the thermal expansion of the tape. Otherwise the WPT coils might deform during the cool down and could be damaged before even the first test was performed.

All in all, the fabrication of functional WPT coils poses plenty of difficult engineering challenges that need to be solved. We will discuss the design and the fabrication process of our coil prototypes in detail in Chap. 6 and 7.

Magnetic Field Dependence of HTS REBCO Tapes

We have stated above that the critical current density in type II superconductors generally depends on the magnetic field strength. For the special case of HTS REBCO tapes, an additional dependency on the field angle is observed as these materials are anisotropic and the superconducting layer is grown with its ab-plane parallel to the tape surface. The current carrying capacity reaches its minimum if the externally applied field is perpendicular to the ab-planes of the crystal lattice.
If HTS tapes are used in a WPT application, they are exposed to the magnetic fields, which are generated by the primary and by the secondary coil. In order to be able to design the HTS windings appropriately, we need a precise knowledge of the field dependence of Theva tapes.

For 1G HTS tapes in an external magnetic field, the critical current density can be described by the modified 4-parameter Kim-model [90, 91]:

$$J_{\mathrm{c}}(B,\theta) = \frac{J_{\mathrm{c},0}}{\left(1 + \frac{B}{B_0}\sqrt{k^2 \sin^2\theta + \cos^2\theta}\right)^{\beta}}\,, \tag{3.8}$$

where $J_{\mathrm{c},0}$ is the critical current density at zero field, θ is the angle between the applied field and the surface of the tape, k is the anisotropy factor which accounts for the lattice structure and B_0 and β are material specific parameters.
For 2G HTS tapes, the simple 4 parameter equation does no longer model the behavior correctly, and expressions with more fitting parameters become necessary [92, 93].
Reference [94] shows an elegant way to fit an analytic equation to the actual behavior of a given tape. The method requires measurements of the field dependency in perpendicular ($J_{\mathrm{c},\perp}(B)$) and in parallel ($J_{\mathrm{c},\parallel}(B)$) field. Further, it requires the measurement of the normalized angle dependency at one fixed field amplitude $G(\theta)$.
The field dependence for arbitrary amplitudes and angles is then given by [94]

$$J_{\mathrm{c}}(B,\theta) = J_{\mathrm{c},\perp}(B) + G(\theta)(J_{\mathrm{c},\parallel}(B) - J_{\mathrm{c},\perp}(B))\,. \tag{3.9}$$

We apply this method to the measurement data of Theva tapes [95] and show the results in Fig. 3.3. Due to the fact that the ab-planes of the crystal structure are tilted by 30 degrees relative to the surface of the tape, the condition for parallel/perpendicular field is shifted to $\theta = 120°/\theta = 30°$. We see that the fit of Eq. (3.9) agrees reasonably with the experimental data and can therefore be used to estimate the reduction of the critical current in WPT coils.

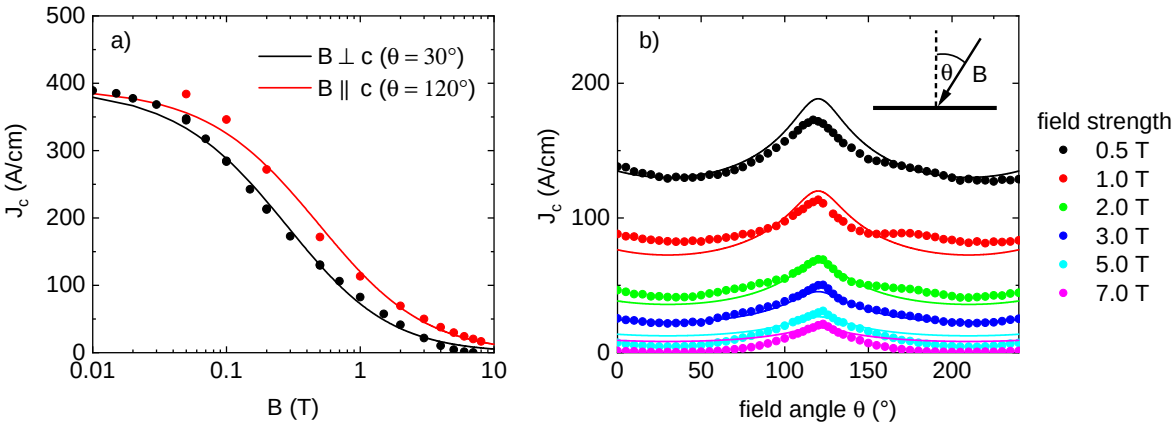

Figure 3.3: Magnetic field dependence of the critical current density of an HTS tape manufactured by Theva Dünnschichttechnik GmbH. The critical current density is shown in (a) as a function of the applied field strength for the limiting cases of perpendicular and parallel field angle, and in (b) as a function of the field angle for a set of different field strengths. The experimental data was obtained from the manufacturer upon request [95] and is fitted with Eq. (3.9) according to the method from [94]. The agreement of the fit with the measurement data is reasonable. Eq. (3.9) can therefore be used to estimate the reduction of the critical current in WPT coils.

3.4 State of the Art - Large Scale devices

Since the commercialization of HTS tapes, many efforts have been made to replace Cu and Fe in conventional power electronics applications. Plenty of large scale devices, including rotating AC machines (motors and generators), transformers, fault current limiters, power cables, high field magnets and magnetic levitation transportation systems have been developed successfully with outstanding properties, compared to their conventional counterparts in scientific and industrial projects [88]. Nevertheless, only few of them have been accepted by the market and HTS applications are not wide spread in the power grid. This is mainly due to the fact that the price of HTS tapes is far above the price of copper.
The challenge for manufacturers, to make HTS tapes competitive to copper, is a chicken-and-egg problem. High prices lead to little demand on the global market and little demand leads to small production volumes and hence high prices.
Ten years ago, in early predictions [96], the manufacturers expected to be able to bring the price per kAm (required amount of tape to transport a current of 1 kA along one meter) down to 20 € until the year 2020. However, recent reports [97] show that although the demand for HTS tapes has increased significantly and the manufacturers have ramped up their production and throughput, the decrease in price was not as strong as initially expected. The actual cost per kAm in the year 2019 was still around one order of magnitude above the expectation. Industry experts believe that HTS becomes competitive to copper if the price of HTS tapes drops below 10 €/kAm [88].

When a company like Würth Elektronik eiSos, which completely relies on conventional technologies, considers to invest into the development of superconducting devices, a profound knowledge of the market situation and a careful assessment of the future development is essential. Therefore

we present the state of the art of superconducting large scale devices and the most recent developments in the market in Tab. 3.2.

As we see in Tab. 3.2, the commercialization of 1G HTS tapes, beginning in the year 2000, resulted in the development of prototypes in all fields of power electronics. Due to price issues most companies withdrew their projects and the initial excitement about superconducting devices was lost after a few years. As nowadays, 2G HTS tapes start to reach an acceptable price level, HTS machines are again a hot topic and many projects have been started very recently. Supported by funding from the European Union, HTS technique has been successfully applied to wind turbines [93] and fault current limiters are on their way [97]. Furthermore the city of Munich has announced to build the worlds longest superconducting power transmission cable [98].
With those very recent success stories, we can expect that more projects will come up in the near future and that the price of HTS wire per kAm will continue to decrease.
We therefore conclude that although the price of HTS tapes cannot tackle the price of classical copper devices at the moment, industries should prepare prototypes in all fields of applications to have them in their portfolio, as soon as the price becomes competitive.

	device	source	year	power class
Rotating AC machines				
	synchronous generator	Siemens [99]	1999-2006	400 kW, 4 MW
	low speed generator	General Electric [100]	2004	100 MW
	ship propulsion motor	Naval research [88]	2007	36.5 MW
	high speed generator	General Electric [101]	2009	1.3 MW
	hydroelectric generator	Converteam [102]	2009	1.7 MW
	wind generator	EcoSwing (EU project) [93]	2019	3.6 MW
Transformers				
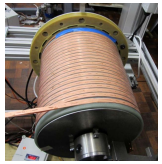	single phase transf.	Siemens [103]	2001	1 MW
	three phase transf.	Waukesha [104]	2004	10 MW
	three phase transf.	RRI New Zeeland [105]	2013	1 MW
Fault Current Limiters (FCL)				
	resistive FCL	Nexans [106]	2005	10 kV/10 MW
	resistive FCL	AMSC [107]	2012	115 kV
	saturated core FCL	InnoPower [108]	2012	220 kV/200 MW
	resistive FCL	FastGrid (EU project) [97]	2019	—
Power Cables				
	low voltage cable	ULTERA [109]	2006	13.2 kV/ 3 kA
	medium voltage cable	SuperPower/Sumitomo [110]	2008	34.5 kV/800 A
	high voltage cable	AMSC/Nexans [111]	2008	138 kV/2.5 kA
	low voltage cable	Nexans/RWE Deutschland [112]	2013	10 kV/4 kA
	power cable	SWM München/Theva [98]	in progress	—

Table 3.2: Literature review of the most important superconducting large scale devices in all areas of power electronics.

Chapter 4

AC Power Losses in Copper Wires and HTS Tapes

One of the most important objectives for a successful WPT coil design, is the minimization of the AC loss in the winding. At elevated frequencies of a few hundred kHz, where WPT coils are typically operated, the AC loss becomes several times larger than the DC conduction loss and imposes an upper limit for the Q-factor. In order to reduce the AC loss, conventional copper coils usually apply high-frequency litz wires, where the copper cross section is filamented into many thin strands. In principle, this trick could also be used for HTS tapes, but because of technical reasons, filamented HTS tapes are not yet commercially available. The HTS tapes, that are used in this thesis, have a large width of up to 12 mm and are therefore prone to large AC losses, if magnetic fields are applied perpendicularly. In the worst case (large transport currents, large magnetic fields and high frequencies), the AC loss in the HTS tapes could actually become larger than the total loss in a litz wire, and all the benefits that are expected from a superconducting WPT coil would be lost.

In order to provide a profound understanding of the AC losses in litz wires and HTS tapes, we give in the following a comprehensive overview of the fundamental loss mechanisms and the available analytical equations. Hereby we restrict ourselves to infinitely long straight conductors under the action of transport current and external field. The optimization of coil windings will be discussed in Chap. 6. We note that all AC loss equations calculate the energy loss per cycle per unit length and have the formula symbol Q. The power loss in Watt can be obtained by multiplying Q with the frequency and the length of the conductor. The formula symbol for the AC loss has been chosen in consistency with literature and should not be confused with the dimensionless Q-factor, which is a measure for the quality of a coil.

In Sec. 4.1, we focus on copper wires and discuss the transport- and the eddy current loss in solid wires, ideal litz wires and real litz wires. In Sec. 4.2, we focus on HTS tapes and discuss the losses in the HTS layer and in the metallic layers. We distinguish between the low-frequency regime, where analytical equations are available, and the high-frequency regime, where numerical simulations become necessary. In Sec. 4.3, we compare the AC losses in litz wires and HTS tapes.

4.1 Classical Copper Wires

For classical copper wires under the action of current and external field, the AC loss consists of transport loss and eddy current loss. For consistency with literature, we introduce the term *skin-effect* for the frequency dependence of the the transport loss, and the term *proximity-effect* for the frequency dependence of the eddy current loss.

1. Skin Effect
While under DC conditions, the current is distributed uniformly over the complete copper cross section, the current is, under AC conditions, displaced onto the surface of the conductor. In this case, the inside of the conductor is free of current and field. The penetration depth δ of AC current at frequency f into a conductor of conductivity σ, is given by [113]

$$\delta = \frac{1}{\sqrt{\pi \mu_0 \sigma f}}\,, \tag{4.1}$$

The effectively usable copper cross section of the conductor is reduced and consequently $R_{\mathrm{ac}} > R_{\mathrm{dc}}$. The electrical power loss per c ycle and unit length of a copper wire that transports an AC current with RMS value $I_{\mathrm{tr,rms}}$ is given by [113]

$$Q_{\mathrm{tr}} = \frac{1}{f}\frac{\rho}{A} I_{\mathrm{tr,rms}}^2 F\,, \tag{4.2}$$

where $\rho = 1/\sigma$ is the material specific resistivity, A is the conductors cross section and F is the frequency and geometry dependent skin factor.

2. Proximity Effect
When a conductor is penetrated by a time varying magnetic field, eddy currents are induced. The electrical power loss per cycle and unit length of a copper wire under the action of external magnetic field with peak amplitude B_{ext} is given by [113]

$$Q_{\mathrm{eddy}} = \frac{1}{f}\frac{\rho}{\mu_0^2} B_{\mathrm{ext}}^2 D\,, \tag{4.3}$$

where D is the frequency and geometry dependent proximity factor.

The frequency dependence, caused by skin and proximity effects, can be mostly suppressed by using high-frequency litz wire. By filamenting a solid wire into N_{s} thin strands with radius $r_{\mathrm{s}} < \delta$ and twisting the strands around each other, a uniform current distribution can be restored across the whole cross section. Nevertheless, even in an ideal litz wire, an interaction between individual strands inside the wire exists, which is called internal proximity effect and imposes an upper limit for the frequency [114, 115]. Analytical equations to calculate the skin and proximity factors, F and D, have been found in [113], for the cases of solid wire, ideal litz wire and real litz wire. The real litz wire model accounts for the fact that the AC loss in commercially available litz wires depends on the exact wire configuration (number of bundles, sub bundles, pitch length, broken strands) and is typically slightly higher than the calculation suggests for idealized wires

[116]. The deviation from the ideal behavior is modeled with two empirical quality parameters, λ_s and λ_p [116]. We present all equations for F and D in Tab. 4.1. Hereby, $\alpha = (1+i)/\delta$ is the complex skin constant, I_0 and I_1 are the modified Bessel functions of first kind, N_s is the number of strands, r_s is the radius of a single strand, r_{Li} is the radius of the litz wire, and r_D is the radius of a solid wire with equivalent copper cross section.

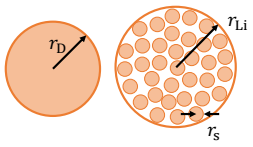

Figure 4.1: Schematic drawing of a solid wire and a litz wire, with equivalent copper cross section. The litz wire is composed of N_s thin strands with radius r_s.

skin factor F	proximity factor D
$F_{solid} = \frac{1}{2}\mathrm{Re}\left\{\frac{\alpha r_D I_0(\alpha r_D)}{I_1(\alpha r_D)}\right\}$	$D_{solid} = 2\pi\mathrm{Re}\left\{\frac{\alpha r_D I_1(\alpha r_D)}{I_0(\alpha r_D)}\right\}$
$F_{ideal} = \frac{1}{2}\mathrm{Re}\left\{\alpha r_s\left[\frac{I_0(\alpha r_s)}{I_1(\alpha r_s)} + \frac{N_s(N_s-1)r_s^2}{r_{Li}^2}\frac{I_1(\alpha r_s)}{I_0(\alpha r_s)}\right]\right\}$	$D_{ideal} = 2\pi N_s\mathrm{Re}\left\{\frac{\alpha r_s I_1(\alpha r_s)}{I_0(\alpha r_s)}\right\}$
$F_{real} = \lambda_s F_{ideal} + (1-\lambda_s)F_{solid}$	$D_{real} = \lambda_p D_{ideal} + (1-\lambda_p)\frac{r_{Li}^2}{r_D^2}D_{solid}$

Table 4.1: Analytical equations to calculate the skin and the proximity factors, F and D, of solid wires, ideal litz wires and real litz wires [113]. This complete set of equations allows a comparison of different wire types and a performance optimization of conventional wireless power transfer coils. We will use it in Sec. 4.3 to compare the AC loss of litz wires and HTS tapes. Detailed description in the main text.

We evaluate F and D exemplary for solid/ideal/real wires with a copper cross section of $A_{Cu} = 4\,\mathrm{mm}^2$ ($N_s = 1000$, $r_s = 35\,\mu\mathrm{m}$, $\lambda_s = 0.5$, $\lambda_p = 0.95$), and we plot the result as a function of frequency in Fig. 4.2.

With F and D being known, we can use Eqs. (4.2) and (4.3) to calculate Q_{tr} and Q_{eddy}. We show the result in Fig. 4.3 and observe clearly the frequency dependence of both loss mechanisms. First, we focus on the transport loss. We see that Q_{tr} decreases linearly with increasing frequency. At low frequency, the solid wire and the litz wire perform identically. At higher frequency, the litz wire suppresses the skin effect and outperforms the solid wire. If the frequency is further increased, at some point the transport loss in the litz wire increases strongly due to the internal proximity effect. Second, we focus on the eddy current loss. We see that Q_{eddy} depends strongly on the diameter of the conductor. At low frequency, the loss in the solid wire is by 3 orders of magnitude larger than the loss in the litz wire. Q_{eddy} increases linearly with increasing frequency until the penetration depth δ approaches the diameter of the conductor. For the solid wire in our example, this happens at $f \approx 10\,\mathrm{kHz}$. Beyond this frequency, the center of the conductor is shielded (the external field can only penetrate the conductor on the length δ) and Q_{eddy} starts to decrease with increasing frequency. For the litz wire, the transition frequency is in the order of a few MHz and Q_{eddy} increases continuously. This leads to the fact that Q_{eddy} of solid wires and litz wires can become comparable at high frequencies.

For further information and a detailed discussion of the parameter interdependencies in litz

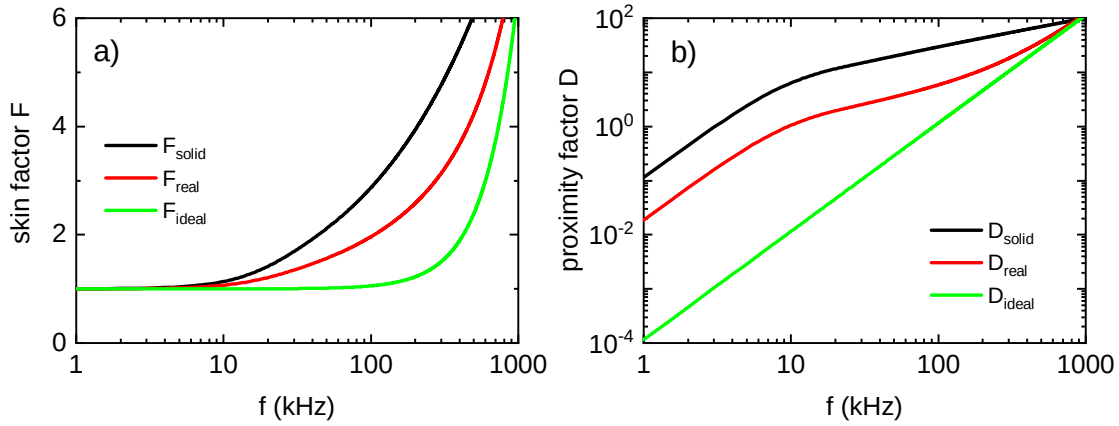

Figure 4.2: Analytical calculation of the (a) skin and (b) proximity factors for solid wire, ideal litz wire and real litz wire with identical copper cross section $A_{\mathrm{Cu}} = 4\,\mathrm{mm}^2$. The litz wire consists exemplary of 1000 strands with a radius of $r_{\mathrm{s}} = 35\,\mu\mathrm{m}$. The quality parameters of the real litz wire model are $\lambda_{\mathrm{s}} = 0.5$ and $\lambda_{\mathrm{p}} = 0.95$.

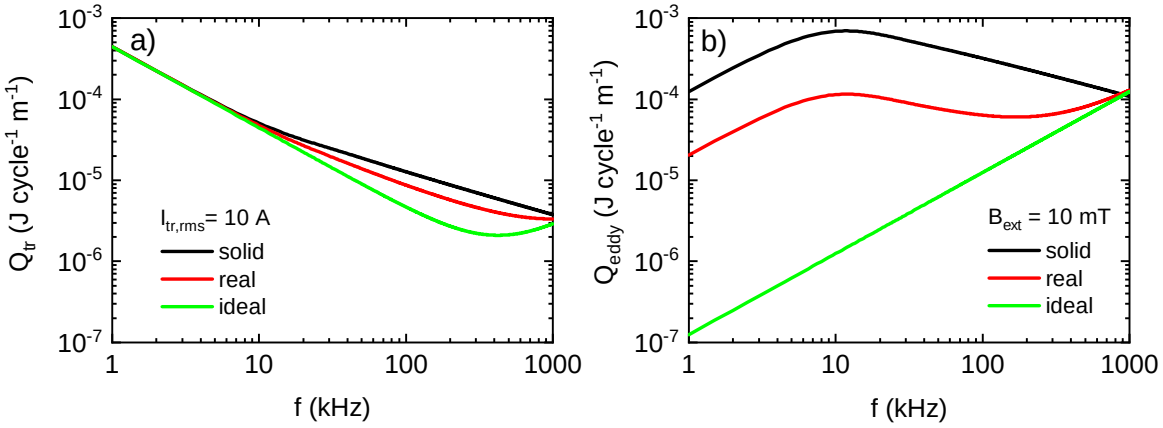

Figure 4.3: Analytical calculation of the (a) transport and (b) eddy current loss for the same wire configuration as in Fig. 4.2. The transport loss is evaluated at $I_{\mathrm{tr,rms}} = 10\,\mathrm{A}$. The eddy current loss is evaluated at $B_{\mathrm{ext}} = 10\,\mathrm{mT}$. The frequency dependence of both loss mechanisms is observable. Detailed description in the main text.

wires, we refer the reader to [113]. Nevertheless, we want to mention that we have implemented the complete analytical model into a Mathematica code, which is now used by the company Würth Elektronik eiSos. This powerful and versatile tool allows us to compare the performance of different litz wires, to optimize WPT coils regarding their cost/performance ratio and to predict the AC behavior. We have demonstrated the validity of the model in Ref. [117]. In this reference, we have shown for several conventional copper coils that the calculation of the AC loss agrees with experimental results.

4.2 HTS Tapes

In superconductors, the loss mechanisms differ fundamentally from those of classical copper wires. In the DC regime, the electrical resistance is zero and high currents can be transported without power loss. Resistive DC losses appear only if the current approaches the critical current (I_c) and the flux vortices start to flow. Under AC conditions however, significant losses appear far below I_c. Depending on the frequency, the current amplitude and the external field, the AC losses can become so large that they lead to self-heating of the tape and result in a quench. Commercial HTS tapes consist of several different layers with different loss mechanisms and different frequency dependencies. In the following, we will discuss the dominant loss mechanisms in each layer and the interaction between the individual layers.

The main loss contributions in thin HTS tapes can generally be distinguished into hysteresis loss and eddy current loss. As the Theva tapes, considered in this thesis, are based on non-magnetic (hastelloy) substrates, ferromagnetic losses in the substrate are not considered. The hysteresis loss appears in the HTS layer and dominates at low frequencies. The eddy current loss appears in all normal conducting, metallic layers and dominates at high frequencies [86]. We show the cross section of an HTS tape with all relevant layers in Fig. 4.4

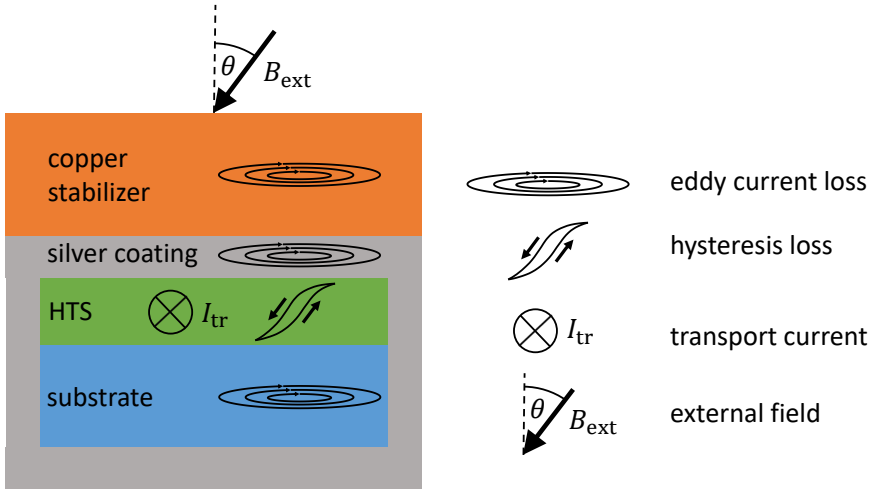

Figure 4.4: Schematic drawing of the main loss mechanisms in a thin HTS tape under the action of AC transport current and external AC magnetic field. The HTS layer is dominated by hysteresis loss and the normal conducting layers are dominated by eddy current loss. The drawing is not to scale.

The loss mechanisms can generally be dissociated by their frequency dependence. The AC loss per unit length per cycle, is frequency independent for the case of hysteresis loss (Q_{hyst}), and scales linearly with f for the case of eddy current loss (Q_{eddy}) [118]. The nature of the dominating loss mechanism can therefore be determined experimentally by performing several loss measurements at different frequencies. The total power loss per unit length is given by

$$P_{\text{tot}} = P_{\text{hyst}} + P_{\text{eddy}} = \underbrace{fQ_{\text{hyst}}}_{\propto f} + \underbrace{fQ_{\text{eddy}}}_{\propto f^2} . \tag{4.4}$$

4.2.1 Hysteresis Loss in the HTS Layer

First, we discuss the hysteresis loss in the HTS layer. This loss mechanism is similar to the magnetization loss in ferromagnetic materials. When hard superconductors are exposed to an alternating magnetic field, they exhibit an irreversible magnetization behavior [119]. The H-M curve has the shape of a hysteresis and the enclosed area is proportional to the energy loss per volume. The macroscopic explanation for the power dissipation is the following. The flux lines in the superconducting volume must adapt continuously to the externally imposed changing magnetic field and the energy to overcome the pinning force is lost irreversibly during each cycle. An even better understanding can be gained by studying the current and the field distribution in the superconductor during one cycle in more detail. At zero external field, the superconductor is in the Meissner state and current and field are zero everywhere in the volume. With increasing external field, small shielding currents begin to flow in the surface of the superconductor to prevent the penetration of flux into the superconducting volume. With further increase of the external field, the outer regions reach the critical current density, the flux starts to penetrate into the sample and deeper regions attempt to expel the flux from the center. When the external field is reversed, current reversals occur in outer regions first and then deeper in the sample. After reducing the external field again to zero, one observes that some magnetic flux remains trapped in the sample and the corresponding energy is lost [120]. For the special case of thin and wide HTS tapes, one observes that the magnetic flux penetrates from the edges towards the center [121].
Hysteresis loss in the HTS layer can be caused (a) by the self-field of an AC transport current, (b) by an externally applied AC magnetic field or (c) by the combination of both. The three different situations are depicted in Fig. 4.5. We note that due to the strong anisotropy of the tape, mostly the perpendicular component (B_{per}) of the externally applied magnetic field is relevant and the parallel component is neglected.

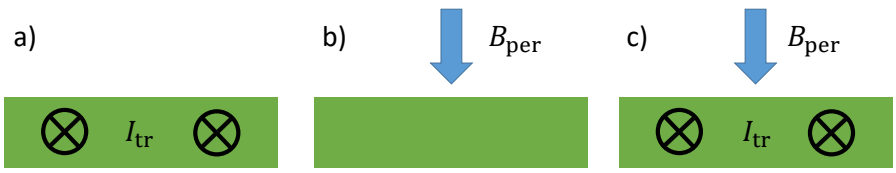

Figure 4.5: Illustration of different sources of AC loss in thin HTS sheets. Power losses are generated by (a) the self-field of AC transport current, (b) externally applied AC magnetic field and (c) simultaneous action of both.

In literature [120–122], analytical equations for all three situations have been found. The solutions are based on the critical state model (CSM) and on the assumptions that J_{c} is constant across the width of the tape and independent of the applied field [86].
In the following we introduce analytical equations for thin HTS tapes of width w, a critical sheet current density J_{c} (given in A/m) and a critical current $I_{\mathrm{c}} = J_{\mathrm{c}}w$, as listed in Tab. 3.1.
For the calculation of AC losses under the action of external field, it is useful to define a char-

acteristic field strength $H_c = J_c/\pi$ and accordingly the characteristic flux density $B_c = \mu_0 H_c$. This characteristic value allows to express the penetration width of magnetic flux from the edge towards the center of the tape as a function of the external field strength. For further details we refer the reader to [121].

(a) Thin HTS layer under the action of AC current - Norris Equation
The hysteresis loss per cycle and unit length of a thin HTS layer that carries AC current of peak amplitude I_{tr} has been derived analytically by W. T. Norris in Ref. [120]. Two approximations for elliptical wires and thin strips are given.

$$Q_{\text{Norris,ellipse}} = \frac{I_c^2 \mu_0}{\pi} F_{\text{ellipse}}\left(i_{tr}\right) , \tag{4.5}$$

$$Q_{\text{Norris,strip}} = \frac{I_c^2 \mu_0}{\pi} F_{\text{strip}}\left(i_{tr}\right) , \tag{4.6}$$

where F_{ellipse} and F_{strip} are functions of the normalized transport current amplitude $i_{tr} = I_{tr}/I_c$

$$F_{\text{ellipse}}\left(i_{tr}\right) = (1 - i_{tr}) \ln(1 - i_{tr}) + (2 - i_{tr}) i_{tr}/2 , \tag{4.7}$$

$$F_{\text{strip}}\left(i_{tr}\right) = (1 - i_{tr}) \ln(1 - i_{tr}) + (1 + i_{tr}) \ln(1 + i_{tr}) - i_{tr}^2 . \tag{4.8}$$

Due to the high aspect ratios of commercially available tapes, measurement results should match the strip approximation. Round edges and reduced critical currents close to the edges however can add an elliptical contribution. Therefore, measurement results are typically in between the predictions of Eq. (4.5) and (4.6).
The validity of the Norris equations has been shown in several papers, e.g. in [123, 124] for YBCO tapes at low frequencies and in [125] for GdBCO tapes in the kHz regime.

(b) Thin HTS layer under the action of perpendicular AC field - Brandt Equation
The hysteresis loss per cycle and unit length of a thin HTS layer that is exposed to a perpendicular AC field with amplitude B_{per} has been derived by E. H. Brandt et al. in [121].

$$Q_{\text{Brandt}} = J_c B_{\text{per}} w^2 G\left(b_{\text{per}}\right) , \tag{4.9}$$

where G is a function of the normalized field amplitude $b_{\text{per}} = B_{\text{per}}/B_c$

$$G\left(b_{\text{per}}\right) = \frac{2}{b_{\text{per}}} \ln\cosh\left(b_{\text{per}}\right) - \tanh\left(b_{\text{per}}\right) , \tag{4.10}$$

The validity of the Brandt equation has also been shown in several papers, e.g. in [126, 127] for YBCO tapes at low frequencies and in [45] for GdBCO tapes in the kHz regime.

(c) Thin HTS layer under the simultaneous action of transport current and perpendicular AC field - Schönborg Equation
The hysteresis loss per cycle and unit length of a thin HTS layer, which is exposed to the simultaneous action of AC transport current and perpendicular AC field, has been derived by N.

Schönborg in [122].

$$Q_{\text{Schoenborg}} = \frac{I_c^2 \mu_0}{\pi} H\left(i_{\text{tr}}, b_{\text{per}}\right) , \tag{4.11}$$

where $H\left(i_{\text{tr}}, b_{\text{per}}\right)$ is a lengthy equation that depends on the amplitudes of the applied current and the applied field, and shall not be reproduced here.
For the limiting cases of zero magnetic field or zero transport current, the Schönborg solution simplifies to the Norris- and to the Brandt equation, respectively.
We evaluate Eq. (4.11) in Fig. 4.6 exemplary for a typical HTS tape with a critical sheet current density of $J_c = 400\,\text{A/cm}$ and we see that the loss scales with $Q \propto I^4$ and $Q \propto B^4$. The Schönborg equation allows us to calculate the exact hysteresis loss in HTS tapes, if the current and the field amplitudes are known, and we will use it in Chap. 6 to optimize the coil winding.

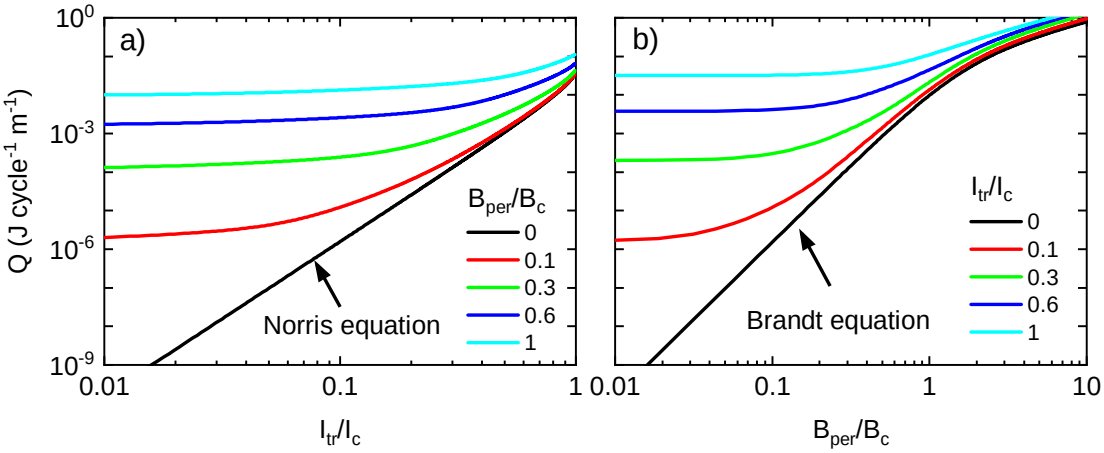

Figure 4.6: Hysteresis loss per cycle and unit length in a thin HTS layer under the simultaneous action of AC transport current and perpendicular AC field. The AC loss according to Eq. (4.11) is plotted (a) versus the normalized current amplitude for different field amplitudes and (b) versus the normalized field amplitude for different current amplitudes.

The validity of the Schönborg equation has been demonstrated in literature. According to [126, 128, 129], the analytical result agrees excellently with numerical simulations and with experimental results. In the high-current and low-field regime, the error of Eq. (4.11) is below 10 %. Only in the low-current and high-field regime, Eq. (4.11) slightly overestimates the hysteresis loss [128].
We note that the Schönborg equation is only valid if the applied AC current and the AC magnetic field are in phase. If we consider a coil winding in its self-field, where the magnetic field of the complete coil penetrates the individual turns, this condition is certainly satisfied. If we consider, however, a coil winding in an externally imposed field, e.g. a WPT system, where the receiver coil is exposed to the magnetic field of the transmitter coil, phase shifts of $\Delta\varphi = 90\,^\circ$ can appear. Theoretical and experimental studies in [130–132] have shown that the AC loss takes its maximum value at zero phase shift and reaches its minimum value in a range between $\Delta\varphi = 60\,^\circ$ and $\Delta\varphi = 105\,^\circ$. So, for the case of a WPT system, the most important loss component is the self-field contribution of the individual coils. The crosstalk between the magnetic fields of separate coils can be mostly neglected, because the field amplitude is much smaller

and because the phase shift between the coils agrees well with the condition for minimum AC loss.

To sum up, the Schönborg equation allows to calculate the AC loss in the superconducting layer of commercially available HTS tapes for any combination of applied current and field amplitudes. The result is correct if the current and the field are in phase, and gives an upper limit for all other phase conditions. In Chap. 6, we will use the Schönborg equation to calculate and optimize the AC loss of coil windings. Thereby we will face the problem that we generally do not know the magnetic field distribution within the winding. We will show that this problem can easily be solved by coupling the analytical Schönborg equation to numerical field simulations. The simulations determine the amplitude and the angle of the generated field at the position of each individual turn and allow a very fast and precise estimation of the hysteresis loss.

4.2.2 Eddy Current Loss in Normal Conducting Metal Layers

Second, we discuss the eddy current loss in the normal conducting metal layers. Because the metallic layers are in the direct vicinity of the superconducting layer, the calculation of the eddy current loss goes beyond the classical methods, which are typically used for metallic thin films. The field displacement in the HTS layer causes a significant reduction of the perpendicular field component [121], which results in a strong shielding effect for the metallic layers [133]. In low frequency applications, where HTS tapes are typically used, the eddy current loss is much smaller than the hysteresis loss [118, 134]. In some studies [135, 136], the eddy current contribution is even completely neglected. However, due to the fact that Q_{hyst} is frequency independent and Q_{eddy} scales with f, the share of eddy current loss increases with increasing frequency. At a certain transition frequency f_{tr}, the eddy currents start to distort the magnetic field distribution around the HTS strip and the shielding effect breaks down. At sufficiently high frequencies, the HTS tape behaves identical to a simple metal strip and the eddy current loss dominates the total loss of the tape. Some very recent publications [44–46, 125, 137] have shown that the eddy loss contribution becomes significant in the kHz regime. Even though the results of these papers are at some points inconsistent and the exact behavior of HTS tapes at the transition frequency is not fully understood yet, it is clear that we must consider the eddy current loss in our coil design.

A commercial HTS tape contains up to three metallic layers with different conductivities and different thicknesses. In order to obtain a profound understanding of the frequency dependence of each layer, we study the layers individually. Therefore, we simplify the multi-layered tape into a metal-superconductor-strip (m-s-strip), as depicted in Fig. 4.7. The thickness of the metal layer is t_{m} and its specific resistivity is ρ_{m}. For the case of the silver coating, where two identical layers are present on the front- and on the backside of the HTS layer, we simplify the geometry to a single silver layer with twice the thickness. Due to the fact that Q_{eddy} scales linearly with t_{m}, this approach is justified.
For such a m-s-strip, we define a low- and a high-frequency regime. The transition frequency f_{tr} is given by the condition that eddy currents in the metallic layer become comparable to the supercurrents in the HTS layer. In [133] it is found that f_{tr} depends on t_{m}, w and ρ_{m} and is

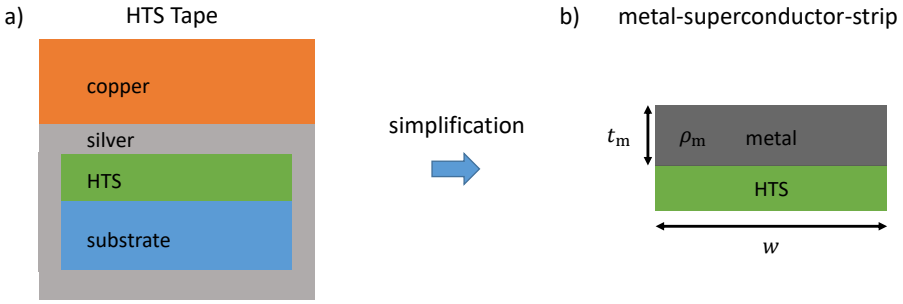

Figure 4.7: Simplification of a multi-layered HTS tape into a metal-superconductor-strip (m-s-strip). This model is used to calculate the eddy current loss and to study the frequency dependence of each metal layer individually.

given by

$$f_{\mathrm{tr}} = \frac{\rho_{\mathrm{m}}}{\mu_0 t_{\mathrm{m}} w} \,. \tag{4.12}$$

We evaluate the transition frequencies for a selection of metallic thin films, which are typically used in commercial HTS tapes in Tab. 4.2.

material	ρ_{m}^{77K} (nΩ m)	t_{m} (µm)	w (mm)	f_{tr} (kHz)
hastelloy	1240 [138]	100	12	822
silver	2.7 [139]	3	12	60
		10	12	13
copper	2.0 [139]	20	12	6.6
		100	12	1.3

Table 4.2: Properties and transition frequencies of selected metallic thin films, which are typically used in commercial HTS tapes. In the low-frequency regime ($f \ll f_{\mathrm{tr}}$), the metallic layers are shielded by the HTS layer and eddy current loss is small compared to the hysteresis loss. In the high-frequency regime ($f \gg f_{\mathrm{tr}}$), the shielding effect breaks down and the eddy current loss dominates the total loss of the HTS tape.

We see that f_{tr} depends strongly on the design of the HTS tape. For the case that the HTS tape is stabilized with a 100 µm thick copper layer, the eddy current loss becomes already significant at frequencies of 1.3 kHz. If the thickness of the stabilizer is reduced to 10 µm, the tape can be used at frequencies of up to 13 kHz. If the copper stabilizer is removed completely, which is dangerous in terms of quench protection, the silver layer would dominate the frequency dependence and the tape could be used at frequencies of up to 60 kHz. Even though the hastelloy substrate has a thickness of 100 µm, the transition frequency of this layer is beyond 800 kHz because of its large specific resistivity.

Low-Frequency Regime

In the low-frequency regime, where $f \ll f_{\mathrm{tr}}$ is satisfied, analytical equations for the eddy current loss in the metal layer of a m-s-strip have been derived by K.-H. Müller [133]. Solutions have been found (a) for the case that the metal layer is exposed to the self-field of an AC transport current, flowing in the superconducting layer, and (b) for the case that the metal layer is exposed to an external perpendicular AC field, which penetrates the m-s-strip.

(a) Metal-superconductor strip in the self-field of an AC transport current

$$Q_{\mathrm{Mueller,tr}} = \frac{8\mu_0^2 t_\mathrm{m} w}{\pi \rho_\mathrm{m}} f I_\mathrm{c}^2 \, K(i_\mathrm{tr}) \,, \tag{4.13}$$

with

$$K(i_\mathrm{tr}) = \int_0^{i_\mathrm{tr}} du \, \sqrt{i_\mathrm{tr} u - u^2} \left[1 - \sqrt{1-u^2} - \frac{u}{2} \ln \frac{1+u}{1-u} + \frac{1}{8} \left(\ln \frac{1+u}{1-u} \right)^2 \right] . \tag{4.14}$$

(b) Metal-superconductor strip in perpendicular AC magnetic field

$$Q_{\mathrm{Mueller,per}} = \frac{\pi^2 t_\mathrm{m} w^3}{6 \rho_\mathrm{m}} f B_\mathrm{per}^2 \, M(b_\mathrm{per}) \,, \tag{4.15}$$

with

$$M(b_\mathrm{per}) = \frac{8}{\pi} \frac{1}{b_\mathrm{per}^2} \int_0^{b_\mathrm{per}} \sqrt{b_\mathrm{per} \xi - \xi^2} \times \left(1 - \frac{3}{\cosh^2 \xi} + \frac{2}{\cosh^3 \xi} \right) d\xi \,. \tag{4.16}$$

In the original publication [133], the solutions have been derived by integrating the time averaged local power loss $1/T \int_0^T E(x,z,t) J(x,z,t) \mathrm{d}T$ over the spatial dimensions of the metal layer. The derivation contains several reformulations and substitutions. The exact meaning of the integration variables u and ξ, which appear in the final result, is not explicitly defined in [133]. Nevertheless, the integral equations (4.14) and (4.16) can easily be implemented into a numerical calculation program (e.g. Wolfram Mathematica) and can be solved for any values of i_tr and b_per. The integration variables u and ξ vanish during the calculation.
We note that $K(i_\mathrm{tr})$ and $M(b_\mathrm{per})$ are shielding terms that account for the fact that the supercurrents in the HTS layer reduce the perpendicular field component. In the limit $B_\mathrm{c} \to 0$, i.e. if the thickness of the superconductor is decreased until only a metal strip (m-strip) remains, we find $M(b_\mathrm{per}) \to 1$ and Eq. (4.15) simplifies to

$$Q_{\mathrm{eddy,m\text{-}strip}} = \frac{\pi^2 t_\mathrm{m} w^3}{6 \rho_\mathrm{m}} f B_\mathrm{per}^2 \,, \tag{4.17}$$

which is the eddy current loss in the m-strip, without the superconducting layer being attached to it. Equations (4.13) and (4.15) show that the eddy current loss in m-s-strips scales proportional to t_m and inversely to ρ_m. Therefore, the biggest eddy current loss appears if the metal layer is thick and highly conductive. As worst case scenario, we evaluate the eddy current loss in a m-s-strip with $t_\mathrm{Cu} = 100\,\mu\mathrm{m}$, $\rho_\mathrm{Cu}^{77K} = 2\,\mathrm{n\Omega m}$, $w = 12\,\mathrm{mm}$ and $J_\mathrm{c} = 400\,\mathrm{A/cm}$. We compare the resulting eddy current loss to the hysteresis loss at a frequency of $f = 1\,\mathrm{kHz} < f_\mathrm{tr}$ in Fig. 4.8. We see that the eddy current loss is small compared to the hysteresis loss at all relevant current and field amplitudes and can therefore be neglected. Only at very high currents and fields, where the superconductivity and hence also the shielding effect breaks down, the eddy current loss in the m-s-strip approaches the value of a simple m-strip and exceeds the hysteresis loss.

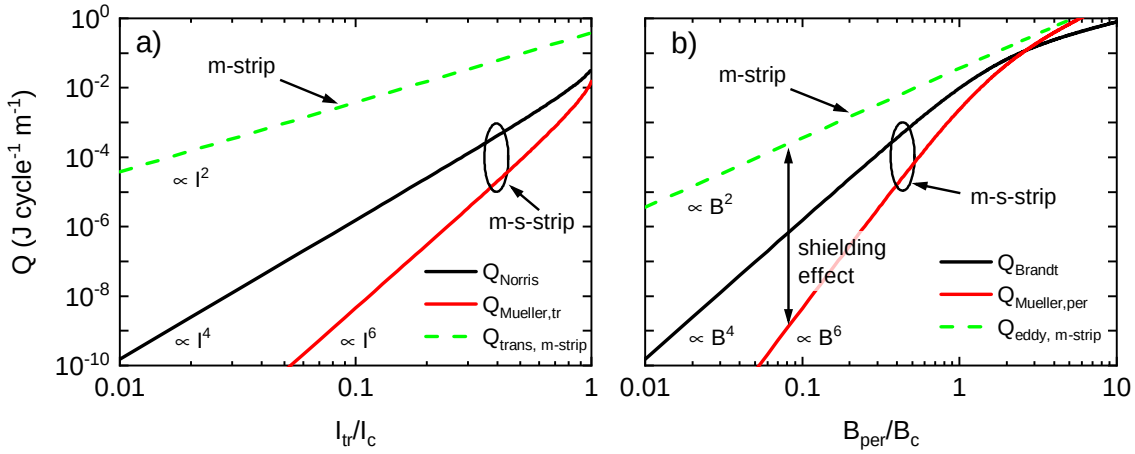

Figure 4.8: Comparison of the hysteresis loss (Q_{Norris}, Q_{Brandt}) and the eddy current loss ($Q_{\mathrm{Mueller,tr}}$, $Q_{\mathrm{Mueller,per}}$) in a m-s-strip with $t_{\mathrm{m}} = 100\,\mu\mathrm{m}$, $\rho_{\mathrm{Cu}}^{77K} = 2\,\mathrm{n}\Omega\mathrm{m}$, $w = 12\,\mathrm{mm}$ and $J_{\mathrm{c}} = 400\,\mathrm{A/cm}$. The energy loss per cycle and unit length is plotted against (a) the applied AC transport current and (b) the applied AC perpendicular magnetic field. The losses are evaluated at $f = 1\,\mathrm{kHz} < f_{\mathrm{tr}}$. As reference, we also show the loss of an equivalent m-strip without the presence of the superconducting layer (dashed line). The shielding effect in the m-s-strip can be clearly observed. The total loss of the m-s-strip is dominated by hysteresis loss in the complete range of relevant amplitudes. We conclude that the eddy current loss can be neglected in the low-frequency regime.

High-Frequency Regime

If the frequency is increased until it approaches f_{tr}, the analytical equations derived by K.-H. Müller lose their validity and numerical methods become necessary. If the frequency is high enough, so that $f \gg f_{\mathrm{tr}}$, the skin-depth is smaller than the thickness of the metal layer and it is clear that all magnetic fields decay within the metal layer. In this high-frequency regime, the loss nature of an HTS tape is obviously completely metallic.

At the transition from the low- to the high-frequency regime, however, a mixture of supercurrents in the HTS layer and eddy currents in the metal layer is present. Latest research [46, 140] suggests that with increasing frequency, an increasing share of the supercurrents merges into the metallic layers. The exact mechanisms at frequencies close to f_{tr} is, however, not fully understood yet. Due to the fact that superconducting and normal conducting regions co-exist next to each other, complicated numerical simulation methods are necessary to estimate the loss in both layers simultaneously. Such an analysis is currently discussed in literature and could be the subject of our future research. Here in this thesis, it is however not our focus and we restrict our studies to classical simulations of the eddy current loss in m-strips. Nevertheless, even such simplified methods provide interesting insights. We will show in Chap. 8 that our simulations of the eddy current loss agree quantitatively with experimental results on HTS tapes. The following simulations have been performed with the commercially available finite element method (FEM) software Ansys Maxwell. Detailed information about the simulation setup can be found in Appendix A.1.

We show the numerically simulated eddy current loss in different m-strips (properties as defined in Tab. 4.2) under the action of perpendicular AC field in Fig. 4.9. The loss per cycle and unit

length is plotted as a function of the frequency at a fixed field amplitude of $B_{\mathrm{per}} = 1\,\mathrm{mT}$. In this simulation, the m-strip carries zero transport current, i.e. all induced currents are eddy currents.

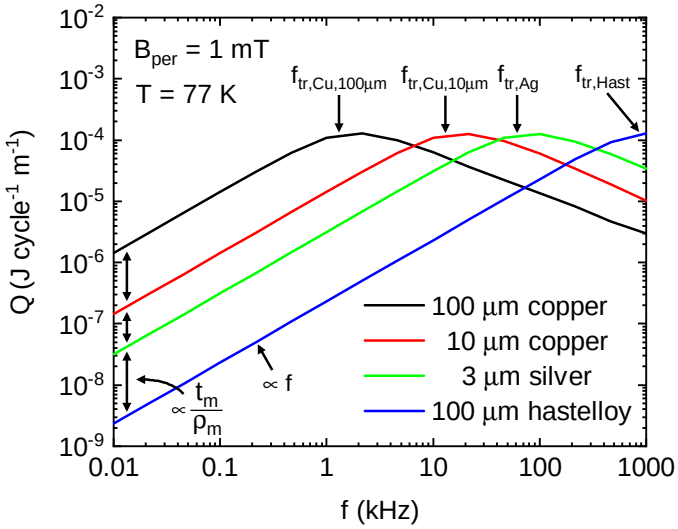

Figure 4.9: Numerically simulated eddy current loss in different m-strips (properties as defined in Tab. 4.2) under the action of a perpendicular AC field with amplitude $B_{\mathrm{per}} = 1\,\mathrm{mT}$. The low-frequency behavior agrees with Eq. (4.17) and the transition frequencies agree with Eq. (4.12). In the high-frequency regime, the eddy current loss decreases with increasing frequency.

In the low-frequency regime, the numerical simulation agrees exactly with Eq. (4.17) and the loss scales proportional to $t_{\mathrm{m}} f/\rho_{\mathrm{m}}$. Similar to the eddy current loss in solid copper wires (compare Fig. 4.3 (b)), the loss reaches a plateau when the frequency approaches the characteristic transition frequency and starts to decrease with further increasing frequency. The numerically obtained transition frequencies of all simulated m-strips agree with Eq. (4.12). The frequency behavior can be understood by analyzing the magnetic field distribution around the m-strip as shown in Fig. 4.10.

In the low-frequency regime (Fig. 4.10 (a)), the induced eddy currents are small and the m-strip is transparent to the magnetic field. At the transition frequency (Fig. 4.10 (b)), the magnetic fields which are generated by the induced eddy currents become comparable to the external field and start to cause local field distortions around the metal strip. The loss reaches its maximum at the frequency where the eddy currents completely shield the strip from the perpendicular field component (Fig. 4.10 (c)). A further increase of the frequency does not change the field distribution (Fig. 4.10 (d)) and the loss per cycle consequently decreases with increasing frequency.

It is interesting to note that the magnetic field distribution around a m-strip in the high-frequency limit is very similar to the one of a superconducting strip in the low-frequency limit [121]. The external field penetrates the strip only at the edges and the center is completely free of perpendicular field. We conclude the following:

For the case of a m-s-strip in the low-frequency regime

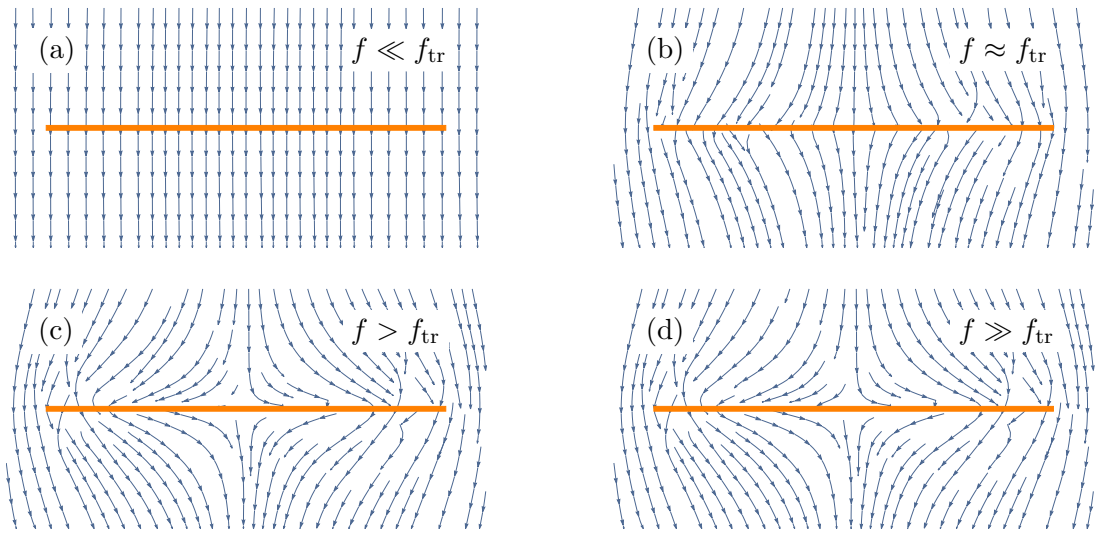

Figure 4.10: Magnetic field distribution around a m-strip in homogeneous perpendicular AC field. In the low-frequency regime (a), the induced eddy currents are small and the m-strip is transparent to the magnetic field. At the transition frequency (b), the induced eddy currents start to shield the perpendicular field component. Beyond the transition frequency (c), the perpendicular field component is completely shielded and a further increase of the frequency (d) does not change the field distribution.

- the field displacement work is afforded by supercurrents in the HTS layer and
- the metallic layer is shielded from the perpendicular field and the eddy current loss is small (as predicted by the Müller equations).

For the case of the m-s-strip in the high-frequency regime

- the field displacement work is afforded by eddy currents in the metallic layer and
- the metallic layer is exposed to the external perpendicular field and the eddy current loss is large.

Finally, we show the frequency dependence of the hysteresis loss and the eddy current loss together in Fig. 4.11. The loss of a m-s-strip with $t_{Cu} = 100\,\mu m$, $\rho_{Cu}^{77K} = 2\,n\Omega m$, $w = 12\,mm$ and $J_c = 400\,A/cm$ is evaluated at perpendicular field amplitudes of (a) $B_{per} = 1\,mT$ and (b) $B_{per} = 10\,mT$. The transition area between the low- and the high-frequency regime is colored gray. The frequency independent hysteresis loss is shown as a black solid line. The eddy current loss according to the Müller equation is shown as a red line and the eddy current loss according to the numerical simulation is shown as a green line. The red and the green lines are solid/dashed, where the according eddy current model is valid/invalid.
This comparison shows that the eddy current loss indeed dominates the AC loss in the high-frequency regime if the field amplitudes are low. With increasing field amplitude, the eddy current loss and the hysteresis loss become comparable ($Q_{eddy,num} \propto B^2$, $Q_{Brandt} \propto B^4$). Independent of the question, which loss mechanisms dominates at which frequency, we see very drastically how challenging the application of HTS tapes at high frequencies will be. Even if no eddy current loss is present, the hysteresis loss at $f = 100\,kHz$ and $B_{per} = 10\,mT$ is $P_{loss} \approx 100\,W/m$. At

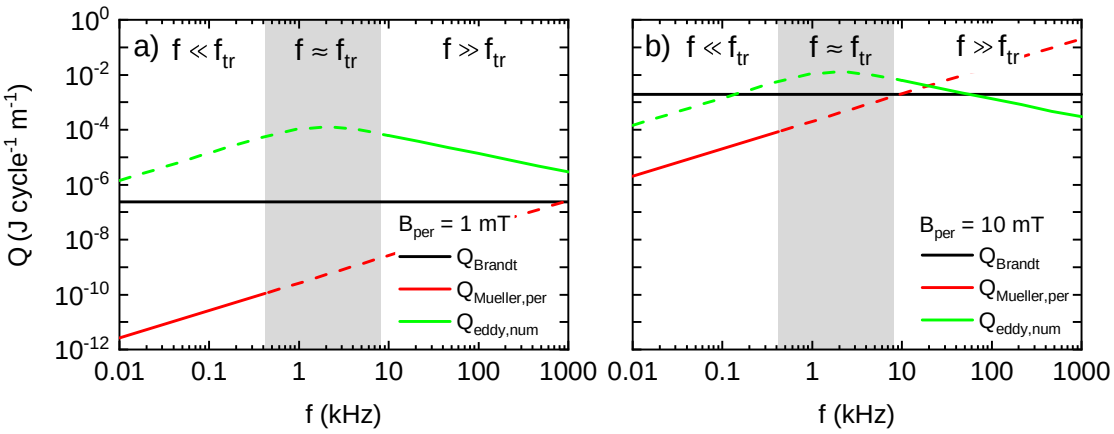

Figure 4.11: Frequency dependence of the different loss mechanisms in a m-s-strip with $t_{\mathrm{Cu}} = 100\,\mu\mathrm{m}$, $\rho_{\mathrm{Cu}}^{77K} = 2\,\mathrm{n\Omega m}$, $w = 12\,\mathrm{mm}$ and $J_{\mathrm{c}} = 400\,\mathrm{A/cm}$ in perpendicular AC magnetic field. The hysteresis loss (Q_{Brandt}, black line), the eddy current loss according to the Müller equation ($Q_{\mathrm{Mueller,per}}$, red line) and the eddy current loss according to the numerical simulation ($Q_{\mathrm{eddy,num}}$, green line) are compared to each other at field amplitudes of (a) $B_{\mathrm{per}} = 1\,\mathrm{mT}$ and (b) $B_{\mathrm{per}} = 10\,\mathrm{mT}$. The transition regime between the low- and the high-frequency limits is colored gray. The red and the green lines are solid/dashed, where the according eddy current model is valid/invalid.

such a high loss rate, it would be difficult to keep the surface temperature of the HTS tape below T_{c}. If we manage to keep the perpendicular field component in our WPT coils low, we see a reasonable chance that the HTS tape does not quench during operation at high frequencies. At $f = 100\,\mathrm{kHz}$ and $B_{\mathrm{per}} = 1\,\mathrm{mT}$, the total AC loss (including eddy current loss) will be most likely $P_{\mathrm{loss}} \approx 1\,\mathrm{W/m}$.

4.3 Comparison Between Litz Wires and HTS Tapes

In order to clarify under which conditions the replacement of litz wires by HTS tapes brings an improvement of the performance, we use in the following the introduced analytical models to compare the AC losses. We study 4 different litz wires and 2 different HTS tapes with parameters as defined in Tab. 4.3 and Tab. 4.4.

	A_{Cu} (mm^2)	number of strands	R_{DC} (mΩ/m)
A	0.4	104	42
B	1.2	311	14
C	6	1560	2.8
D	12	3120	1.4

Table 4.3: Parameters of the selected litz wire configurations. All wires have the same strand radius of $r_{\mathrm{s}} = 35\,\mu\mathrm{m}$ and a specific resistance of $\rho_{\mathrm{Cu}}^{300K} = 17\,\mathrm{n\Omega\,m}$. The AC losses are calculated according to the real litz wire model. The quality parameters are $\lambda_{\mathrm{s}} = 0.5$ and $\lambda_{\mathrm{p}} = 0.9$. Wire types A and B have the equivalent cross sections of typical HTS tapes. Wire types C and D have realistic cross sections, which are typically used in high-power WPT coils.

tape type	width (mm)	thickness (µm)	J_c (A/cm)	I_c (A)
A	4	100	400	160
B	12	100	400	480

Table 4.4: Parameters of the selected HTS tapes. The thickness is a typical value including all technical layers and is relevant for the comparison to a copper wire with equivalent cross section.

The cross sections of the litz wire configurations A and B correspond to the equivalent cross sections of the HTS tapes. The litz wire configurations C and D have realistic cross sections, which are typically used in high-power WPT coils. We note that we have decided to evaluate the AC loss of the litz wires at room temperature. It is certainly true that the specific resistance of copper, and hence also the DC conduction loss in copper wires, decreases nearly by a factor of 10 when cooled from room temperature to 77 K. At elevated frequencies in the kHz regime, the performance of litz wires is, however, dominated by their AC behavior and a reduction of the temperature does not necessarily decreases the total loss. At a given operating frequency, the radius of the strands in the litz wire is chosen in such a way that it is smaller than the penetration depth δ. Due to the fact that δ decreases with decreasing resistance the AC loss increases if the radius of the strands in the litz wire is not adapted. So generally, the performance of commercially available litz wires is not improved by simply cooling them down, and our comparison between HTS tapes at 77 K and litz wires at 300 K is fair.
We plot the AC loss of each conductor as a function of the frequency in Fig. 4.12. The operating conditions vary between the subfigures. The transport current amplitude increases from left to right (10 A, 25 A and 50 A) and the magnetic field amplitude increases from top to bottom (0 mT, 3 mT, 5 mT and 20 mT). In order to improve the readability of the figure, the presented AC loss of the HTS tapes includes only the hysteresis loss. The eddy current loss, which can become significant in the high-frequency regime is not shown. The results in this figure should therefore be considered as a best-case scenario, which is valid if the HTS tapes do not contain metallic layers.
The analysis of Fig. 4.12 reveals the following interesting results:

- At low frequencies, HTS tapes outperform the litz wires strongly. With increasing frequency, the performance gain shrinks. As long as the current and the field amplitudes remain low, the application of HTS tapes can even be beneficial at high frequencies.
- With increasing current and field amplitudes, the application of HTS tapes becomes more and more challenging. At 3 mT and 100 kHz, the performance gain of the HTS tapes is already completely lost. Beyond 5 mT, the loss of HTS tapes even exceeds the loss in litz wires in a broad range of frequencies.
- Depending on the operating conditions, both, the 4 mm wide tape or the 12 mm wide tape can be favorable. Narrow tapes should be chosen if strong magnetic fields are present and wide tapes should be chosen if large current amplitudes are required. It is interesting to note that at a working point with $B_{\mathrm{rms}} = 3\,\mathrm{mT}$ and $I_{\mathrm{rms}} = 50\,\mathrm{A}$, the loss in both HTS tapes is identical. The increased magnetization loss of the wider tape is compensated by a reduced transport loss due to the larger value of I_c.

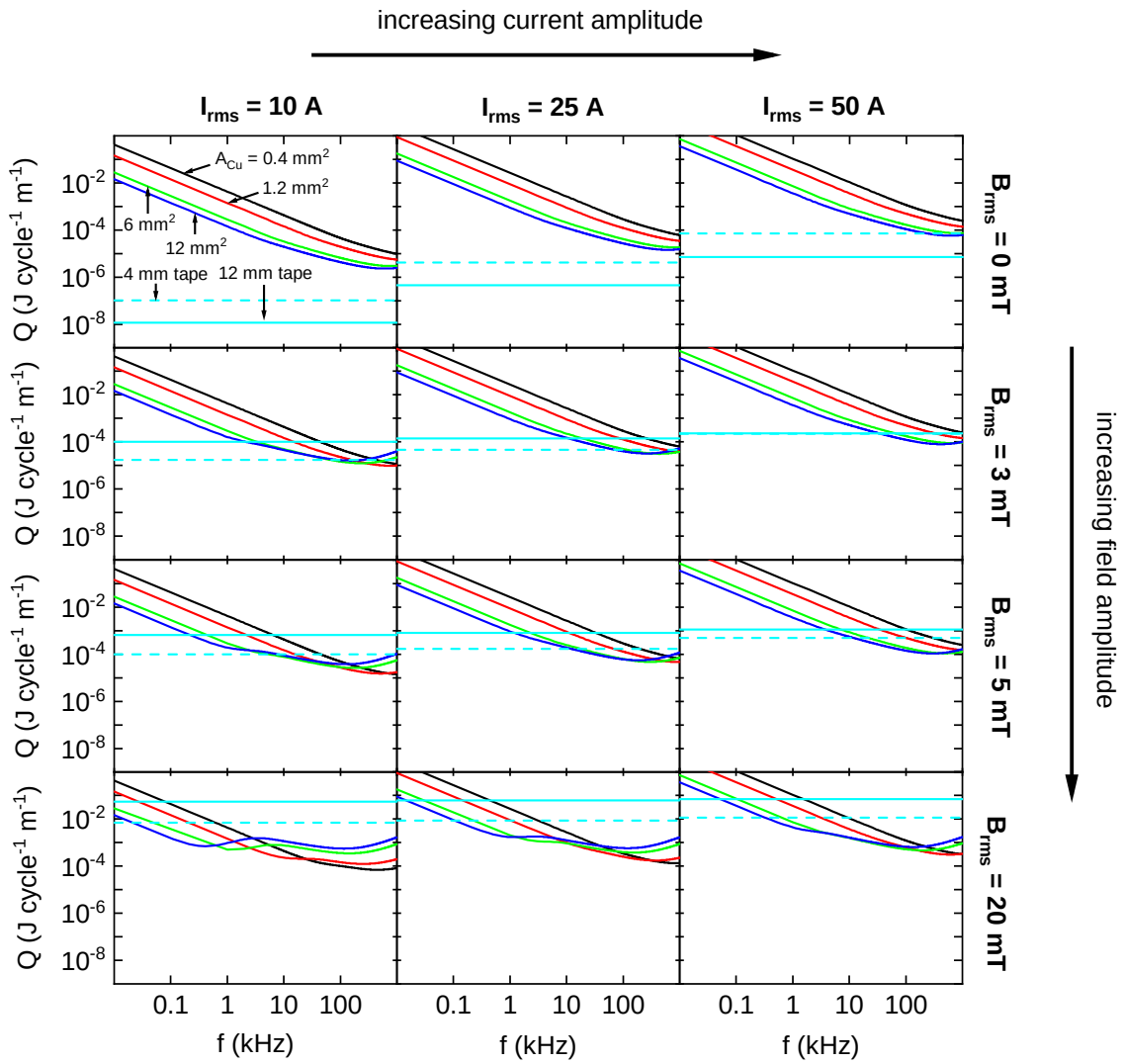

Figure 4.12: Comparison of the AC loss in typical litz wires and HTS tapes at a selection of interesting operating conditions. The total AC loss under the action of current and field is plotted against the frequency for 4 different litz wires and 2 different HTS tapes. The litz wire types A, B, C and D, as defined in Tab. 4.3, are shown as black, red, green and blue solid lines. The HTS tapes A and B, as defined in Tab. 4.4, are shown as dashed magenta and solid magenta lines. The applied transport current increases from left to right (10 A, 25 A and 50 A). The external magnetic field increases from top to bottom (0 mT, 3 mT, 5 mT and 20 mT).

Chapter 5

AC Power Losses in the Ferromagnetic Core

Besides the AC loss in the windings, the ferromagnetic loss in the core is the second challenge that must be considered very carefully when designing a WPT system. Even though the magnetic path in the core is interrupted by the air gap between the coils, the flux densities in a high permeability core are still large and lead to significant power loss.
The magnetic loss mechanisms can be divided into three main contributions [141]. Hysteresis loss, eddy current loss and residual loss. The hysteresis loss originates from the irreversible and spontaneous movement of domain walls during a change of magnetization (Barkhausen jumps). The eddy current loss depends on the conductivity and the spatial dimensions of the magnet. The residual loss arises from relaxation processes in excited magnetic systems due to spin-spin and spin-lattice interactions. On a macroscopic scale, the latter ones only become significant in the limit $B \to 0$ and $f \to 0$, i.e. when hysteresis and eddy current losses vanish [142] and are therefore not further considered in this thesis.
In order to reduce the loss in the core to an acceptable level, WPT coils apply magnetically soft power ferrites. At room temperature, these ferrites have a very narrow hysteresis loop and show nearly reversible magnetization behavior. However, with decreasing temperature, the hysteresis loop broadens and the magnetization behavior changes from soft to hard. In order to understand and to quantify the AC loss in power ferrites (at cryogenic temperatures), we present in Sec. 5.1 their fundamental properties, and we perform in Sec. 5.2 an experimental low temperature characterization.

5.1 Properties of Magnetically Soft Power Ferrites for WPT Applications

Commercially available power ferrites consist of MnZn or NiZn compositions and are optimized for the operation at room temperature. As long as the field excitation is harmonic, the total loss per unit volume, including hysteresis and eddy current loss, can be calculated with the empirical

Steinmetz equation [143]

$$\frac{P}{V} = C_{\mathrm{m}} f^{\alpha} B^{\beta} \,, \tag{5.1}$$

where f is the frequency, B is the peak amplitude of the alternating magnetic flux density in the core and C_{m}, α and β are the Steinmetz parameters. The Steinmetz parameters, can be extracted from experimental measurements and are typically valid in a limited range of frequency and field amplitude.
In order to estimate the AC loss in a given core geometry, the exact field distribution inside the core must be solved with numerical methods and Eq. (5.1) must be integrated over the core volume. Such a numerical simulation, in turn, requires a precise knowledge of the intrinsic permeability of the core ($B \propto \mu_0 \mu_{\mathrm{r}} H$).
Due to the fact that both, the Steinmetz parameters and the permeability, show a strong temperature dependence, the loss calculation at low temperatures becomes challenging. Manufacturers provide measurement data only in a limited temperature range from $T = -40\,^{\circ}\mathrm{C}$ to $T = 150\,^{\circ}\mathrm{C}$. Beyond these limits the permeability and the AC loss of the core are not known. In the following, we discuss shortly the physical origin of the temperature dependence.
The B-H loop, which defines the hysteresis loss per unit volume, is determined by the saturation flux density (B_{s}), the remanence flux density (B_{r}) and the coercivity field strength (H_{c}), which by themselves depend on the temperature. With decreasing temperature, B_{s} increases according to the Bloch law [142], B_{r} increases due to a change of the magnetostriction constants [144] and H_{c} increases due to an increase of the magnetocrystalline anisotropy energies [144]. Due to these effects, the total hysteresis loss increases with decreasing temperature [145]. The eddy current loss on the other hand becomes less significant at low temperatures. As the intrinsic conductivity of ferrites decreases exponentially with decreasing temperature, no eddy current losses are to be expected at cryogenic temperatures.

Experimental data from literature [146–148] suggests that the hysteresis loss in commercially available ferrites increases by a factor of 10 when the temperature is decreased from 300 K to 77 K. This is obviously a huge drawback for superconducting WPT coils, because we must expect that the loss in the core will exceed the loss of the winding.
The only alternative core material that could be considered instead of ferrite, is an Fe-based nanocrystalline alloy (Metglas). This alloy is produced as a thin metallic ribbon which needs to be stacked and wound to form a core. According to literature [146], the hysteresis loss in Metglas at cryogenic temperatures is only increased by a factor of 3 compared to room temperature. Very recently, significant efforts have been made to further optimize these alloys for low temperature applications [149–151], which would make them even more interesting. Unfortunately, Metglas can not be used in WPT coils because it has a very low specific resistivity ($\rho \sim \mu\Omega\,\mathrm{m}$) which would lead to huge eddy current losses. Additionally, the production of magnetic cores from Metglas is much more complex and costly than the simple production of ferrite cores, which can be produced in arbitrary shapes at very low cost.
So due to a lack of alternative materials, we perform in the following a low temperature characterization of a selected soft power ferrite. Among the vast amount of commercially available power ferrites, we have chosen a material which shows, according to the datasheet, a good

performance at temperatures below room temperature. With a permeability of $\mu_r^{-40\,°C} = 2500$ and a power loss of $P_V^{-40\,°C} = 500\,\mathrm{mW/cm^3}$ (at 200 mT and 100 kHz), the material DMR95 from the manufacturer DMEGC exceeds the performance of most other material compositions and was therefore selected to be studied at cryogenic temperatures.

5.2 Experimental Low Temperature Characterization

5.2.1 Experimental Methods

In order to gain a full understanding of the low temperature properties of the DMR95 power ferrite, we have analyzed three samples with different shapes under various operating conditions. Therefore, we have applied three different experimental methods. First, we have used an industrial B-H-analyzer (Bs&T Pro System) to measure the hysteresis loop in a toroidal ring core. Second, we have used a highly sensitive SQUID* magnetometer (MPMS XL-7) to measure the hysteresis loop of a small bulk sample. Third, we have used a calibration free AC loss set-up to measure the power loss of a flat I-type core segment in an external AC field. All methods are described in the following.

B-H-Analyser (ring core)

The industrial B-H analyzer provides fully automated hysteresis loss measurements in a temperature range from $T = -60\,°C$ (215 K) to $T = 150\,°C$ (425 K). Due to the fact that no liquid nitrogen was available at the location of the analyzer, we were not able to extend the temperature range beyond $-60\,°C$. The measurements in this temperature range have been performed mostly to verify the values from the datasheet.

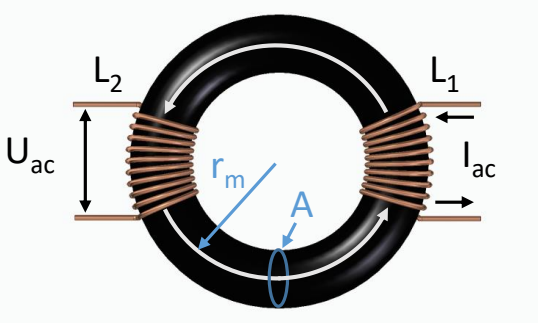

Figure 5.1: Experimental technique of B-H-analysis on a toroidal ring core.

The ring core with cross section A and average radius r_m is equipped with a primary winding L_1 to create a field excitation in the core and with a secondary winding L_2 to measure the magnetic response. For simplicity, both windings have N turns. L_1 is connected to an AC power amplifier, which supplies a sinusoidal current I_{AC}. The current in L_1 results in a well known magnetic field strength of $H = NI_{AC}/(2\pi r_m)$, which causes an unknown magnetic flux density B in the core. The flux density is measured with L_2 and the hysteresis curve is given by plotting B as a function of H.

Besides the B-H-analysis, the ring core sample can be used to determine the relative permeability μ_r. The winding on the toroidal ring core has a well known inductance of $L = \mu_0\mu_r N^2 A/(2\pi r_m)$. A simple measurement of the inductance L allows therefore direct extraction of μ_r. This inductive

* Superconducting Quantum Interference Device

method can be performed with simple measurement equipment, which allowed us to measure the value of μ_r also in liquid nitrogen at $T = 77\,\mathrm{K}$.

SQUID Magnetometer (bulk sample)

A SQUID magnetometer is a highly sensitive measurement device, which allows to determine the overall magnetic moment of small bulk samples and thin films in absolute units with a sensitivity of $1 \cdot 10^{-11}\,\mathrm{Am}^2$ [152]. Based on quantum interference, the smallest changes of the magnetic flux can be converted into a change of voltage. For our measurements, we used the MPMS XL-7 SQUID magnetometer at the Walther-Meissner-Institute in Garching. The experimental setup is depicted schematically in Fig. 5.2.

The sample is glued into the sample holder and positioned in the sample chamber. The temperature in the sample chamber can be controlled in a range from $T = 1.8\,\mathrm{K}$ to $T = 400\,\mathrm{K}$. An external DC magnet provides at the sample position a homogeneous field strength of $|\mu_0 H| < 7\,\mathrm{T}$. The magnetic moment of the sample in the external DC field is measured by moving the sample up and down through a second order gradiometer, which cancels the contribution of the DC field and of the sample holder. The change of magnetic flux is coupled into the SQUID loop where it is converted into a voltage signal and amplified by the internal electronics. The projection of the magnetic moment, onto the axis of the external field, can finally be deduced from the voltage versus sample position curve [152]. By sweeping the external field strength, a quasi static hysteresis loop can be obtained. Repetition of the measurement at different temperatures allows to show the temperature dependence of the magnetic properties of the sample.

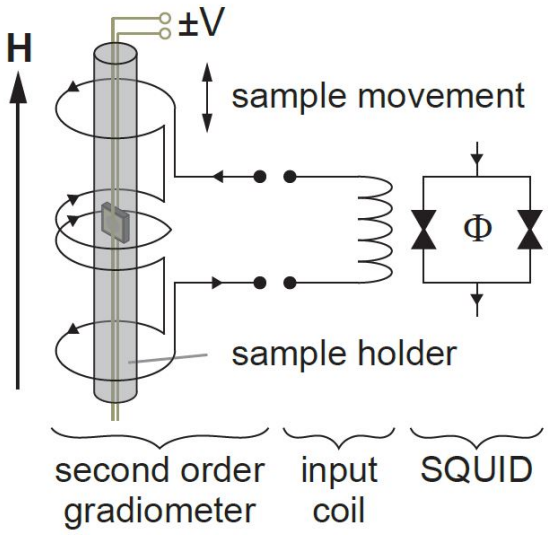

Figure 5.2: Experimental technique of SQUID-magnetometry of small bulk samples. Figure taken from [152].

Calibration Free AC Loss Measurement (arbitrary shape)

The calibration free AC loss measurement setup, which is located at the Institute of Electrical Engineering in Bratislava, allows to measure the magnetization loss of arbitrarily shaped samples in an external AC field in absolute units. The method is based on the fact that the AC loss, which is dissipated in the sample, must be supplied by the power source, which drives the magnetic field [153]. Therefore, by measuring the energy flow from the source into the measurement device, the loss of the sample can be extracted. In a simple setup, the measured value would contain two loss contributions, the power loss of the sample and the parasitic loss of the measurement device itself. By using the calibration free setup, as depicted in Fig. 5.3, the contribution of the measurement device can however be canceled out. The setup consist of two AC magnets, which have exactly the same geometry, are positioned next to each other, and are connected in series.

One of them contains the sample, the other one remains empty. The voltage pick-up loops of both magnets are connected in anti-series configuration in such a way that the parasitic loss contributions cancel each other and only the signal from the sample remains.
The complete setup needs to be cooled with liquid nitrogen, so measurements are only possible at a fixed temperature of $T = 77\,\mathrm{K}$. We note that in this method, the magnetic AC loss of the sample is measured as a function of the external field amplitude, not as a function of the magnetic flux density in the sample, as it was the case in the B-H-analyzer. The flux density in the sample is explicitly not known in this method. Depending on the shape of the core and its orientation relative to the external field direction, the flux density in the core and hence also the power loss may differ.
Comparisons to the results of the ring core (B-H-analyzer) are only possible if the magnetic flux density in the measured sample is estimated by calculation or simulation.

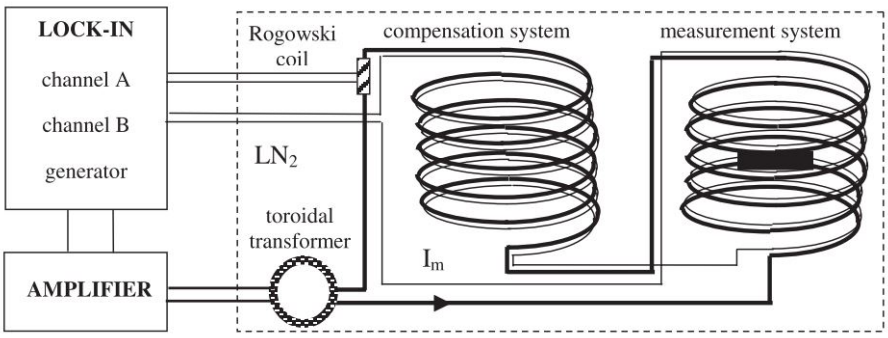

Figure 5.3: Experimental setup of the calibration free AC loss measurement. The sample is positioned in an AC magnet, which is driven by an external power source. The power loss of the sample is measured with a voltage pickup loop that is co-wound with the winding of the magnet. The parasitic loss contribution of the measurement system is canceled out by using a second, identical AC magnet as compensation. The compensation system does not contain a sample and the voltage pickup loops of both magnets are connected in anti-series configuration. The measurement signal is detected with a lock-in amplifier. Figure taken from [153].

5.2.2 Experimental Results

First, we have measured the B-H curve of the toroidal ring core sample at different temperatures and at different field amplitudes. The major hysteresis loop and two minor loops are shown exemplary at temperatures of $T = 300\,\mathrm{K}$ and $T = 215\,\mathrm{K}$ in Figs. 5.4 (a) and (b), respectively. The initial magnetization curve is defined by the tips of all minor loops and was fitted to the measurement data as described in [154]. It is shown in Fig. 5.4 as a black dashed line. We see that the power ferrite behaves at room temperature perfectly soft magnetic with a small hysteresis loop. With decreasing temperature, the hysteresis loop broadens strongly. At 215 K, the sample can already be considered as magnetically hard. The remanence flux density is increased by a factor of 4, and the coercivity field strength is increased by a factor of 5, compared to 300 K.
We determine the power loss per unit volume by analyzing the enclosed area of the hysteresis loops and find that the power loss at 215 K is increased by a factor of 20 ($B = 100\,\mathrm{mT}$) and by

a factor of 6 ($B = 400\,\mathrm{mT}$), compared to 300 K. We will show the power loss as a function of the magnetic flux density in Fig. 5.7 (b), where we compare the result of the *B-H* analyzer to the results of the calibration free setup.
We further observe in Fig. 5.4 that the slope of the initial magnetization curve, which corresponds to μ_r in the limit $H \to 0$, decreases with decreasing temperature. A detailed analysis of μ_r as a function of the temperature is presented in Fig. 5.6 (a). We see that μ_r decreases very strongly between 200 K and 300 K. At 77 K, μ_r reaches an extremely low value of $\mu_\mathrm{r}^{77K} = 35$.

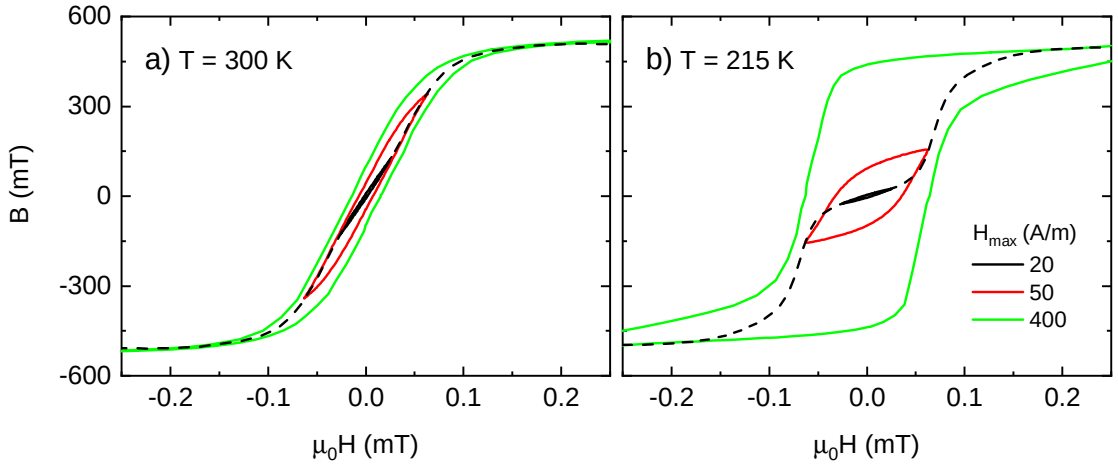

Figure 5.4: *B-H* hysteresis loop of the ring core. The major loop and two minor loops at field excitations of $H_\mathrm{max} = 20\,\mathrm{A/m}$, 50 A/m and 400 A/m are shown. In (a) and (b), the results at $T = 300\,\mathrm{K}$ and $T = 215\,\mathrm{K}$ are compared. The initial magnetization curve, which connects the tips of all minor loops, is fitted to the measurement data according to [154] and is shown as a dashed line.

Second, we have used the SQUID magnetometer to measure the *B-H* curve of a small bulk sample, which was cut out of the ring core. The sample has a cubic shape, a volume of $V = 2\,\mathrm{mm}^3$ and a mass of $m = 10\,\mathrm{mg}$. The *B-H* curves at various temperatures between $T = 20\,\mathrm{K}$ and $T = 350\,\mathrm{K}$ are shown in Fig. 5.5. We observe that the *B-H* behavior of the bulk sample differs strongly from the one of the ring core. While for the case of the ring core, a field excitation of $\mu_0 H = \pm 1\,\mathrm{mT}$ was sufficient to drive the magnetization into saturation, a field of nearly $\mu_0 H = \pm 1\,\mathrm{T}$ is required for the case of the bulk sample. Nevertheless, the results are not in contradiction to each other. The difference can be explained by the fact that the magnetic path is closed in the ring core and open in the bulk sample. An open magnetic path results in large demagnetizing fields, which reduce the magnetization of the sample. The effective permeability of the bulk sample is therefore far below the intrinsic value ($\mu_\mathrm{eff} \approx 10 \ll \mu_\mathrm{r}$).
The analysis of the measured *B-H* curves allows further to extract the temperature dependence of the saturation flux density B_s. We observe that B_s does not depend on the sample geometry and we plot the result in Fig. 5.6 (b). The measured values agree excellently with the available datasheet values and B_s increases with decreasing temperature as predicted by the Bloch law [155]

$$B_\mathrm{s}(T) = B_\mathrm{s}(0)\left(1 - \frac{T}{T_0}\right)^{3/2}, \tag{5.2}$$

where $B_s(0)$ is the saturation flux density at $T = 0\,\mathrm{K}$ and T_0 is the Curie-temperature.
An analytic fit of Eq. (5.2) to our measurement data allows to extract the fit parameters $B_s(0) = 852\,\mathrm{mT}$ and $T_0 = 576\,\mathrm{K}$. The saturation flux density at 77 K is $B_s^{77\,\mathrm{K}} = 820\,\mathrm{mT}$.
It is interesting to observe that our measurements with the SQUID magnetometer were not able to resolve the hysteresis loop of the B-H curve. The up-sweep and the down-sweep of each quasistatic cycle are identical. This means that the small bulk sample has no magnetic memory and seems to be free of loss. We assume that a hysteresis loop and the according AC loss would appear if the frequency was increased. The measurement of a single B-H curve with the SQUID magnetometer takes about 2 hours and is therefore performed effectively at $f = 0\,\mathrm{Hz}$.

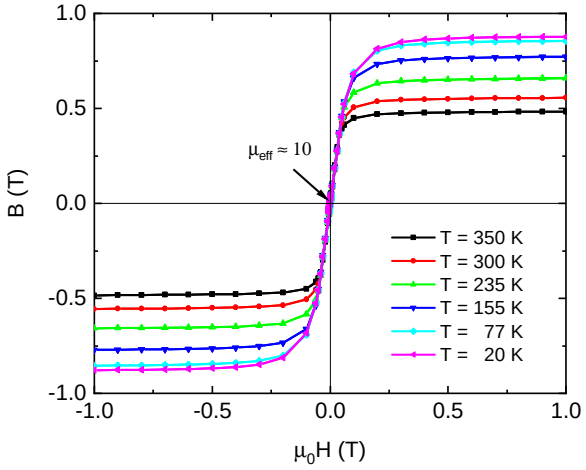

Figure 5.5: Quasistatic B-H hysteresis loops of the small rectangular bulk sample, which was cut out from the ring core. The hysteresis loops are measured with the SQUID magnetometer and are shown at different temperatures in the range from $T = 20\,\mathrm{K}$ to $T = 350\,\mathrm{K}$. The bulk sample has an effective permeability of $\mu_{\mathrm{eff}} = 10$ and the magnetization process is completely reversible. The saturation flux density follows the Bloch law with a $(1 - T/T_0)^{3/2}$ dependence.

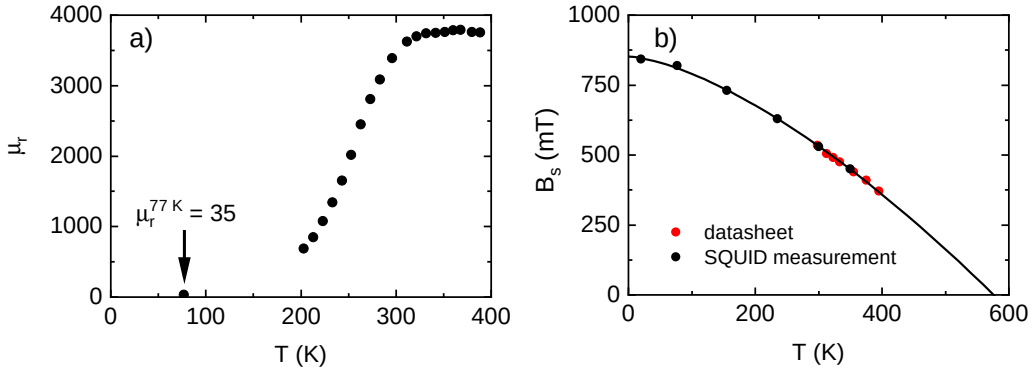

Figure 5.6: Low temperature properties of the experimentally characterized power ferrite. The intrinsic relative permeability μ_r and the saturation flux density B_s are shown as a function of temperature in (a) and (b), respectively. The solid line in (b) corresponds to the analytical fit of the Bloch law according to Eq. (5.2). Although the values of B_s increase with decreasing temperature, the strong decrease of μ_r makes it impractical to use a cold ferrite core in power inductors.

Lastly, we have applied the calibration free AC loss setup to measure the exact power loss per unit volume at $T = 77\,\mathrm{K}$. We have learned from the above measurements that the internal magnetic flux density depends strongly on the shape of the sample. As the power loss scales with the internal flux density, it is clear that two differently shaped samples will cause different power loss when exposed to the same external AC field. Due to the fact that the magnetic core of our WPT coils will not be a single piece, but will be assembled from several small segments (compare Fig. 6.3), it is of special interest to know the AC loss of such a segment.
The length, the width, the thickness and the volume of one segment are $l = 45\,\mathrm{mm}$, $w = 13\,\mathrm{mm}$, $t = 2.5\,\mathrm{mm}$ and $V = 1.463\,\mathrm{cm}^3$, respectively. We have measured the power loss of this sample in parallel and in perpendicular field at frequencies of 36 Hz and 72 Hz. The power loss per cycle per cm^3 is plotted against the externally applied magnetic field B_{ext} in Fig. 5.7 (a).
As expected, we see that the power loss is frequency independent and therefore of purely hysteretic nature. We see that the measurements in parallel and in perpendicular field differ by more than a factor of 10. With this result we can already approximate the power loss in the core of a WPT coil. By estimating the magnetic field, that is generated by the coil, we can calculate the loss for each individual core segment. It is however often useful to know also the power loss as a function of the internal flux density in the sample. Therefore, we have performed numerical simulations to determine the effective permeability of the measured ferrite sample. For the cases of parallel and perpendicular field, we have found $\mu_{\mathrm{eff}} \approx 20$ and $\mu_{\mathrm{eff}} \approx 4$, respectively. With the approximation $B = \mu_{\mathrm{eff}} B_{\mathrm{ext}}$, we can determine the internal magnetic flux density in the sample and plot the power loss against B in Fig. 5.7 (b). We see in this plot that the results from both

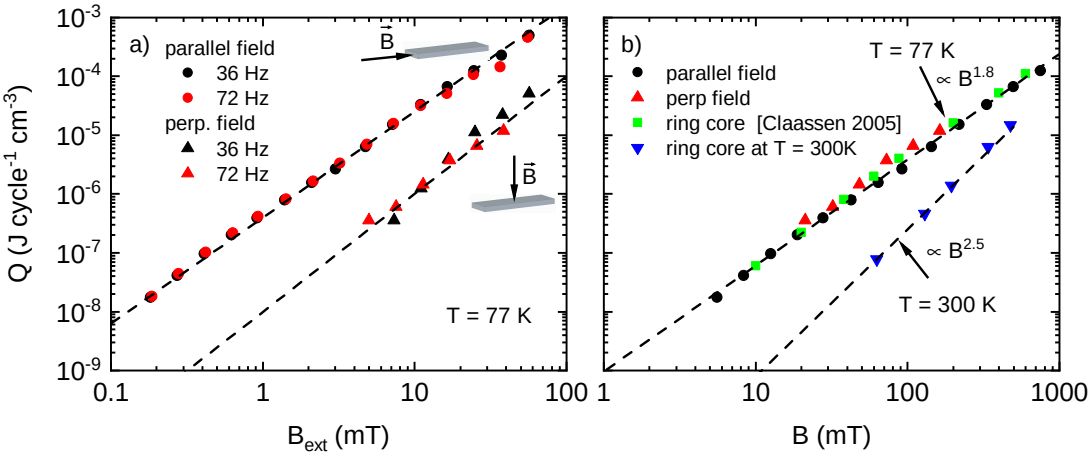

Figure 5.7: Field dependence of the magnetic AC loss in a flat ferrite bar under the action of external magnetic AC field. (a) The loss, as measured with the calibration free setup in parallel and in perpendicular field, is plotted against B_{ext} at two different frequencies. (b) The same measurement is plotted against the internal flux density in the sample ($B \approx \mu_{\mathrm{eff}} B_{\mathrm{ext}}$), where μ_{eff} was estimated numerically for both field directions. In this representation, the measurements in perpendicular and in parallel fields agree with each other and with the literature result from [146]. For comparison, we also show the room temperature measurement, which was obtained with the B-H analyzer on the ring core sample. The dashed lines in both panels are fitted to the measurement data and indicate the slope.

field directions coincide with each other. This is a strong indication that the loss measurement and the estimation of the flux density in the sample are correct. Additionally, our measurement results agree also with experimental data from literature [146]. Comparison of the measurement results at 77 K (calibration free setup) and at 300 K (B-H analyzer) reveals that the cold and the warm core have a different field dependence. They scale with $B^{1.8}$ and $B^{2.5}$ respectively. The power loss in the cold core is strongly increased, compared to room temperature. At small field amplitudes by more than a factor of 100, at large amplitudes still by a factor of 10.
We conclude this section by extracting the Steinmetz parameters of our ferrite material (DMR95, DMEGC) at 77 K from the measurement data. The result in Fig. 5.7 (b) is independent of the sample shape and can be fitted easily with Eq. (5.1). The Steinmetz parameters to calculate the power loss in $\mathrm{W/m^3}$ are $C_\mathrm{m} = 240$, $\alpha = 1$ and $\beta = 1.8$. With the Steinmetz parameters being known, we can use a standard method to calculate the magnetic loss in the core of our WPT coils. We will determine the flux density inside the core numerically and integrate the Steinmetz equation over the core volume in Chap. 6.

Chapter 6

Design and Optimization of HTS Coils for WPT Systems

In this chapter, we present the design of the superconducting transmission coils of the WPT system. The key figures of merit for high power applications are the efficiency (η) and the power density (α). During our review of the parameter interdependencies of state-of-the-art WPT coils in Sec. 1.2, we have seen that both performance goals can not be achieved simultaneously. The conventional technology is trapped in the so called η-α-Pareto front, where an increase of the power density results in an inevitable decrease of the efficiency.
Our coil design, based on superconducting tapes, aims to overcome this Pareto front. As discussed in Chap. 2, a high transmission efficiency requires large quality factors (Q-factor) and strong magnetic coupling factors (κ). If we increase the power density by reducing the coil size, a decrease of κ can not be avoided at the same coil distance. Nevertheless, by applying HTS tapes, we hope to realize very large Q-factors in the small winding space. The large Q-factors would allow to compensate the reduced coupling strength and keep the efficiency high, even in a very compact coil design. If the coil distance is reduced by the same factor as the coil size, κ remains high and extremely efficient systems across small air gaps could be expected.

In order to achieve the desired Q-factors, the coil design must be systematically optimized for low AC losses. We introduce, in Sec. 6.1, the fundamental coil design and we define the target parameters of our 11 kW WPT system. In Sec. 6.2, we introduce a semianalytical and a fully analytical method to calculate the AC loss of the winding. We apply both methods to study the coil design. Based on the calculation result, we define two optimized coil designs for the operation at high and at low frequencies. In Sec. 6.3, we shortly discuss alternative AC loss calculation methods, which are typically used in literature.

6.1 Fundamental Coil Design

In order to significantly exceed the power density of state-of-the-art WPT coils, we set ourselves the ambitious target of outperforming the best literature result by a factor of two. Taking the values from [28] as reference, we aim to achieve an area-related power density of $\alpha = 3\,\mathrm{kW/dm^2}$

and a weight-related power density of $\rho = 4\,\mathrm{kW/kg}$. To achieve these values at a maximum output power of 11 kW, the upper limits for the area and the weight of the coil are $3.66\,\mathrm{dm}^2$ and 2.75 kg, respectively. For the case of a circular coil design, the maximum coil radius is $r_{\mathrm{out}} = 10.8\,\mathrm{cm}$. With the coil size being fixed, we need to define the inductance of the transmission coils. According to Eq. 2.14, the coil inductance must satisfy $L = R_{\mathrm{L,eq}}/\omega_{\mathrm{r}}\kappa$. The optimum load resistance of our WPT system at full power is $R_{\mathrm{L,eq}} \approx 6.7\,\Omega$ (compare Chap. 2). For the magnetic coupling factor, i.e. the distance between the transmission coils, we have chosen an initial design value of $\kappa = 0.5$. During our experiments, we will be able to vary κ slightly in both directions, by increasing or decreasing the distance between the coils. With these boundary conditions, the only remaining parameter is the operating frequency. At frequencies of 100 kHz, 10 kHz, 1 kHz the required inductance is given by 21.5 µH, 215 µH and 2.15 mH, respectively. The challenge of finding the best ratio between inductance and frequency requires a detailed loss analysis and will be discussed in Sec. 6.2.

Before optimizing the winding, we first present the fundamental coil design.

A typical WPT coil consists of a planar, rotationally symmetric, spiral shaped winding. Such a winding scheme can easily be realized with superconducting tapes and is known in literature as a single pancake coil. We show a 3D picture of the winding in Fig. 6.1. The winding is parameterized by the inner coil radius r_{in}, the outer coil radius r_{out}, the number of turns n, the intertape spacing d, the thickness of the HTS tape t and the width of the HTS tape w.

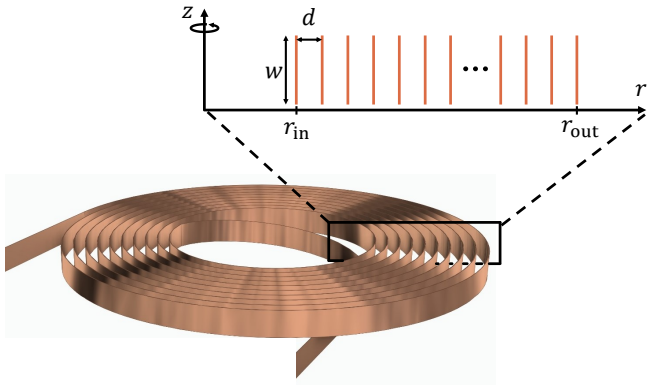

Figure 6.1: Winding design of a rotationally symmetric single pancake coil. In cylindrical coordinates, the winding is parameterized by the inner coil radius r_{in}, the outer coil radius r_{out}, the number of turns n, the intertape spacing d, the thickness of the HTS tape t and the width of the HTS tape w

The outer coil radius is fixed by the desired power density to $r_{\mathrm{out}} = 10.8\,\mathrm{cm}$. The inner coil radius depends on multiple design considerations. In order to maximize κ, the inner radius should satisfy $r_{\mathrm{in}}/r_{\mathrm{out}} \leq 0.5$ [16]. In order to maximize the available winding space, r_{in} should be as small as possible. And finally, in order to avoid the critical bending diameter of the tape, $r_{\mathrm{in}} > 2.5\,\mathrm{cm}$ must be satisfied. Taking into account that the innermost turns contribute only little to the total inductance, $r_{\mathrm{in}} = 5\,\mathrm{cm}$ was chosen. The available winding space, defined by r_{in} and r_{out}, has a width of 5.8 cm and can hold a maximum of 580 turns, if $t = 100\,\mu\mathrm{m}$ and $d \to 0$. With such a large number of turns, inductances of several mH can realistically be achieved. Nevertheless, we must keep in mind that a large inductance also leads to large magnetic fields,

which reduce the critical current of the tape (compare Fig. 3.3).

If the innermost turn is numbered as turn 1, and n is small enough, so that $nt \ll (r_{\mathrm{out}} - r_{\mathrm{in}})$, the intertape spacing is given by

$$d = \frac{r_{\mathrm{out}} - r_{\mathrm{in}}}{n}\,, \tag{6.1}$$

the average radius of the i$^{\mathrm{th}}$ turn is given by

$$r_i = r_{\mathrm{in}} + \left(i - \frac{1}{2}\right) d\,, \tag{6.2}$$

the length of the i$^{\mathrm{th}}$ turn is

$$l_i = 2\pi r_i\,, \tag{6.3}$$

and the total length of the complete winding is

$$l_{\mathrm{tot}} = \sum_{i=1}^{n} l_i\,. \tag{6.4}$$

The inductance and the field distribution of such a winding can in principle be calculated analytically. For reasons of simplicity, we use here, however, numerical FEM simulations (Ansys Maxwell). With the simulation setup, as described in Appendix A.2, the properties of coupled coil pairs can be determined within a few seconds.
When varying the number of turns in the given winding space, we see that $l_{\mathrm{tot}} \propto n$, $d \propto 1/n$ and $L \propto n^2$. In order to further increase the inductance for a given number of turns, the winding can be mounted onto a magnetic core. Because the magnetic path of the core is not closed, the inductance scales not linearly with μ_{r}. In the limiting case of a solid, thick, high permeability ferrite plate, the inductance can, in the best case, only be increased by a factor of 2 [156]. Considering the large weight of the ferrite core, this performance gain is very small and an application without core could be beneficial. In most realistic applications, the ferrite is however required to shield the stray fields of the coil. In order to optimize the weight-related power density, it is a common practice to use a segmented core structure instead of a solid ferrite plate [157]. As the segmentation of the core breaks the rotational symmetry of the coil, we used a full 3D simulation model as described in Appendix A.3. We found that a star shaped core structure of 24 narrow, and evenly spaced ferrite bars with a thickness of 2.5 mm (compare Fig. 6.3) provides best performance. The volume has been chosen large enough, so that the core does not saturate at full power. The total mass of the core is $m_{\mathrm{core}} = 258\,\mathrm{g}$.
To demonstrate the shielding effect of the core, we compare in Fig. 6.2 the flux lines of a coupled coil pair (a) with and (b) without magnetic core.
We further show in Fig. 6.3 (a) the bottom view of the segmented core structure, and in Fig. 6.3 (b), the magnetic flux density inside the core at 77 K. The winding is assumed to have 10 evenly distributed turns and the current at full power is assumed to be $I_{\mathrm{rms}} = 36\,\mathrm{A}$.
At 77 K, the permeability of the applied MnZn power ferrite is $\mu_{\mathrm{r}}^{77\,\mathrm{K}} = 35$ and the saturation flux density is $B_{\mathrm{s}}^{77\,\mathrm{K}} = 820\,\mathrm{mT}$ (compare Chap. 5). Due to the small value of μ_{r}, the core increases the inductance of the winding only by a factor of 1.2. The peak flux density in the

core is $B = 100\,\mathrm{mT} \ll B_\mathrm{s}$ and the resulting magnetic power loss at 100 kHz is $P_\mathrm{core}^{77\,\mathrm{K}} \approx 10\,\mathrm{W}$.

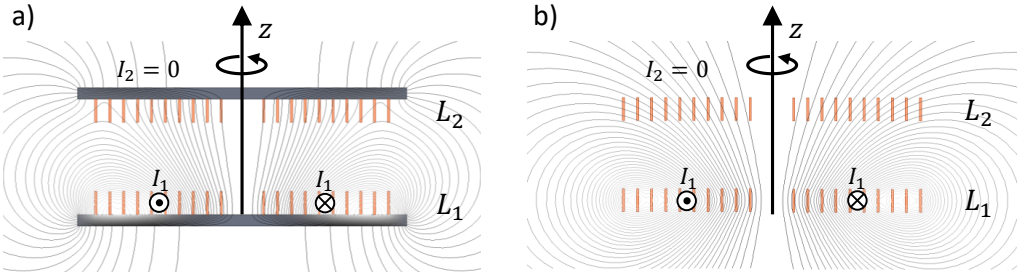

Figure 6.2: Shielding effect of the magnetic core. The flux lines of a coupled coil pair (a) with and (b) without magnetic core, are compared to each other.

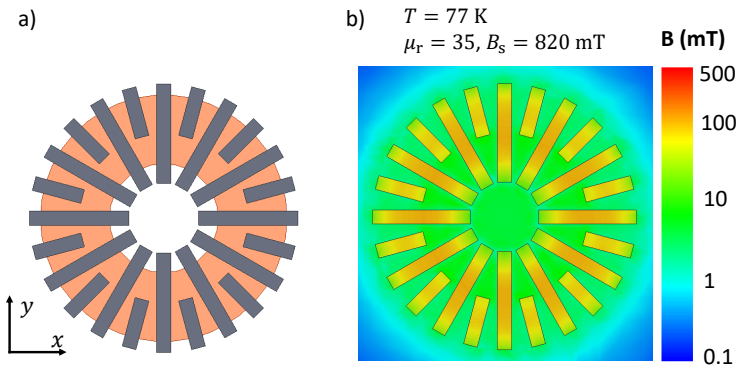

Figure 6.3: (a) Bottom view of the WPT coil with a segmented magnetic core. The ferrite segments are gray, the winding space is orange. In (b), the magnetic flux density inside the core segments is evaluated at 77 K. The magnetization of the core remains below B_s. The winding is assumed to have 10 evenly distributed turns and the current at full power is assumed to be $I_\mathrm{rms} = 36\,\mathrm{A}$.

6.2 AC Loss Optimization of the HTS Winding

With the fundamental coil design being defined, we will now calculate and optimize the AC loss of the winding. We have introduced, in Chap. 4, analytical and numerical methods to calculate the AC loss of infinitely long straight HTS tapes under the action of current and field. For the case of the coil winding, we face now the problem that the turns are exposed to the self-field of the complete coil. The amplitude and the angle of the magnetic field varies inside the winding and the AC loss must be solved individually for each turn. In the same way as in Chap. 4, we distinguish between the low- and the high-frequency regime.
In the low-frequency regime, we consider only the hysteresis loss, and in the high-frequency regime, we consider only the eddy current loss. In the following, we introduce the calculation methods for HST coils and in Sec. 6.2.2, we apply the methods to find the optimum coil design. We will verify all results experimentally in Chap. 8.

6.2.1 Calculation Methods

Low-frequency regime: hysteresis loss

1. Semianalytical method

In the semianalytical method, we compute the magnetic field distribution of the winding with the simulation setup as described in Appendix A.2. We assume that the exact current distribution in the HTS tapes does not significantly influence the overall magnetic field distribution of the complete coil, and we model the HTS tape as a single thin strip that carries a uniform current density. Once the field distribution is known, we use the analytical Schönborg equation (4.11) to calculate the hysteresis loss for each turn individually. The loss per unit length in the i^{th} turn is given by

$$Q_{\mathrm{i}} = Q_{\mathrm{Schoenborg}}(I_{\mathrm{tr}}, B_{\perp,\mathrm{i}}) \,, \tag{6.5}$$

where $B_{\perp,\mathrm{i}}$ is the perpendicular magnetic field component penetrating the i^{th} turn.
As the amplitude and the direction of the magnetic field may vary locally along the width of the tapes, $B_{\perp,\mathrm{i}}$ is determined by averaging the value of $B_{\perp}$ across the width. Due to the fact that the input parameter for the Schönborg equation is only the externally applied field, the self-field contribution of the turn under study must be subtracted from $B_{\perp,\mathrm{i}}$. The average hysteresis loss per cycle and unit length of the complete coil is given by

$$Q_{\mathrm{hyst}} = \frac{\sum_{i=1}^{n} l_{\mathrm{i}} Q_{\mathrm{i}}}{\sum_{i=1}^{n} l_{\mathrm{i}}} \,. \tag{6.6}$$

As the strict assumption of a uniform current density does not reproduce the exact field distribution in the direct vicinity of the tapes and neglects shielding currents between the turns, we expect that this method overestimates the loss in tightly wound coils ($d \to 0$). For HTS windings with sufficiently large inter-tape spacings, however, our method allows for a very fast and simple estimation of the AC loss. The assumption of a uniform current density reduces the computation time for complex 3D structures to a few seconds on a normal PC.

We note that we have verified the validity of the semianalytical approach in [117]. In this reference, we have shown that the AC loss behavior of conventional WPT coils can be predicted by combining numerically field simulations with the analytical litz wire model, as introduced in Sec. 4.1.

2. Fully analytical method

The fully analytical approach is a very elegant method of estimating the loss in a single pancake coil. Instead of considering the exact geometry of the winding, the coil is approximated by an infinite stack of parallel tapes. All tapes in the stack carry the same transport current and are insulated from each other. For such a stack in its self-field, an analytical solution has been derived by K.-H. Müller [158]. The loss per tape, unit length, and cycle, is given by

$$Q_{\mathrm{hyst}} = \frac{2\mu_0}{\pi^3} I_{\mathrm{c}}^2 \, F\left(\frac{d}{w}, \frac{I_{\mathrm{tr}}}{I_{\mathrm{c}}}\right) \,, \tag{6.7}$$

with

$$F = \int_{\tilde{\eta}}^{\pi w/2d} \left(\frac{\pi w}{2d} - \eta\right) \operatorname{arctanh}\left(\frac{\tanh^2\eta - \tanh^2\tilde{\eta}}{\tanh^2(\pi w/2d) - \tanh^2\tilde{\eta}}\right)^{1/2} \mathrm{d}\eta\,, \tag{6.8}$$

and

$$\tilde{\eta} = \operatorname{arccosh}\left(\frac{\cosh(\pi w/2d)}{\cosh(\pi w I_{\mathrm{tr}}/2dI_{\mathrm{c}})}\right)\,. \tag{6.9}$$

Eq. (6.7) shows that the hysteresis loss in an infinite stack of tapes depends only on the ratios $I_{\mathrm{tr}}/I_{\mathrm{c}}$ and d/w. Due to symmetry reasons, all tapes of the stack exhibit exactly the same loss. The approximation is therefore valid, if the coil under study has a sufficiently large number of turns, so that the boundary effects in the innermost and outermost turns can be neglected.

High-frequency regime: Eddy current loss

In the high-frequency regime, we simulate the eddy current loss of the complete winding fully numerical. We use the simulation setup as described in Appendix A.2. The HTS tape is modeled as a m-s-strip (compare Sec. 4.2.2). The applied current flows entirely in the HTS layer and has a uniform current density. We assume explicitly that the current amplitude in the metal layer is zero, i.e. no current sharing between the layers is allowed. The induced currents in the metal layer are therefore pure eddy currents. The eddy currents in each turn are driven by the self-field of the AC transport current in the turn of study, and by the external field generated by all the other turns. We use the integrated calculation tools of the simulation software to determine the eddy current loss in all turns simultaneously.

6.2.2 Optimization Results

Obviously, Eq. (6.7) suggest that Q_{hyst} can be optimized by tuning d and w. In order to understand the exact influence of such tuning, we have applied the semianalytical and the fully analytical method. We have observed good agreement between both methods*, and we present in the following a detailed analysis of the results.

Firstly, we have studied the influence of w at a fixed value of d. Thereby, we have taken into account that a change of w simultaneously changes I_{c}. We have assumed that the tape quality is constant, i.e. $I_{\mathrm{c}} = wJ_{\mathrm{c}}$. In this case, we observe that Q_{hyst} decreases with increasing w and converges for $w > d$ towards the limiting case of a homogeneous superconducting slab [159]. This is true for any combination of d and I_{tr}. So the choice of w is straight forward. In single pancake coils, a wider tape always outperforms a thinner one. At a given value of d, we should choose w so that $I_{\mathrm{tr}} \ll I_{\mathrm{c}}$ and $w \geq d$. We emphasize that the loss does not merely depend on the ratio d/w. The loss at $d = w = 6\,\mathrm{mm}$ is larger than the loss at $d = w = 12\,\mathrm{mm}$, because $I_{\mathrm{c}} \propto w$. Therefore, any decrease of w does not help to reach small values of d.

Secondly, we have studied the influence of d at a fixed value of w. We show Q_{hyst} as a function of d at different values of I_{tr} in Fig. 6.4 (a). In agreement with [160], we observe that d is a very important parameter to optimize Q_{hyst}. In a tightly wound coil ($d \to 0$), the loss of the winding

* As the number of turns scales with $1/d$, and a large number of turns requires a large computational effort, the semianalytical method is evaluated at a fixed number of turns $n = 10$. The intertape spacing is varied by changing the outer coil radius.

exceeds the loss of a single straight tape by more than a factor of 100. Plenty of such coils have been presented in literature [25, 94, 125, 161–163], and the large AC loss is always considered as a show stopper for an application at significant AC frequencies. Here, we see, however, that Q_{hyst} decreases strongly with increasing d. For $d > w$, Q_{hyst} even converges towards the single tape limit (Norris equation). Our analysis shows that a surprisingly small intertape spacing is sufficient to bring the AC loss of single pancake coils to an acceptable level. At $d = w/2$, the remaining loss exceeds the single tape limit only by a factor of 10, and at $d = w$, only by a factor of 3.

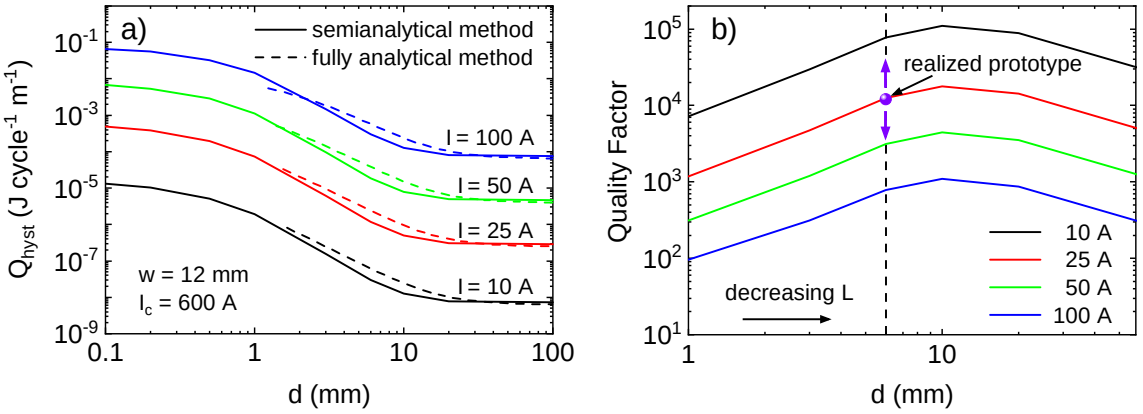

Figure 6.4: (a) Calculated hysteresis loss of the complete winding as a function of d. The loss per cycle and unit tape length is shown for different values of I_{rms}. The semianalytical [solid lines, Eq. (6.6)] and the fully analytical methods [dashed lines, Eq. (6.7)] are compared to each other and show good agreement. (b) Calculated Q-factors of different design variations as a function of d. The values have been obtained by evaluating Eq. (6.10) at different values of I_{rms}. All parameter interdependencies between d, L, n and l_{tot} have been considered. The black arrow indicates that L decreases with increasing d. The realized prototype at $d = 6\,\mathrm{mm}$ is indicated as a purple dot. Subfigure (a) is reprinted from [164].

In order to be able to choose the best intertape spacing, we evaluate in the next step the Q-factor of the coil as a function of d. According to Eq. (2.8), the Q-factor can be expressed as

$$\text{Q-factor} = 2\pi \times \frac{\text{stored energy}}{\text{energy loss per cycle}} = 2\pi \frac{L I_{\mathrm{rms}}^2}{Q_{\mathrm{hyst}} l_{\mathrm{tot}}} \tag{6.10}$$

We have calculated the Q-factors of all reasonable winding configurations, with turn numbers between $n = 1$ and $n = 58$, and show the result* in Fig. 6.4 (b). As expected, the Q-factor increases with increasing d. As soon as Q_{hyst} approaches the single tape limit, the Q-factor reaches a plateau and starts to decrease again. Furthermore, we observe that the Q-factor depends on the current amplitude and scales with $1/I_{\mathrm{tr}}^2$. This is caused by the fact that $Q_{\mathrm{hyst}} \propto I_{\mathrm{tr}}^4$. At low current amplitudes, the Q-factors can therefore reach values as high as 100 000. This justifies our holistic design approach of operating the WPT system at high voltages and low currents. According to Fig. 6.4, the optimum number of turns to maximize the Q-factor in the limited

* All parameter interdependencies of the coil design have been considered: $L \propto n^2$, $l_{\mathrm{tot}} \propto n$ and $n \propto 1/d$.

winding space is $n = 5$ ($d = 12\,\mathrm{mm}$). Due to the fact that this winding would have a very low inductance of only $L \approx 5\,\mu\mathrm{H}$, the corresponding operating frequency in our WPT system would be $f \approx 400\,\mathrm{kHz}$ [compare Eq. (2.14)]. At such a high frequency, eddy current losses would certainly reduce the performance of the coil. A lower frequency can only be achieved, if we accept a reduced Q-factor.

It is evident that the choice of the best coil design is unfortunately not straight forward. We found a difficult trade-off between two risk cases. If d is chosen too small, the hysteresis loss in the HTS layer could result in self-heating of the winding and in a breakdown of superconductivity during operation. If d is chosen too large, the power density is reduced and we run the risk of significant eddy current losses at the required operating frequency.
Based on these considerations we decided to realize two different coil designs (called 1st Gen. and 2nd Gen.). All coil parameters are summarized in Tab. 6.1. The 1st Gen. coil design has 10 turns and an intertape spacing of $d = 6\,\mathrm{mm}$. The inductance is $L = 20.5\,\mu\mathrm{H}$ and the required operating frequency will be $f = 100\,\mathrm{kHz}$. If the superconducting hysteresis loss alone is considered, the Q-factor at the expected peak current of $I_{\mathrm{rms}} = 36\,\mathrm{A}$ is $Q \approx 3000$. The corresponding power loss per unit length is $P/l \approx 1\,\mathrm{W/m}$ and the total power loss per coil is $P \approx 5.4\,\mathrm{W}$.
The 2nd Gen. coil design has a larger inductance and will allow us to perform experiments at lower frequencies. In order to avoid the risk of a coil quench, we decided to reduce the power density. We increase the winding space by extending the outer coil radius to $r_{\mathrm{out}} = 23\,\mathrm{cm}$. This allows us to fit 30 turns into the winding space, while keeping the same intertape spacing of $d = 6\,\mathrm{mm}$. The inductance of the resulting winding is $L = 230\,\mu\mathrm{H}$ and the required operating frequency will be $f \approx 9\,\mathrm{kHz}$. The Q-factor at the expected peak current of $I_{\mathrm{rms}} = 36\,\mathrm{A}$ is $Q \approx 7000$. The corresponding power loss per unit length is $P/l \approx 0.1\,\mathrm{W/m}$ and the total power loss per coil is $P \approx 2.7\,\mathrm{W}$.
The key figures of merit of the 2nd Gen. coil outperform the ones of the 1st Gen. coil. This is the case, because obviously the 2nd Gen. coil will not achieve the initial target power density of $3\,\mathrm{kW/dm^2}$. Nevertheless, we expect that these coil designs will allow us to demonstrate the performance of the WPT system in a broad frequency range.

Parameter	1st Gen.	2nd Gen.
r_{in}	5 cm	5 cm
r_{out}	11 cm	23 cm
n	10.5	30.5
d	6 mm	6 mm
l_{tot}	5.4 m	27.4 m
L (air coil)	20.5 µH	230 µH
L (with magn. core at 77 K)	24.4 µH	–
f	100 kHz	9 kHz
Q-factor (at $P_{\mathrm{out}} = 11\,\mathrm{kW}$)	3000	7000
power density (at $P_{\mathrm{out}} = 11\,\mathrm{kW}$)	$3\,\mathrm{kW/dm^2}$	$0.66\,\mathrm{kW/dm^2}$

Table 6.1: Design parameters of the selected coil geometries.

The remaining question is, which HTS tapes should be used for the coil prototypes to avoid eddy current losses. Based on our findings from Sec. 4.2.2, we can state that an HTS tape with copper stabilizer should not be used. Even if the stabilizer is as thin as 20 µm, $f \gg f_{\mathrm{tr,Cu}}$ would be satisfied at the desired operating frequencies and the eddy current loss would dominate the total loss of the winding. In a non-stabilized tape on the other hand, the frequency dependence is dominated by the thin silver layer. For the 1st Gen. coil, we see that the working frequency is dangerously close to the transition frequency of the silver layer ($f = 100\,\mathrm{kHz} \approx f_{\mathrm{tr,Ag}}$). In this regime, the exact behavior of the eddy current loss is not fully understood, yet. In particular, we have to consider the fact that the shielding effect of the superconducting layer breaks down, and that eddy current losses start to appear. For the 2nd Gen. coil the working frequency is significantly below $f_{\mathrm{tr,Ag}}$, and eddy current losses will not appear.
Due to the large resistivity of the hastelloy substrate, $f \ll f_{\mathrm{tr,hastelloy}}$ is given for all cases, and eddy current losses in the substrate can be neglected.
In order to verify our assumptions, we will build coil prototypes with both, stabilized- and non-stabilized tapes (as defined in Tab. 6.2), and we will compare their performance in Chap. 8.

Parameter	Tape A (non-stabilized)	Tape B (stabilized)*
Manufacturer	Theva	Theva
Product name	TPL 1100	TPL 4121
w	12 mm	12 mm
$t_{\mathrm{hastelloy}}$	100 µm	50 µm
t_{HTS}	3 µm	3 µm
t_{Ag} (per side)	≈ 1.5 µm	≈ 1.5 µm
t_{Cu} (per side)	–	10 µm
I_{c} (77 K, in self-field)	600 A	600 A

Table 6.2: Properties of the selected HTS tapes that have been used to build coil prototypes. The comparison between Tape A (non-stabilized) and Tape B (stabilized) is expected to reveal the influence of eddy current losses at high frequencies.

In order to obtain a quantitative reference value that can later be compared to experimental results, we have used our numerical simulation model to estimate the total eddy current loss of the complete winding (1st Gen.) for tape A and tape B. The different tape configurations have been modeled as m-s-strips, as introduced in Sec. 4.2.2. We present the result in Fig. 6.5, and we remind the reader that the result is only valid in the high-frequency regime. In this regime, any effects related to superconductivity are insignificant and the tape behaves identical to a simple metallic strip. The curves in Fig. 6.5 are solid/dashed, where the high-frequency approximation is valid/invalid.
The result in Fig. 6.5 shows that the loss in the copper stabilizer at 100 kHz would exceed the superconducting hysteresis loss by a factor of 10.

* For better comparability between stabilized and non-stabilized tapes, an identical substrate thickness of $t_{\mathrm{hastelloy}} = 100$ µm would have been prefered in both tapes. At the moment of coil fabrication, unfortunately, stabilized tapes have only been available with $t_{\mathrm{hastelloy}} = 50$ µm. Nevertheless, the applied frequencies are low enough, so that eddy current losses in the substrate can be neglected. Therefore, we assume that the comparison between the tapes will be valid.

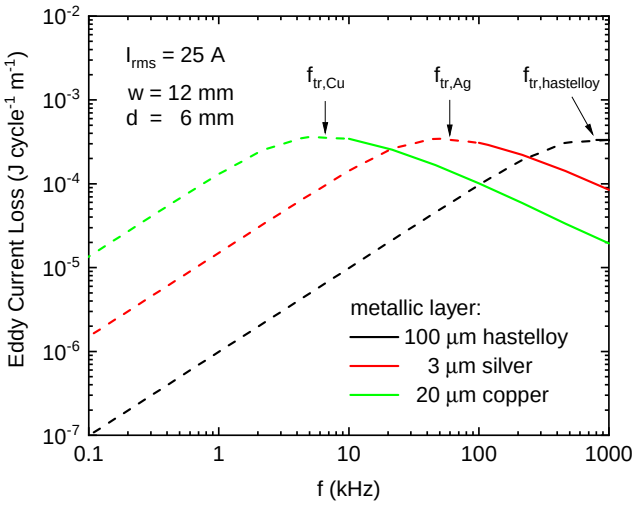

Figure 6.5: Simulated eddy current loss of an HTS winding with $n = 10$, $w = 12\,\mathrm{mm}$ and $d = w/2$ at a transport current of $I_{\mathrm{rms}} = 25\,\mathrm{A}$ as a function of the frequency. The results of three typical metal layers are compared to each other. The individual transition frequencies of all layers are marked by the arrows. The transport current density in the HTS layer is assumed to be uniform and superconducting shielding currents are not considered. The result is therefore only valid in the high-frequency regime ($f \gg f_{\mathrm{tr}}$). The material specific resistivities, which have been used to model the behavior of the metal strips at 77 K, have been listed in Tab. 4.2. The lines are solid/dashed, where the high-frequency approximation is valid/invalid.

For the case that the shielding effect in the non-stabilized tape is also lost at 100 kHz, Fig. 6.5 suggests that the eddy current loss in the silver layer could even be larger than the loss of the copper stabilizer.

6.3 Alternative Calculation Methods

We conclude this chapter by mentioning that our approach of combining numerical and analytical methods to calculate the AC loss in HTS coils, differs from the fully numerical methods, which are applied in most of the recent literature publications. We discuss, in the following, shortly the basics of those methods and we show under which circumstances they become necessary.
The typical approach of fully numerical methods is to calculate the exact, non-uniform current distribution in the HTS tapes, considering the highly non-linear dependency of the conductivity on electric and magnetic fields. The $E(J)$ power law of type II superconductors (Eq. (3.7)) is implemented into the field formulation of FEM programs and the local power dissipation is determined numerically from the electromagnetic field quantities $P_{\mathrm{loss}} = J \cdot E$ [124, 137, 160, 165]. With this method, the superconducting hysteresis loss can be solved in all turns simultaneously and shielding effects between the turns or between different coils can be considered. Furthermore, the field dependence $J_{\mathrm{c}}(B)$ and the spatial dependence $J_{\mathrm{c}}(x)$ of the critical current density can be implemented [86].
Fully numerical methods have been applied in literature to solve the AC loss in single pancake coils [94, 123, 166, 167], double pancake coils [124, 168] and even in stacks of pancake coils

[169, 170]. For the case of tightly wound windings with a large number of turns, the approach of homogenization is often used [171–173] to reduce computational time. In this approach all the turns of the winding are considered as a single solid bulk superconductor.
Most of the available simulation results have been validated by experiments and the methods are widely accepted as state of the art. Nevertheless, compared to the simplified simulations based on uniform current density, the exact calculation of the current distribution requires significantly enhanced efforts, regarding modeling and computation time. These extra efforts are only required if,

- the magnetic field generated by the complete coil is strong enough to reduce the critical current of individual turns. In this case, the critical currents of all turns must be determined self consistently for each value of applied current [94, 162, 174]. The critical current and hence also the AC loss of the complete coil, is then dominated by the weakest turn.
- the intertape spacing is small, or stacks of coils are considered, so that shielding effects between the individual turns [175, 176] or coils [86] become important.

The WPT coils considered in this thesis don't fulfill either of the conditions.
Firstly, the number of turns is small, the current amplitudes are far below I_c and the resulting magnetic field strengths inside the winding are in the order of only a few mT. Our analysis in Fig. 3.3 shows that the critical current of Theva tapes is not reduced up to field strengths of several 100 mT. Therefore, the critical current in the proposed coil design is identical to the critical current of a single tape in its self-field.
Secondly, the intertape spacing between the turns in the winding, and the distance between transmitter and receiver coils is big enough so that shielding effects between the tapes or coils are unimportant.

In order to verify that our simplified approach gives accurate results, we have applied both simulation methods (uniform and non-uniform current density) to a stack of 20 HTS tapes at two different values of intertape spacing. We were able to show that the assumption of a uniform current density reproduces the magnetic field distribution of the complete stack perfectly, if the intertape spacing is large enough. The results are presented in detail in Appendix A.4.

Chapter 7

Coil Fabrication

Although the fabrication of superconducting coils is generally well established in the industry, we encountered surprisingly many engineering challenges during the preparation of our WPT prototypes. The 1st Gen. coil was realized in a simple 3D printed coil former. For the 2nd Gen. coil, we developed a molding technique, which allowed us to embed the distributed winding into a Stycast resin. The established technique has proven to provide sufficient stability during thermal cycling and could be a promising candidate for a commercial solution. In the following, we present our fabrication procedure in detail.

7.1 Winding Technique

The superconducting winding of the coil prototypes is built with a simple, but effective method. A circular wooden centerpiece of radius $r = 5\,\mathrm{cm}$ is mounted onto a rotating plate. The HTS tape and the spacer material are both wound simultaneously around the centerpiece by slowly turning the plate as shown in Fig. 7.1.

Figure 7.1: Home built setup for the fabrication of the HTS winding. The HTS tape and the spacer material are both wound simultaneously around the centerpiece by slowly turning the rotating plate.

The applied spacer material is a commercially available ethylene-propylene-diene-monomer (EPDM) rubber band with a closed cell structure. One side of the rubber band is equipped with an adhesive tape. The width of the rubber band is chosen 3 mm wider than the width of the HTS tape. Due to the small overlap, the rubber band not only sticks to the HTS tape, but also the individual turns stick to each other. After completing all the turns, the centerpiece

is removed and the winding is reinforced with Kapton tape. The EPDM rubber band showed very good properties during thermal cycling. Due to the fact that the rubber band, and hence also the complete winding, is soft and flexible, all internal tensions are leveled out during the cool down and we did not observe any deformations. We show pictures of the fabricated HTS windings with (a) 10 turns and (b) 30 turns in Fig. 7.2.

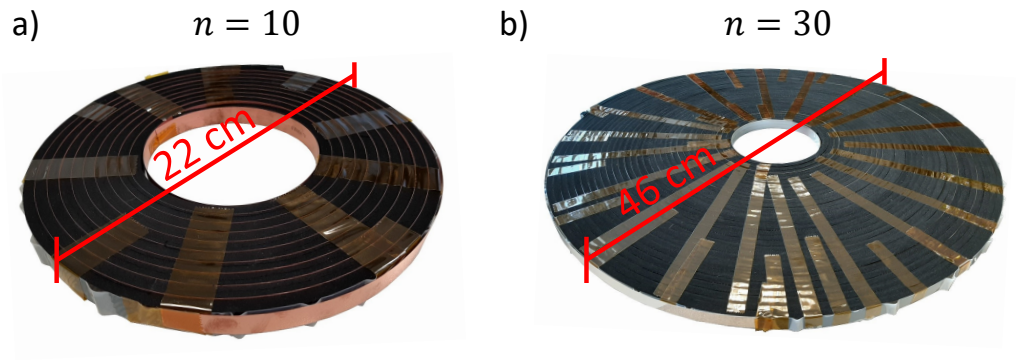

Figure 7.2: Photographs of the fabricated HTS windings with (a) 10 turns and (b) 30 turns.

7.2 First Generation HTS Coils in 3D Printed Coil Former

For the 1st Gen. coil design, we have developed a 3D printed coil former, which holds the winding, the current leads, and the ferrite core. The current leads are positioned at the edge of the coil to avoid eddy current losses in the copper contacts. The copper contacts consist, each, of two solid copper blocks with an area* of $30 \times 30\,\mathrm{mm}^2$ and a total thickness of 20 mm. The HTS tape is sandwiched between the contact surfaces, and pressure is applied with four screws. The ferrite segments are embedded into small recesses in the bottom of the coil former. As HTS tapes do not allow to be bent or twisted on short length scales, the contacting of the innermost turn is challenging. In our design, the innermost turn is lowered, exits the coil former through a slit and is guided towards the copper contact below the coil former. In order to make enough room for a smooth transition from the inside to the outside, we had to remove four ferrite segments from the magnetic core. The coil former can be closed with a lid. The lid fixes the HTS winding inside the coil former, so that the coil can be turned upside down. The coil former has four fixtures, which can be used to mount the receiver coil on top of the transmitter coil. We used threaded rods, made of plastic, to control the distance between the transmitter and the receiver. We show, in Fig. 7.3 (a), a CAD drawing of the complete coil, with the winding being mounted into the 3D printed coil former, and in Fig. 7.3 (b) a photograph of a fabricated coil pair, as it was used in the experiments in Chap. 8.
In order to highlight the development process of this coil design, we show in Fig. 7.4 the evolution from the first winding tests to the final prototype.

* We note that the volume of the copper contacts is not optimized and could be further reduced in future work.

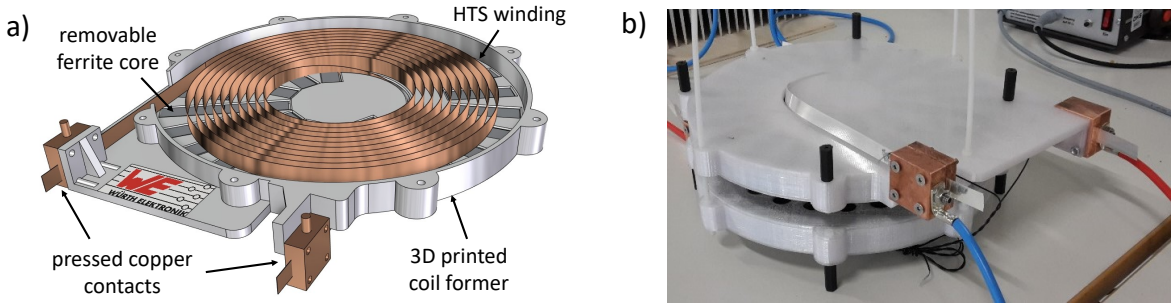

Figure 7.3: Overview of the 1st Gen. superconducting WPT coil design in a 3D printed coil former. In (a), we show a CAD drawing of the complete coil, including the HTS winding (spacer material not shown), the removable ferrite core, and the pressed copper contacts. In (b), we show a photograph of an inductively coupled coil pair. The receiver coil is mounted face down on top of the transmitter coil. The receiver and the transmitter are spaced by an air gap of a few centimeters.

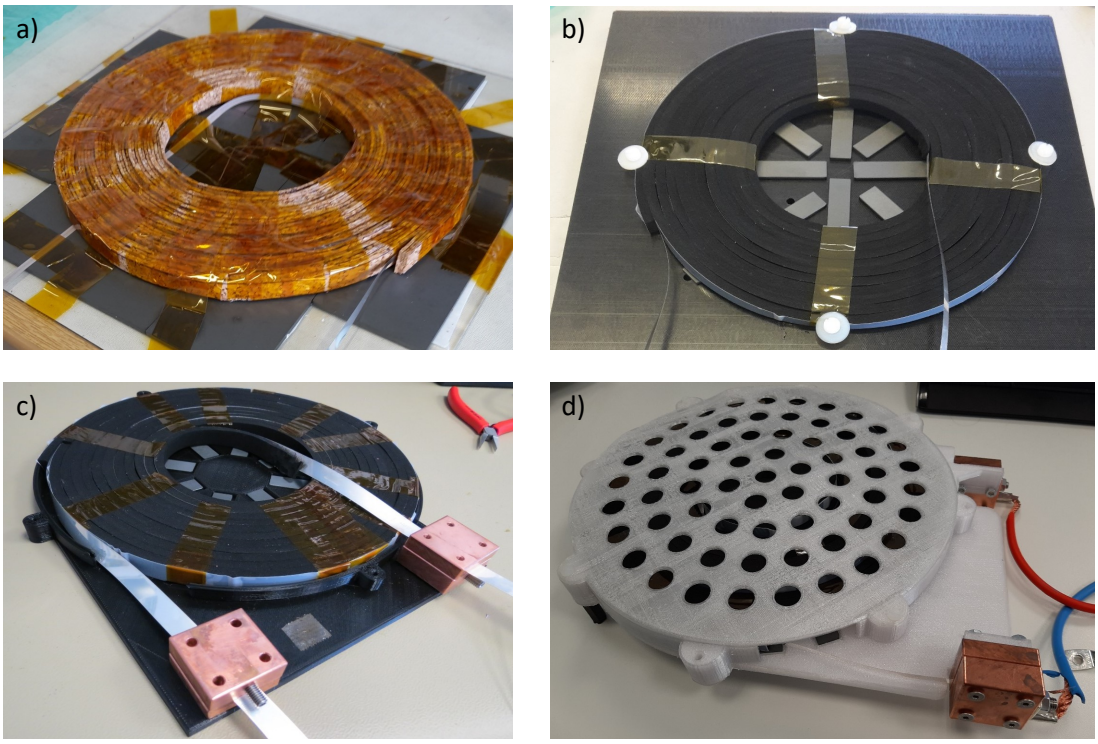

Figure 7.4: Evolution of the coil design. From the first winding tests to the final prototype, we had to overcome plenty of engineering challenges: (a) finding a suitable spacer material, (b) finding a solution to fix the winding, the core and the copper contacts, and (c) avoiding the twist of the HTS tape in the current leads, which results in a damage of the tape and in a strong reduction of I_c. (d) shows the final prototype, which has successfully transfered power levels of 6 kW. The diameter of the prototypes is 22 cm.

7.3 Second Generation HTS Coils with Molding Technique

With the aim of further improving the mechanical stability of the coil, we have realized the 2nd Gen. coil design with a molding technique. Instead of using a coil former to assemble the winding and the copper contacts, we have embedded the components into a potting compound. A professional molding process typically involves the development of a special molding form and the application of vacuum technique to avoid air bubbles. As such topics would go far beyond the scope of this thesis, we demonstrate here a simplified process, based on a silicone form without vacuum technique.
The challenges, of using epoxy resins to impregnate the windings of HTS coils are well known in literature. In order to avoid mechanical stress during thermal cycling, which could lead to a delamination of the HTS layer, the thermal expansion coefficients of the potting compound must be matched very carefully to the properties of the HTS tape. For the case of tightly wound pancake coils, the commercially available Stycast FT2850 resin has proven to be suitable. Its thermal expansion is nearly identical to the one of HTS tapes [177], and in most* literature publications, the critical current of the impregnated coils is only slightly reduced [178–181]. The Stycast resin can be used with different hardeners. In order to achieve the lowest viscosity, we have applied exclusively the Cat 24LV hardener, with the mixing ratio as suggested by the manufacturer.
In our coil design, we face however the challenge that the winding does not have a rigid support structure. Any internal tensions that might appear in the potting compound will act directly onto the winding. Furthermore, the compatibility between the Stycast resin and the EPDM rubber band is unknown. In order to investigate the applicability of the Stycast resin to our coil windings, we have performed the following pretests.

7.3.1 Experimental Investigation of the Applicability of the Stycast Resin

First, we have applied our molding technique to a short sample of straight Theva tape, in order to check if the general compatibility between Theva tapes and Stycast resin is indeed given as expected. The current feeds are realized by solid copper blocks, identical as it would be the case in the actual coil. The environment around the tape is reinforced with fiberglass. The voltage taps, to determine the critical current with the four-point measurement, are soldered directly onto the tape. The length of the complete sample is 27 cm and the distance between the voltage taps is 12 cm. The sample is shown in Fig. 7.5 (a). After cooling the sample slowly down to 77 K, we observed that the critical current was reduced from its initial value $I_c = 600$ A (tapestar measurement) by 36 % to $I_c = 382$ A. We cycled the temperature 5 times between 300 K and 77 K and we observed that the critical current did not degrade further. The mechanism of degradation might be of chemical or of mechanical nature. Considering that the AC currents in our WPT coils remain always far below the critical current, the slightly reduced current carrying capacity is however not a show stopper.

* In Ref. [177], Bart et al. have found a chemical incompatibility between the Stycast FT2850 resin and the superconducting REBCO layer. If the REBCO layer is exposed to the resin, i.e. if the tape is cut open on the sides, or if the protective silver coating is damaged, the critical current of the tape degrades completely. As we use only tapes, which are completely covered by the silver coating, we expect no degradation.

Second, we have applied our molding technique to a small coil winding with 10 turns. The individual turns are spaced by the EPDM rubber band and the winding is only reinforced by a thin layer of fiberglass. The voltage taps are soldered onto the ends of the winding, so that the voltage drop along the complete tape length of 5.4 m is measured by the four-point method. According to the tapestar measurement data, the critical current of the winding is $I_c = 425$ A. Due to the fact that this was the first potting test of a distributed winding, we did not expect the test to be successful and used for the current feed only thin copper strips, instead of the expensive solid copper contacts. Surprisingly, the distributed winding was compatible with the Stycast resin and we encountered no problems during the potting process or during the cooldown. The prepared sample, including the current feeds and the voltage taps is shown in Fig. 7.5 (b). We cycled the temperature 5 times between 300 K and 77 K. After the last cycle, we increased the DC current until we observed at $I = 330$ A a quench due to the temperature increase in the thin (normal conducting) current feed. The quench happened behind the voltage tap and was not detected by the I_c-measurement.
We conclude that the critical current in the coil is larger than 330 A, which corresponds, to a degradation of less than 22 %. Most importantly, we did not observe any cracks or deformations, even after multiple thermal cycles. We were very satisfied with this result and proceeded directly to the next step.

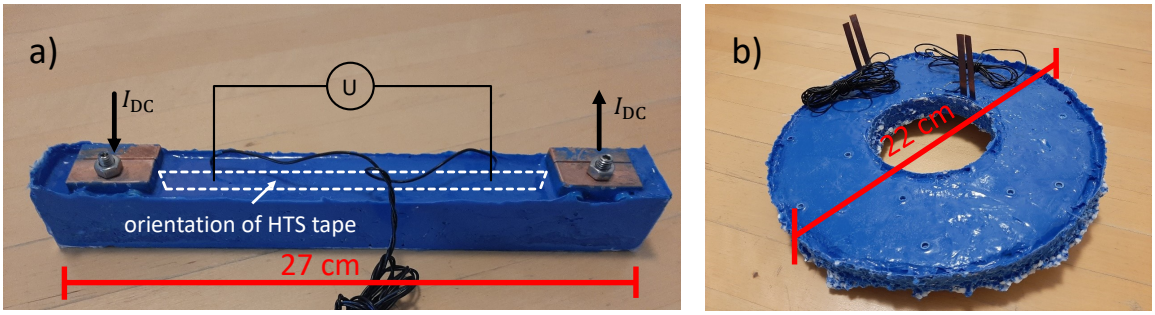

Figure 7.5: Fabricated samples to study the applicability of the Stycast resin. In (a), we have potted a straight tape with a length of 27 cm, which is contacted by two copper blocks. Voltage taps are soldered directly onto the tape. In (b), we have potted an HTS coil winding as depicted in Fig. 7.2 (a). The individual turns are spaced by an EPDM rubber band and the winding does not contain any rigid support structure.

7.3.2 Fabrication of the HTS Coils

After having completed the successful pretests, we have applied the molding technique to the final 2nd Gen. coil design. Therefore, we firstly had to manufacture a suitable silicone form. We applied a conventional impression technique, where a true scale model of the coil design is used to create a negative imprint in liquid silicone. After curing, the silicone form can be used (multiple times) to embed the final product into the potting compound.
In order to be able to prepare such a silicone form, we had to fabricate a true scale coil model,

which defines the inner shape of the form, and we had to fabricate a suitable tub, where the liquid silicone can be poured into, and which defines the outer shape of the silicone form [see Fig. 7.6 (a)]. The silicone form should provide sufficient stability, but the weight must remain reasonably low. We decided to design the tub in such a way that the silicone form has a minimum wall thickness of 2 cm. The tub and the true scale coil model consist each of several wooden pieces, which have been shaped in a milling machine and have been assembled in our lab. With this simple process, we have obtained a high quality silicone form.
We show the fabrication of the silicone form schematically in Fig. 7.6. In (a), we show the shapes of the tub and of the true scale coil model in detail. In (b), we show the final silicone form after curing it at room temperature for 6 hours. The applied silicone is a low-viscosity and fast curing compound (Mold Max 29NV/2), which can be used without vacuum technique. The required mass of liquid silicone was approximately 10 kg.

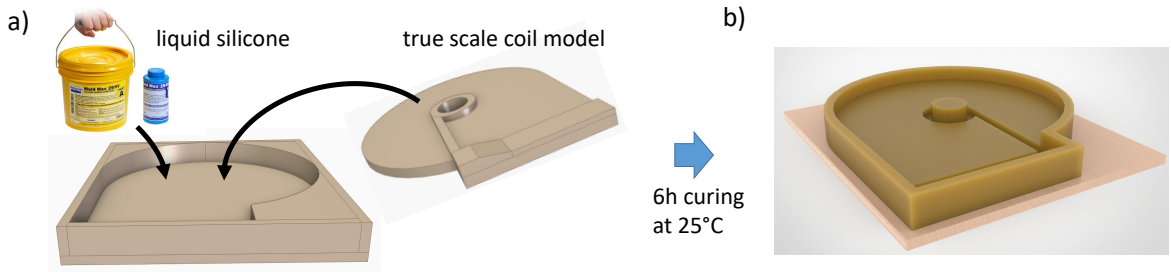

Figure 7.6: Preparation of the silicone form, which was used to mold the 2nd Gen. WPT coils. (a) Schematic overview of the fabrication process. We used a wooden true scale model of our coil design to create an imprint in a low-viscosity silicone rubber. The tub, where the liquid silicone was poured into, has been designed in such a way that the silicone form has a minimum wall thickness of 2 cm. (b) Picture of the final silicone form after curing. The total mass is approximately 10 kg.

After having prepared the silicone form, we used it to fabricate our 2nd Gen. WPT coils. The chosen type of silicone has proven to be compatible with the Stycast resin. The properties of the form did not deteriorate after several molding processes and it can still be used to fabricate further prototypes.
The molding process of each prototype is performed in three steps.
First, the silicone form is partly filled with Stycast resin. Second, the HTS winding is placed into the silicone form. Last, the remaining Stycast resin is poured over the winding until the form is completely filled. The total amount of required Stycast per coil is 5.4 kg.
In order to be able to transfer the flexible winding, including the copper contacts, safely into the silicone form, we prepared a wooden transfer plate as shown in Fig. 7.7 (a). We have used thin cotton cords to attach the winding to the transfer plate. During the transfer, the plate is turned upside down to place the winding into the silicone form. The winding must be positioned very accurately, so that the current lead, which runs below the coil, slips into the small channel (compare bottom view of the coil). Once the transfer is complete, the cords can be cut and the transfer plate can be removed. We show a photograph of the uncured coil in the silicone form in Fig. 7.7 (b).
After curing the Stycast resin for 12 hours at room temperature, the coil can be easily removed

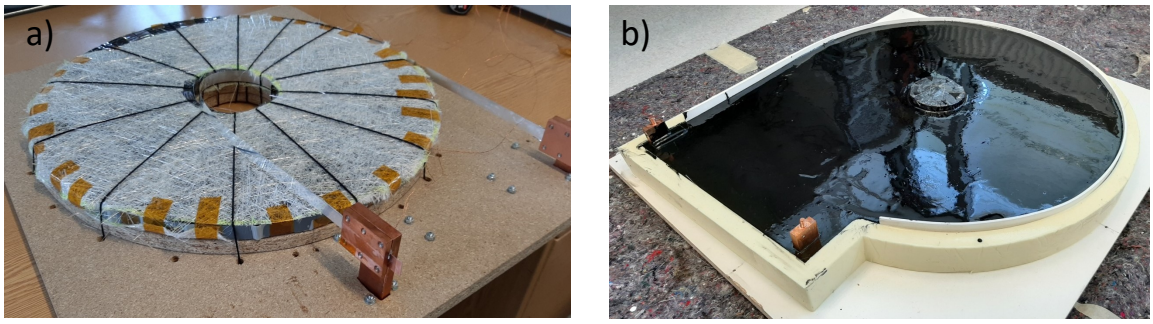

Figure 7.7: Production steps of the 2nd Gen. WPT coil. (a) The winding and the copper contacts are fixed on a wooden plate, which allows to transfer the coil safely into the silicone form for the molding process. (b) The coil is molded with Stycast FT 2850, as described in the main text.

from the flexible silicone form. The top and the bottom views of the final coil are shown in Fig. 7.8 (a) and (b).

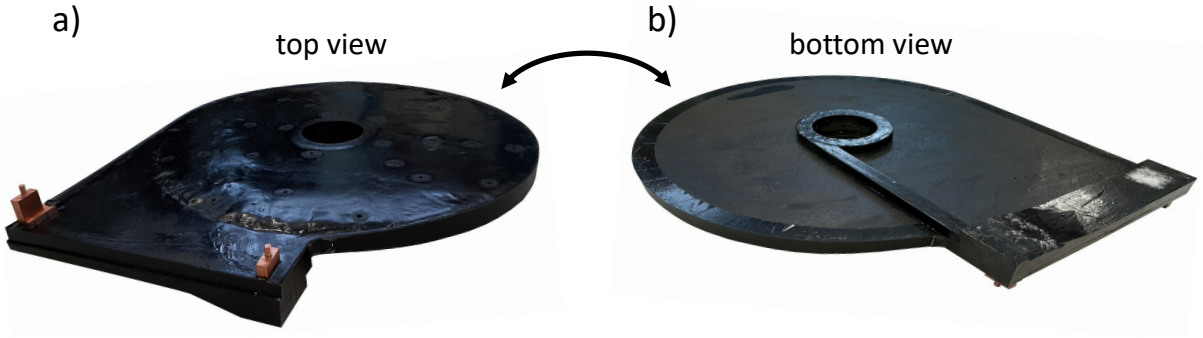

Figure 7.8: Photographs of the fabricated 2nd Gen. WPT coil. The (a) top and (b) bottom view are shown next to each other. The coil is completely sealed and has proven to provide sufficient stability during thermal cycles. The innermost turn is guided to the current feed in a thin channel. The diameter of the coil is 50 cm.

7.4 Sample Overview

We conclude this chapter by providing an overview of all fabricated coil samples in Tab. 7.1. The entries are sorted according to the coil design (1st Gen./2nd Gen.) and each sample is identified by a unique sample number. Further, we specify the applied tape type and we give additional information about the intended experimental purpose, for each sample.

1st Gen. coil design

sample number	tape type	comment
#1.1	Tape A	Low-frequency AC loss, I_c–measurement
#1.2	Tape B	Low-frequency AC loss, WPT experiments
#1.3	Tape A	WPT experiments
#1.4	Tape A	
#1.5	Tape B	WPT experiments (with #1.2)

2nd Gen. coil design

sample number	tape type	comment
#2.1	Tape A	I_c–measurement
#2.2	Tape A	WPT experiments
#2.3	Tape A	
#2.4	Tape A	repetition of WPT experiments
#2.5	Tape A	

Table 7.1: List of all fabricated coil prototypes. The samples are sorted according to the coil design (1st Gen./ 2nd Gen.). For future reference, each sample is identified by a unique sample number, the applied tape type is defined and the intended experimental purpose is mentioned in the comment.

Chapter 8

Experimental Verification

In this chapter, we present the experimental results of this thesis. In Sec. 8.1, we characterize two of our fabricated coils under DC conditions, to verify that the fabrication process produces functional prototypes. In Sec. 8.2, we perform low-frequency AC loss measurements. First, we measure the AC loss in short samples of Theva tape, to verify that these tapes generally behave as expected. Second, we measure the AC loss in the fabricated 1st Gen. coils to verify that our calculations from Chap. 6 are correct. In Sec. 8.3, we apply the fabricated coils to our fully functional WPT system and we perform several high-power experiments. First, we perform a pre-characterization, where we determine the optimum working points of different system configurations. Second, we apply the 1st Gen. coils to operate the WPT system in the high-frequency regime. We measure the DC-to-DC efficiency at different frequencies and we use the results to extract the high-frequency AC loss of the transmission coils. Last, we apply the 2nd Gen. coils to operate the WPT system in the low-frequency regime. We measure the DC-to-DC efficiency, and we observe an unexpected quench behavior. We analyze the results in detail and we provide a comprehensive conclusion.
Several parts of the presented results have already been published in [164]. Where appropriate, we have added the reference in the text.

8.1 DC Characterization

Considering the fragility of the HTS tapes and the various challenges of the coil fabrication (compare Chap. 7), it is clear that some of the fabricated coils could have local defects. At the position of such a damage, the superconducting layer could be broken or could at least suffer from a reduced value of I_c. It is therefore necessary to test the fabricated coils first under DC conditions. During the DC characterization, we faced however the challenge that the local defects are not easy to detect. As long as $I < I_c$, they are completely invisible, i.e., perfectly superconducting with zero voltage drop. In the moment when $I = I_c$, the power dissipation at the position of the defect increases very quickly. So in order to protect the coil during the quench from irreversible damage, the quench-detection mechanisms of the measurement system must switch off the current supply fast enough. This is only possible, if the voltage taps are

soldered directly onto the HTS tape*, and if the threshold voltage is low enough†. But even then, the measurement of I_c comes along with a significant risk of damaging the sample. We had to consider for each sample individually, if it is required to know the exact value of I_c.
On the one hand, it is not required, because our WPT system is designed to be operated at low current amplitudes ($I_{rms} < 36\,A$). The applied HTS tapes have large critical currents of $I_c = 600\,A$, and small defects are therefore not necessarily a problem. Even if the critical current at the defect is reduced to 10 % of its initial value, the tape can still carry DC currents of 60 A. On the other hand, such a defect results in a local increase of the AC loss. As the AC loss scales with $(I/I_c)^4$, the heat load at the defect is much larger then in the rest of the coil, which could cause a local hotspot. If the hotspot expands into undamaged regions, the small defect can trigger a quench of the complete coil.

In most cases, we decided that it is sufficient to test the coils at low current amplitudes. Only in two samples (#1.1 and #2.1), we tried to measure the exact value of I_c‡. The results of both samples are shown in Fig. 8.1.
We observe that both coils are perfectly superconducting up to large current amplitudes and are therefore suitable for WPT experiments. We are however not able to determine the exact value of I_c. At current amplitudes of 400 A (sample #1.1) and 200 A (sample #2.1), the coils quenched due to a temperature increase in the (normal conducting) current feed§. The quench happened directly behind the current feed and was therefore not protected by the quench-detection. Both coils took irreversible damage during the measurement. A picture of the relevant tape segment with the burned area of sample #1.1, is shown in the inset of Fig. 8.1. Nevertheless, we have obtained an important result with these measurements. The developed fabrication process of both coil generations produces functional prototypes. The critical current of the 2nd Gen. coil (50 cm diameter, 30 turns, 6 mm intertape spacing, molded with Stycast resin) is $I_c > 200\,A$. The exact value of I_c, is not relevant for the application in our WPT system. For scientific purpose, it could be studied in more detail in future work. Additionally, we have learned that the copper contacts are not able to feed currents beyond 400 A into the coil.

* While the soldering of voltage taps is typically not a problem for stabilized tapes, it becomes difficult for non-stabilized ones. The thin silver layer, of these tapes, melts and dissolves in the soldering tin. So there is a large risk that the soldering process itself damages the protective silver layer and reduces I_c at the position of the voltage tap. Due to the possible incompatibility between the HTS layer and the Stycast resin [177], a damaged silver layer in the 2nd Gen. coils could result in a complete degradation of I_c. The samples #2.2, #2.3, #2.4 and #2.5 have therefore been fabricated without soldering voltage taps onto the surface of the HTS tape.

† Any change of transport current in the coil requires a finite voltage. So in order to avoid that the quench-detection is triggered at each current step, we had to set the threshold voltage higher than the typical value of 1 µV/cm. The high threshold voltage increases however the risk of a coil damage during the quench

‡ The DC measurement of sample #1.1 was performed after having finished all the AC loss measurements (compare Sec. 8.2)

§ The quench of sample #2.1 at 200 A can be explained by the fact that the current feeds have not been sufficiently cooled during this experiment. Without noticing it, the fill level of the liquid nitrogen bath has dropped below the required level. We show the result anyway, because it demonstrates that the developed molding technique produces functional prototypes. The critical current of the large scale HTS winding, embedded into Stycast resin, is beyond 200 A.

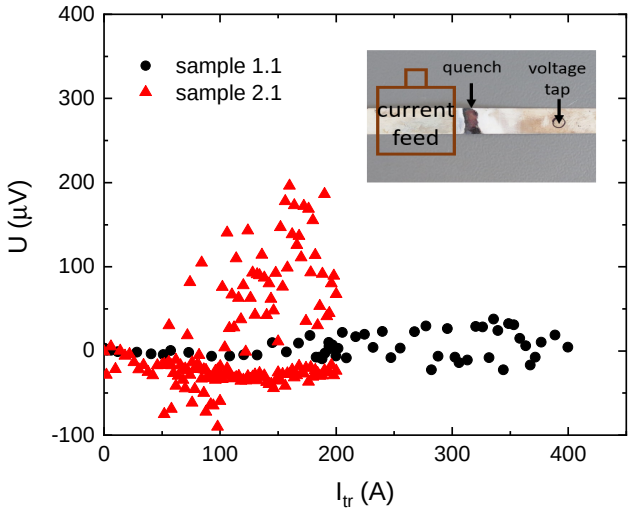

Figure 8.1: Measurement of the critical current in a 1st Gen. coil (sample #1.1) and in a 2nd Gen. coil (sample #2.1). Both coils are perfectly superconducting up to large current amplitudes and are therefore suitable for WPT experiments. Nevertheless, both coils quenched significantly below the expected value of I_c. The quench happened directly behind the (normal conducting) current feed and was therefore not protected by the quench-detection. Both coils took irreversible damage during the measurement. A picture of the relevant tape segment with the burned area of sample #1.1, is shown in the inset.

8.2 Low-Frequency AC Loss Measurements

In order to verify our AC loss calculations, we have performed several low-frequency measurements. First, we have verified that the AC loss behavior of the HTS tapes, manufactured by Theva Dünnschichttechnik, agrees with the analytical equations from Chap. 4. This verification is particularly interesting, because the crystal structure of the Theva tapes differs from other manufacturers. They have the unique feature that the *ab* planes of the crystal lattice are tilted by 30° with respect to the surface of the tape. To the best of our knowledge, no measurements of the AC loss in Theva tapes have been presented in literature yet. Second, we have verified that the AC loss behavior of the fabricated WPT coils agrees with the calculations from Chap. 6. Therefore, we have measured the AC loss in a single coil (standalone). It should be mentioned that in contrast to this exact result, the measurement with the WPT system is less precise, because it always contains the loss of two coils as well as the parasitic losses of the room temperature electronics.
In the following, we introduce the experimental method and we discuss the measurement results.

8.2.1 Experimental Method

The AC loss measurements have been performed with a standard lock-in technique [125, 182] at the Institute of Electrical Engineering in Bratislava. The experimental setup, which is supervised by the group of F. Gömöry, can be used for the measurement of short HTS tapes and complete HTS coils. We show the schematic overview of the experimental setup in both measurement modes in Fig. 8.2 (a) and (b), respectively.

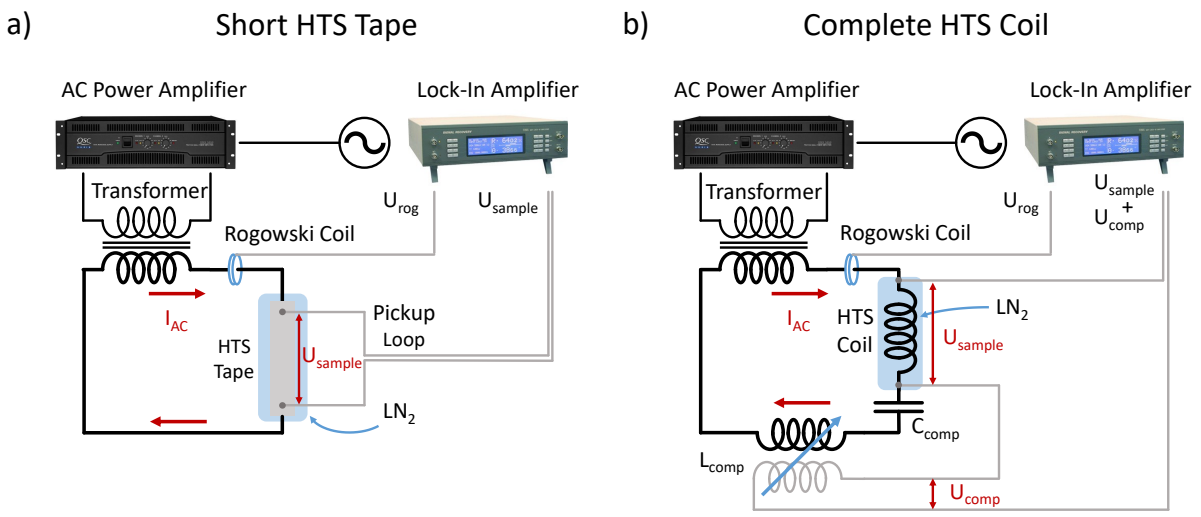

Figure 8.2: Standard lock-in technique for the experimental measurement of the AC loss in (a) short samples of HTS tape and (b) HTS coils. An AC current of frequency f and amplitude I_{AC} is driven through the sample. The voltage drop across the sample is measured with a highly sensitive lock-in amplifier. The part of the circuit, which carries the high amplitude AC current, is indicated with solid black lines. The measurement wires, which pick-up the voltage signals, are indicated with thin gray lines. The samples are cooled to 77 K with liquid nitrogen (LN_2). Detailed explanation in the main text.

The general principle of the experiment is the following. An AC current with frequency f and current amplitude I_{AC} is driven through the sample. The loss mechanisms, in the sample, result in a voltage drop, which can be measured with voltage taps.
The high amplitude AC current is generated by amplifying a sinusoidal reference signal with an acoustic power amplifier. The output signal of the amplifier is further increased with a simple transformer. With this method, AC currents up to $I_{\mathrm{rms}} \approx 300\,\mathrm{A}$ at frequencies up to $f \approx 5\,\mathrm{kHz}$ can be achieved. The exact current amplitude through the sample is measured with a calibrated Rogowski coil. The voltage drop across the sample is in the order of a few µV, and must be recovered from the noisy environment with a highly sensitive lock-in amplifier (EG&G Instruments 7265). The power loss per cycle and unit length is then given by

$$Q = \frac{1}{l} \int_T IU \mathrm{d}t\,, \tag{8.1}$$

where l is the distance between the voltage taps.

For the case of a short HTS tape, the measurement is relatively simple. The voltage drop across the sample is directly proportional to the AC loss. For best results, the voltage is measured by using a rectangular pick-up loop ($U_{\mathrm{sample}} = -\partial\Phi/\partial t$), where the width of the loop should be a few times larger than the width of the tape.
For the case of HTS coils, the measurement is more difficult. First, the impedance of the coil increases with increasing frequency. In order to reach the required current amplitudes with the available setup, we had to reduce the input impedance of the circuit by adding compensation

capacitors (C_{comp}) in series to the coil. Depending on the measurement frequency, the value of C_{comp} was chosen so that the LC circuit is driven close to its resonance frequency. Second, the measured voltage across the coil does not only contain the loss component, but also the inductive component. In order to compensate the induced voltage in the measurement signal, a tunable compensation coil (L_{comp}) was added to the circuit, as depicted in Fig. 8.2 (b). Due to the fact that the inductive component is several orders of magnitude larger than the loss component, the tuning of the compensation coil is difficult and becomes with increasing frequency more and more challenging.

8.2.2 Transport Loss in Short Tape Samples

We have measured the low-frequency transport loss in two samples of Theva tapes with widths of 4 mm and 12 mm. The tapes have an identical critical sheet current density of $J_{\mathrm{c}} \approx 500\,\mathrm{A/cm}$ and can therefore be considered as being of the same quality. Due to their different widths, they have critical currents of 200 A and 600 A. The exact critical currents* of the tape samples, measured with a four probe method, are $I_{\mathrm{c}} = 179\,\mathrm{A}$ and $I_{\mathrm{c}} = 608\,\mathrm{A}$.
We show the AC loss of both samples in Fig. 8.3. The AC loss is plotted as a function of the applied transport current for two different frequencies. We compare the experimental result to the Norris equations in the elliptic limit (4.5) and in the thin strip limit (4.6).

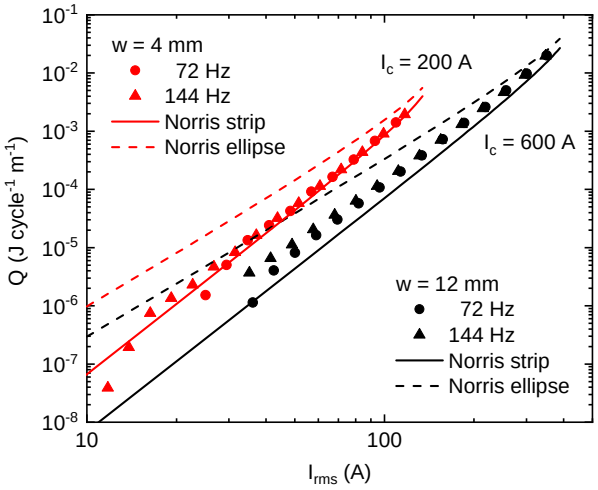

Figure 8.3: Low-frequency transport loss measurement of short HTS tape samples with $w = 4\,\mathrm{mm}$ and $w = 12\,\mathrm{mm}$. The self-field loss is purely hysteretic and follows the analytical expectation according to the Norris equations. The loss is in between the limiting cases of the ellipse approximation (4.5) and the strip approximation (4.6). The measurement proves that the tilted *ab* planes of the crystal structure in Theva tapes do not influence the AC loss. Reprinted from [164].

We observe that the measured AC loss is frequency independent, i.e. purely hysteretic, and that it agrees nicely with the analytical expectation. At large current amplitudes, the AC loss matches perfectly with the thin strip approximation. At small current amplitudes, it tends

* We note that the DC measurement of the critical current detects the weakest spot of the sample. The AC loss appears, however, already at $I \ll I_{\mathrm{c}}$ and depends mostly on the average value of I_{c}.

slightly towards the elliptical approximation. This can be explained with the argument that the current fronts penetrate the tape from the edges inwards [128]. In the low current regime most of the current flows at the edge of the tape, where the tape quality is often reduced and the shape of the tape resembles an elliptical geometry.
The measurement proves that the tilted *ab* planes of the crystal lattice in Theva tapes do not affect the validity of the Norris equation. Based on the fact that the Brandt and the Schönborg equations have been derived from the same assumptions, it is reasonable to assume that they are valid as well.

8.2.3 Transport Loss in the Fabricated WPT Coils

Now we discuss the AC loss in our fabricated HTS coils. We have performed measurements of the low-frequency transport loss in the samples #1.1 and #1.2 (1$^{\text{st}}$ Gen., non-stabilized and stabilized tape). Both samples have been measured, with and without magnetic core, at different frequencies up to 4.6 kHz. The results are presented in Fig. 8.4.
In Fig. 8.4 (a), we show the transport loss of sample #1.2 (stabilized, $f_{\text{tr,Cu}} = 6.6\,\text{kHz}$), without the magnetic core. We observe that the measured loss agrees nicely with the infinite stack approximation* [dashed line, Eq. (6.7)]. As reference, we also show the limiting cases of a single straight tape in self-field [solid line, Eq. (4.6)] and a tightly wound coil with $d = 0.4\,\text{mm}$ (dotted line, measurement data taken from [33]). The loss of our coil is in between both limiting cases. As predicted in Chap. 6, the intertape spacing reduces the loss by a factor of 10, compared to the tightly wound coil.
We further observe that the measured loss is completely independent of the frequency, i.e., of purely hysteretic nature. Only at the highest frequency of 4.6 kHz, the loss is evidently increased. Due to the fact that this measurement already approaches the transition regime of the stabilized tape $f \approx f_{\text{tr,Cu}}$, the increased AC loss could possibly be explained with the onset of eddy current losses. We repeated all measurements on sample #1.1 (non-stabilized, $f_{\text{tr,Ag}} = 60\,\text{kHz}$), and indeed, in this sample, the loss at 4.6 kHz was not increased. This allows us to rule out the possibility of a systematic error. A further increase of the measurement frequency was not possible due to technical restrictions in the available experimental setup.

In Fig. 8.4 (b), we show the influence of the magnetic core on the total loss of the coil. We compare the measurements, with and without magnetic core, to each other, and we observe that the loss contribution of the magnetic material exceeds the loss of the HTS winding by several orders of magnitude. The qualitative behavior of the complete core is identical to the result of a single ferrite segment†, which was measured in Chap. 5. The loss is frequency independent and

* We remind the reader that the infinite stack calculation depends only on one free parameter, the critical current of the tape. In the calculation, a value of $I_c = 600\,\text{A}$ was assumed. According to the tapestar measurement of the manufacturer, the actual average critical current of the utilized tape segment was $I_c \approx 550\,\text{A}$. The good agreement between measurement and calculation in Fig. 8.4 (a) was obtained without a single fit parameter.

† In Chap. 5, we have measured the power loss as a function of the magnetic flux density. Here, we show the loss as a function of the applied transport current in the coil. Because the magnetic field of the coil scales with $B \propto I$, the measured current dependence of $Q \propto I^{1.8}$ is equivalent to a field dependence of $Q \propto B^{1.8}$.

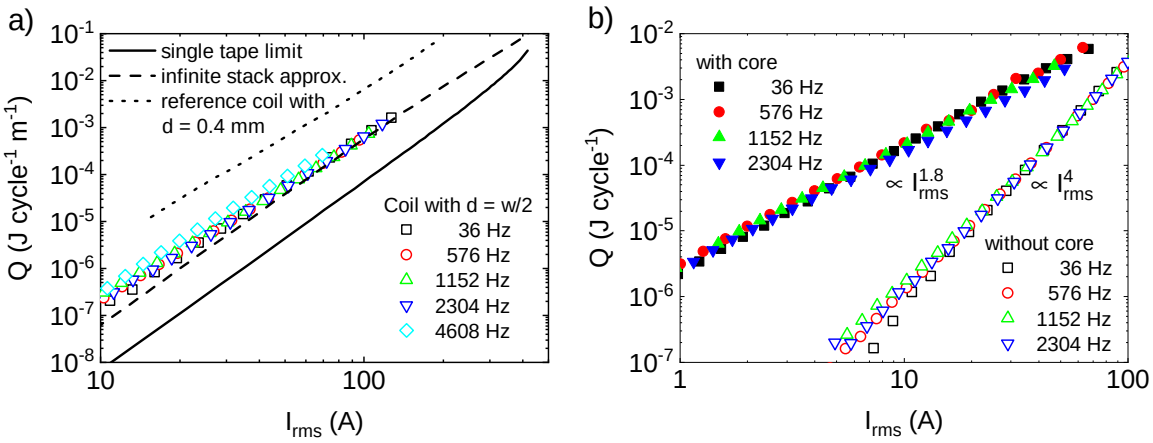

Figure 8.4: Low-frequency AC loss measurements of superconducting WPT coils. (a) Transport loss of the stabilized coil (sample #1.2), without the magnetic core. The measured loss agrees very well with the infinite stack approximation (dashed line). The limiting cases of a single tape in self-field (solid line) and of a tightly wound coil with $d = 0.4\,\mathrm{mm}$ (dotted line, data taken from [162]) are shown as reference. (b) Influence of the magnetic core on the total loss of the coil. The measurements, with and without the magnetic core, are compared to each other. The result shows that the loss contribution of the magnetic material exceeds the loss of the HTS winding by several orders of magnitude. A detailed discussion is given in the main text. Both figures are reprinted from [164].

scales with $I^{1.8}$. The absolute value, however, is much larger than expected*. This is particularly surprising, because the characterization of the single ferrite segments in Chap. 5 showed a good quantitative agreement with the literature result (comp. Fig. 5.7), and can therefore be considered to be correct. The most likely scenario to explain this large discrepancy is that the simulated magnetic flux density in the core is not correct. Due to the fact that $P_{\mathrm{core}} \propto B^{1.8}$, a factor of 5 in the simulated flux density would already explain the result. Considering the strong temperature dependence of μ_{r}, even small measurement uncertainties during the characterization of the ferrite, could have such a large effect. Another possible explanation would be that the presence of the core changes the field distribution in the complete winding and thereby increases the loss in the HTS tapes. This scenario is however unlikely, because in this case we would expect a field dependence of B^4. Additionally, it is known in literature [161, 183] that a flat magnetic core below an HTS winding normally reduces the AC loss in the winding, because it diverts the flux away from the winding. However, for our special core design, we can not neglect the possibility that the stray fields at the edges of the ferrite segments could have a negative influence on the AC loss.

Finally, we use the measured values of the AC loss to determine the Q-factors of the fabricated coils. We calculate the Q-factors based on Eq. (2.8) and we present the result as a function of

* In Chap. 6, we have implemented the experimentally determined properties of the ferrite material into our numerical simulation, and we have estimated the magnetization in the complete core at an exemplary transport current of $I_{\mathrm{rms}} = 36\,\mathrm{A}$. We have predicted a peak flux density of $B = 100\,\mathrm{mT}$ and a power loss of $Q_{\mathrm{core}} = 1 \cdot 10^{-4}\,\mathrm{J/cycle}$ ($P_{\mathrm{core}} = 10\,\mathrm{W}$ at $f = 100\,\mathrm{kHz}$). The result from Fig. 8.4 (b), shows however that the measured loss contribution of the magnetic material is by a factor of 20 larger than expected.

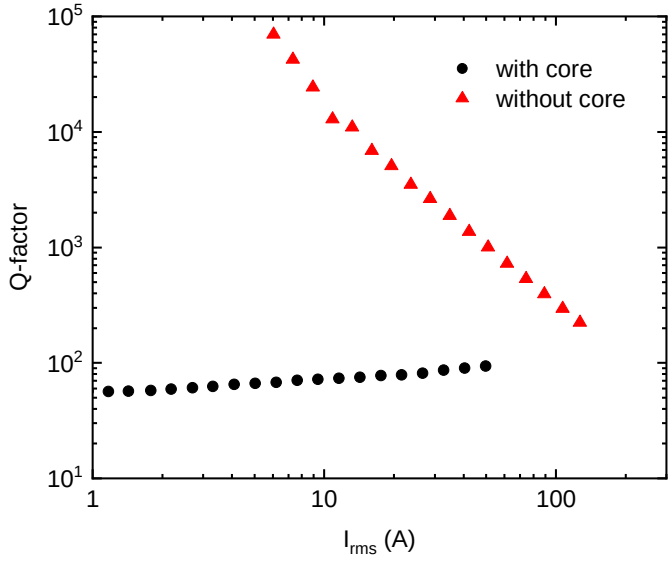

Figure 8.5: Measured quality factors of the HTS coils, with and without ferromagnetic core, in the low-frequency limit as a function of the AC transport current. Without the core, the coil is dominated by the hysteresis loss in the winding. The Q-factor is frequency independent and scales with $1/I^2$. At low current amplitudes, the Q-factor exhibits values far beyond 10000 and outperforms conventional copper coils. With the insertion of the cold ferromagnetic core, the supremacy of the superconducting winding is completely lost.

the current amplitude in Fig. 8.5.
We see that the low-frequency result agrees well with the expectations from Chap 6. The Q-factor of the HTS winding is frequency independent, scales with $1/I^2$ and exhibits values far beyond 10000 at low current amplitudes. If the core is used, the Q-factors remain below 100 and all the benefits of the superconducting coil, compared to a conventional coil, would be lost.

We summarize the main results of the presented low-frequency AC loss measurements:

- The fabricated WPT coils can indeed be operated at the required AC transport current. At $I_{\mathrm{rms}} = 36\,\mathrm{A}$, the experimentally verified (low-frequency) hysteresis loss is $Q = 1.6 \cdot 10^{-5}\mathrm{J\ cycle^{-1}m^{-1}}$ and the verified Q-factor is 1800. At lower current amplitudes, the Q-factor reaches values of 70 000.

- During our experiments at 2.3 kHz, we have applied a maximum current amplitude of $I_{\mathrm{rms}} = 117\,\mathrm{A}$, which resulted in a power dissipation of $P/l = 2.8\,\mathrm{W/m}$. Even though, this power dissipation caused a moderate amount of gas bubbles in the liquid nitrogen bath, we did not observe a coil quench. Taking this value as reference, it is evident that higher frequencies can easily be achieved as long as the current amplitude remains low. At $I_{\mathrm{rms}} = 36\,\mathrm{A}$ and $f = 100\,\mathrm{kHz}$, the resulting power dissipation (due to hysteresis loss) would be $P/l = 1.6\,\mathrm{W/m}$. If no additional eddy current loss appears, i.e. if a completely non-metallic tape was used, the self-heating of the winding would not be a problem.

- We have observed that eddy current losses start to appear slightly below the transition frequency. For the case of the stabilized coil, we have measured the onset of eddy current loss at $f = 0.7 f_{\mathrm{tr}}$. Applying this result to the non-stabilized coil, we must expect the onset of eddy current loss at $f \approx 40\,\mathrm{kHz}$.

8.3 Wireless Power Transfer Experiments

After having studied the low-frequency AC loss behavior of standalone coils, we have applied the fabricated HTS coils to our fully functional WPT system and we have performed high-power experiments. In this section, we present the characterization of the system performance. We have used the 1st Gen. coils to study the WPT system at high frequencies, and the 2nd Gen. coils to study the same system at low frequencies. The main objective of the experiments is of course to demonstrate the transmission of high power levels at excellent efficiencies. Besides that, we show that we can use our setup to study the AC loss of the transmission coils in the high-frequency regime. We have analyzed the influence of the eddy current loss in stabilized and non-stabilized pairs of coils. First, we present the experimental setup, then we show the results.

8.3.1 Experimental Method

Our experimental setup for the characterization of the WPT system, contains the complete power conversion chain from the DC source to the DC load, as introduced in Chap. 2. We show (a) the circuit diagram, and (b) a photograph of the realized setup in Fig. 8.6. All components are indicated with a color code.
The DC source (Keysight N8954A) is operated in constant voltage mode, the DC load (EA-ELR-9750-66) in constant resistance mode. The transferred power is controlled on the transmitter side by changing the DC voltage of the source. The coupled WPT coils are positioned inside a thermobox. They are operated at 77 K and are cooled with liquid nitrogen. All other components are operated at room temperature. We have used conduction cooled power capacitors (CSM Nano, CSP 120/200 and CSP 150/200) from the manufacturer Celem, to tune the resonance frequency of both LC circuits (transmitter and receiver side) to the desired value. The switching frequency of the inverter is controlled by a frequency generator (Keysight 33500B). The AC voltages and currents in the resonant circuits* are measured with an oscilloscope (Tektronix MDO3024). The DC-to-DC efficiency and the power loss of the complete system is measured with a high precision power analyzer (Yokogawa WT5000). The power analyzer is connected as shown in Fig. 8.6. The input power is measured directly before the inverter ($P_{\mathrm{in}} = I_{\mathrm{DC,in}} U_{\mathrm{DC,in}}$) and the output power directly behind the rectifier ($P_{\mathrm{out}} = I_{\mathrm{DC,out}} U_{\mathrm{DC,out}}$). The measured DC-to-DC power loss is given by $P_{\mathrm{loss}} = P_{\mathrm{in}} - P_{\mathrm{out}}$ and contains all loss components of the power conversion chain, including the transmission coils, the resonant capacitors, the inverter and the rectifier.
We have shown in [164] that we can use the full system measurement to extract the AC loss of the superconducting coils. Under the assumption that the losses in the power electronics are

* Due to resonance phenomena in the LC circuits, the AC currents ($I_{1,\mathrm{AC}}$ and $I_{2,\mathrm{AC}}$) are slightly larger than the DC currents ($I_{\mathrm{DC,in}}$ and $I_{\mathrm{DC,out}}$).

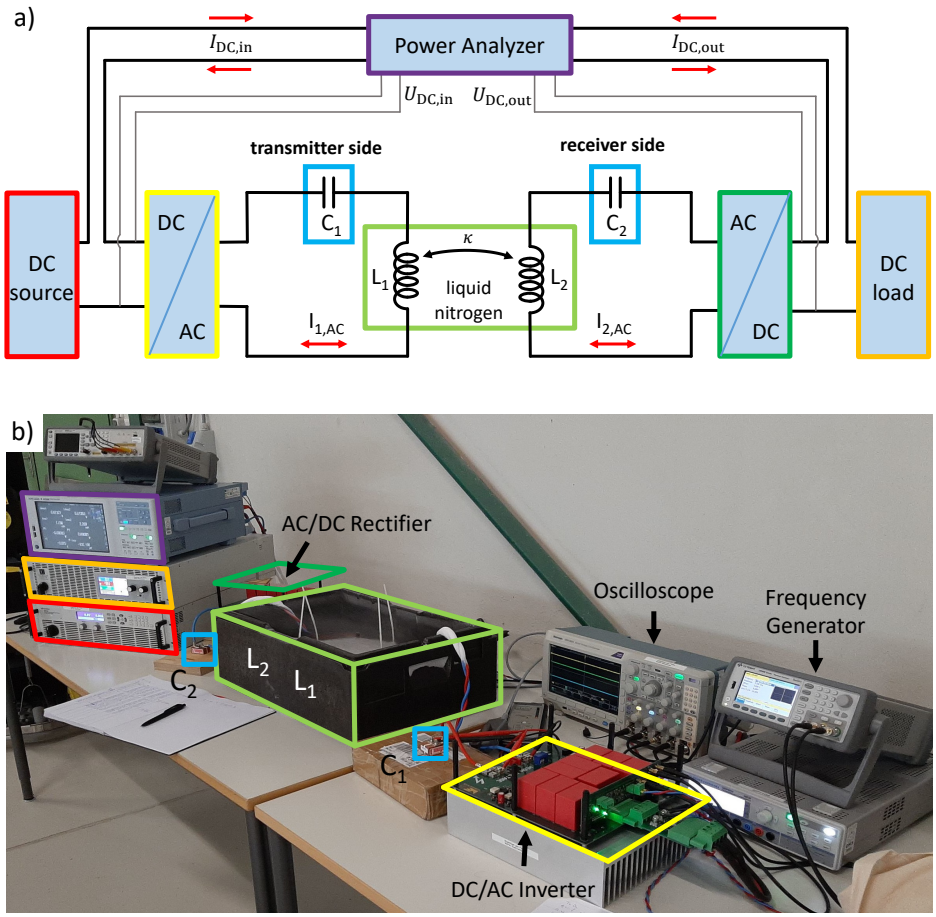

Figure 8.6: Experimental setup for the characterization of the WPT system. (a) Circuit diagram and (b) photograph of the complete power conversion chain. All components are indicated with a color code. Detailed explanation in the main text.

small, i.e., the loss of the complete WPT system is dissipated mostly in the transmission coils, the AC loss per cycle and coil is given by

$$Q = P_{\text{loss}}/(2f)\,. \tag{8.2}$$

We can compare this result (obtained with the WPT system) directly to the low-frequency AC loss measurements (obtained with the lock-in technique). The fact that the power loss in the WPT setup is measured in DC values, enables high-precision measurements of the AC loss at frequencies that are not accessible by the lock-in technique.
In reality, a small fraction of the power loss is, of course, dissipated in the room temperature electronics. The high-frequency AC loss (measured with the WPT system) should therefore only be considered as an upper limit.
In order to further increase the precision of the measurement, it would be necessary to determine the exact AC loss of all components in the power conversion chain. Such loss measurements are very challenging and could be the focus of future work. Here in this thesis, we provide at

least a small refinement of our previously reported measurement result [164]. In Sec. 2.4, we have estimated the DC conduction losses in the inverter [$P_{\mathrm{loss,inv}}$, compare Eq. (2.15)] and in the rectifier [$P_{\mathrm{loss,rect}}$, compare Eq. (2.18)]. By subtracting the calculated values of $P_{\mathrm{loss,inv}}$ and $P_{\mathrm{loss,rect}}$ from the measured DC-to-DC power loss, we expect to improve the accuracy of the measurement. With $P_{\mathrm{loss,calib}} = P_{\mathrm{loss}} - P_{\mathrm{loss,inv}} - P_{\mathrm{loss,rect}}$, the calibrated AC loss per coil per cycle is given by

$$Q = P_{\mathrm{loss,calib}}/(2f)\,, \tag{8.3}$$

8.3.2 Pre-Characterization of the WPT System

Before using our WPT system to transfer large power levels, we have performed a pre-characterization.

First, we have measured the coupling factors between the different coil pairs as a function of the transfer distance*. The results of the 1st Gen. coil pair (with and without magnetic core) and the 2nd Gen. coil pair (without magnetic core) are shown in Fig. 8.7 (a). The measurements (symbols) are compared to the results of the FEM simulation (solid lines). The agreement is excellent. We see in the figure that the target value of $\kappa = 0.5$ is reached with transmission distances of $d_{\mathrm{transfer}} = 1.5\,\mathrm{cm}$ (1st Gen. no core), $d_{\mathrm{transfer}} = 2.5\,\mathrm{cm}$ (1st Gen. with core) and $d_{\mathrm{transfer}} = 4\,\mathrm{cm}$ (2nd Gen. no core). Larger distances are of course possible if we accept lower coupling factors. With a reasonable boundary condition of $\kappa > 0.1$, we can achieve transfer distances of up to $d_{\mathrm{transfer}} = 10\,\mathrm{cm}$ with the 1st Gen. coils and $d_{\mathrm{transfer}} = 24\,\mathrm{cm}$ with the 2nd Gen. coils.
It is interesting to note that the influence of the ferromagnetic core decreases with increasing transmission distances. At $d_{\mathrm{transfer}} = 10\,\mathrm{cm}$, the magnetic core has a negligible influence on the coupling strength. Additionally, it is interesting to see that the coupling factor does not approach the value of $\kappa = 1$ for $d_{\mathrm{transfer}} \to 0$. This can be explained by the fact that the HTS winding has a width of 12mm. When the distance between transmitter and receiver coil is reduced to zero, the inner sides of the windings touch each other, but the outer sides of the windings are still separated by 24mm (twice the thickness of the winding). So the natural thickness of the winding already results in a significant flux leakage and imposes an upper limit to the magnetic coupling strength.

Second, we have measured the voltage gain of the WPT system (from source to load) as a function of the drive tone frequency. The measurement was performed with the 1st Gen. coil pair at a reduced output power of $P_{\mathrm{out}} \approx 100\,\mathrm{W}$. The resonance frequency was fixed at $f_{\mathrm{r}} = 110\,\mathrm{kHz}$ and the coupling constant was fixed to $\kappa = 0.5$. We show the results under different load conditions in Fig. 8.7 (b). The measurement (symbols) is compared to the analytical calculation according to Eq. (2.6) (solid lines). We see that the measurement agrees perfectly with the calculation and we can conclude that the analytical model in Sec. 2.3.1 is valid. The transition

* The measurement of the coupling factor was done with the typical method of determining the mutual inductance. For each measurement point, the coils are arranged in the coupled position and the inductance of L_1 is measured twice. In the first measurement, the contacts of L_2 are open ($L_{1,\mathrm{L_{2,open}}}$), in the second measurement the contacts of L_2 are shorted ($L_{1,\mathrm{L_{2,short}}}$). The coupling factor at the given distance is then $\kappa = (1-(L_{1,\mathrm{L_{2,short}}}/L_{1,\mathrm{L_{2,open}}}))^{1/2}$

from the undercoupled regime ($R_L < R_{L,opt}$), where a frequency splitting is present, into the overcoupled regime ($R_L > R_{L,opt}$), where a voltage gain around f_r appears, can be observed. The optimal working point of the system is indicated with a purple asterisk in Fig. 8.7 (b). At this working point, R_L satisfies Eq. (2.12), the system is driven slightly above f_r (ZVS condition) and the voltage gain satisfies $|G| \approx 1$.

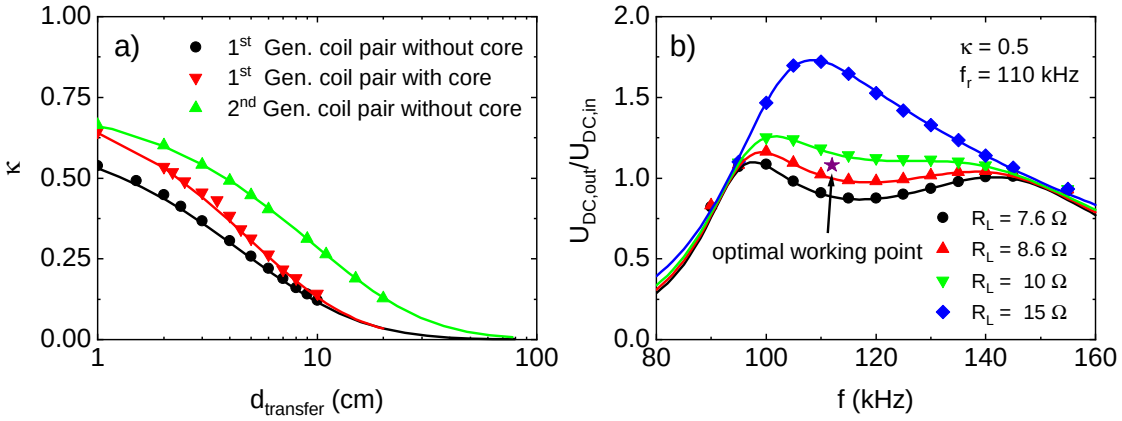

Figure 8.7: (a) Measured (symbols) and simulated (solid lines) coupling factors of the different coil pairs as a function of the distance between the coils. (b) Measured (symbols) and calculated (Eq. (2.6), solid lines) voltage gain of the WPT system from the source to the load for an exemplary system configuration. The resonance frequencies of the transmitter and the receiver circuits are fixed to $f_r = 110\,\text{kHz}$. The drive tone frequency is swept from 85 to 155 kHz to find the optimal working point (purple asterisk). Comparison of different load values shows the transition from the undercoupled into the overcoupled regime. The voltage gain of the superconducting system behaves as predicted in Chap. 2. Figure (b) is reprinted from [164].

In the following sections we will present high power experiments at different frequencies. It is important to understand that these measurements have not been obtained by simply sweeping the drive tone frequency, as shown in Fig. 8.7 (b). If the system is driven at a non-optimal working point, the system efficiency is reduced (impedance mismatch, increased resonant currents, voltage gain,...) and the actual influence of the frequency change can not be observed.
So in order to obtain comparable results at different frequencies, we must change the system in such a way, that the optimal working point shifts to the desired frequency. We have discussed the interdependencies in detail in Sec. 2.3.1. Here we repeat the most important points only briefly.
For a given coil inductance (L_1 and L_2), it is possible to shift the working point of the system (in a limited range) by physically exchanging the capacitors (C_1 and C_2). With changing resonance frequency, also the load resistance must be adapted to the new value $R_{L,opt}$ [compare Eq. (2.12)]. The change of R_L results in a change of the DC voltages at the input and at the output. For a larger frequency range, the inductances L_1 and L_2 must be replaced.
With the 1st Gen. coil pairs, we operated the system in a frequency range from $f = 89\,\text{kHz}$ to $f = 316\,\text{kHz}$. With the 2nd Gen. coil pairs between $f = 4.3\,\text{kHz}$ and $f = 33.5\,\text{kHz}$.
During all measurements, we have made sure that the system was always operated at the optimal

working point with the best possible efficiency, where the parasitic loss contributions of the measurement system are as small as possible.

8.3.3 High-Frequency Measurements with 1st Gen. Coils

In this section, we present the high-frequency performance of the WPT system. The measurements in the frequency range from $f = 89\,\mathrm{kHz}$ to $f = 316\,\mathrm{kHz}$ have been obtained with the 1st Gen. coils. We have repeated all of the following measurements on two different coil pairs. The first pair of coils (samples #1.3 and #1.4) is made of non-stabilized tape (Tape A), the second pair of coils (samples #1.2 and #1.5) is made of stabilized tape (Tape B).
We present the measured DC-to-DC efficiency of the full system at different frequencies in Fig. 8.8. We compare the results of both coil pairs to each other and we show the influence of the magnetic core.

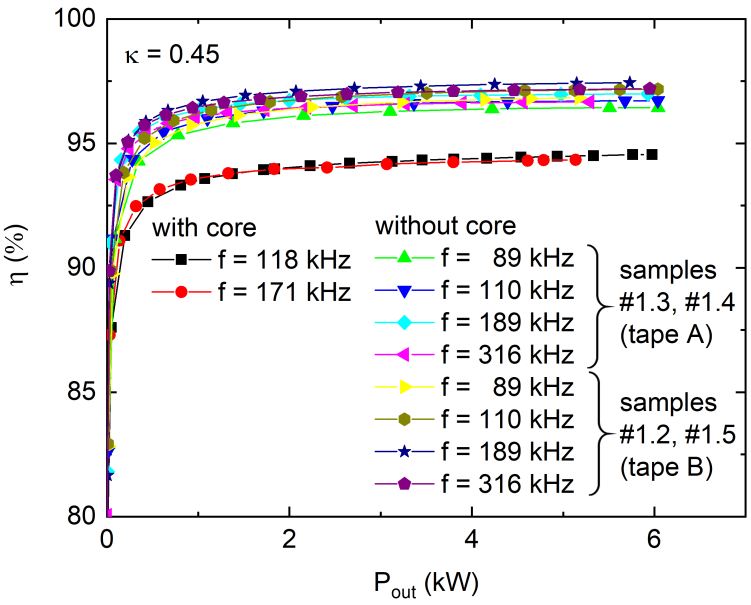

Figure 8.8: Full system DC-to-DC efficiency in the high-frequency regime (1st Gen. transmission coils). Measurements with and without magnetic core, and coil pairs with and without stabilization are compared to each other. Without the core, the efficiency is limited by eddy current losses, a frequency dependence becomes visible and the stabilized coils outperform their non-stabilized counterparts. A maximum efficiency of $\eta = 97.44\,\%$ has been achieved at an output power of 6 kW. Higher power levels were not accessible with the available setup. Reprinted from [164].

The results show that the developed WPT system enables us to transfer large power levels of $P_{\mathrm{out}} = 6\,\mathrm{kW}$ at efficiencies of up to $\eta = 97.44\,\%$. Higher power levels were not accessible with the current setup, because we reached the thermal limit of the HTS coils. The power dissipation in the coils increases with increasing output power, and at $P_{\mathrm{out}} = 6\,\mathrm{kW}$ the AC loss in the coils starts to exceed the cooling capability of the liquid nitrogen bath. As a result, the surface temperature of the HTS tapes increases and the superconductivity breaks down. A coil quench in the WPT system is clearly visible during the experiment by a spontaneous decrease of the DC-to-DC efficiency. As the quench happens on a timescale of less than 1 s, we were not able to

take measurement data during the quench. So the decrease of the efficiency is not visible in Fig. 8.8. Due to the fact that the currents in the WPT system are relatively low, the transmission coils do not take damage during the quench, if the system is depowered fast enough. In the following, we analyze the results in detail.

With the magnetic core, the efficiency is limited to $\eta = 95\,\%$ and the system performance is frequency independent. During the experiments, we observed that the liquid nitrogen bath boiled strongly. Our calibrated loss estimation [Eq. (8.3)] suggests that a total loss of 280 W has been dissipated in the nitrogen bath at an output power of $P_{\mathrm{out}} = 6\,\mathrm{kW}$. This result is consistent with the lock-in measurements, and proofs once more that the cold magnetic core causes large losses.

Without the core, the system efficiency is increased and the loss in the liquid nitrogen bath is reduced. Only at large output powers, we observed a small amount of gas bubbles. Fig. 8.8 shows that η becomes frequency dependent and the performance of both coil pairs (tape A/tape B) is very similar. We observe that the stabilized coils slightly outperform their non-stabilized counterparts. This result clarifies the high-frequency performance of HTS tapes. At 100 kHz, the eddy current loss is indeed the dominant loss mechanism in both, stabilized and non-stabilized tapes.

We gain further insight into the nature of the loss mechanisms by extracting the AC loss from the DC-to-DC measurement. With the methods described above [compare Eq. (8.2) and (8.3)], we determine the loss per cycle and coil and show the result in Fig. 8.9. In (a), the result is based on the assumption that the loss in the room temperature electronics is small and the complete loss of the WPT system is mostly dissipated in the transmission coils. In (b), the precision of the analysis is further increased by subtracting the estimated conduction loss, of the inverter and of the rectifier.

We compare all data to the results of the low-frequency lock-in measurement and to our numerical eddy current simulations.

First, we focus on Fig. 8.9 (a). For the case that the magnetic core is applied, we find good agreement between the low-frequency lock-in measurements and the high-frequency WPT experiments. This proves that our high-frequency loss measurement gives correct results and allows us to study the eddy current losses.

Without the core, we see that the power losses are strongly enhanced, compared to the low-frequency lock-in measurement. The frequency dependence of the eddy current loss is observable, the measured power loss scales with I^2 and agrees for large current amplitudes with the numerical simulation. In our previous publication [164], we have assumed that the small deviation at low current amplitudes is due to parasitic losses in the power electronics. Here, we show in Fig. 8.9 (b) that we can indeed improve the agreement in the low-current regime by subtracting the loss of the inverter and the rectifier.

The analysis of the same experiments with the non-stabilized coil pair has also given consistent results. The eddy current loss is slightly increased, and the frequency dependence is reduced, compared to the stabilized coil pair. This behavior agrees well with the expectations of the eddy current simulations. In Fig. 6.5 (Chap. 6), we have predicted that the eddy current loss at 100 kHz could be larger in the non-stabilized coil than in the stabilized coil. The reduced frequency dependence can be explained by the fact that the eddy current loss of the non-stabilized

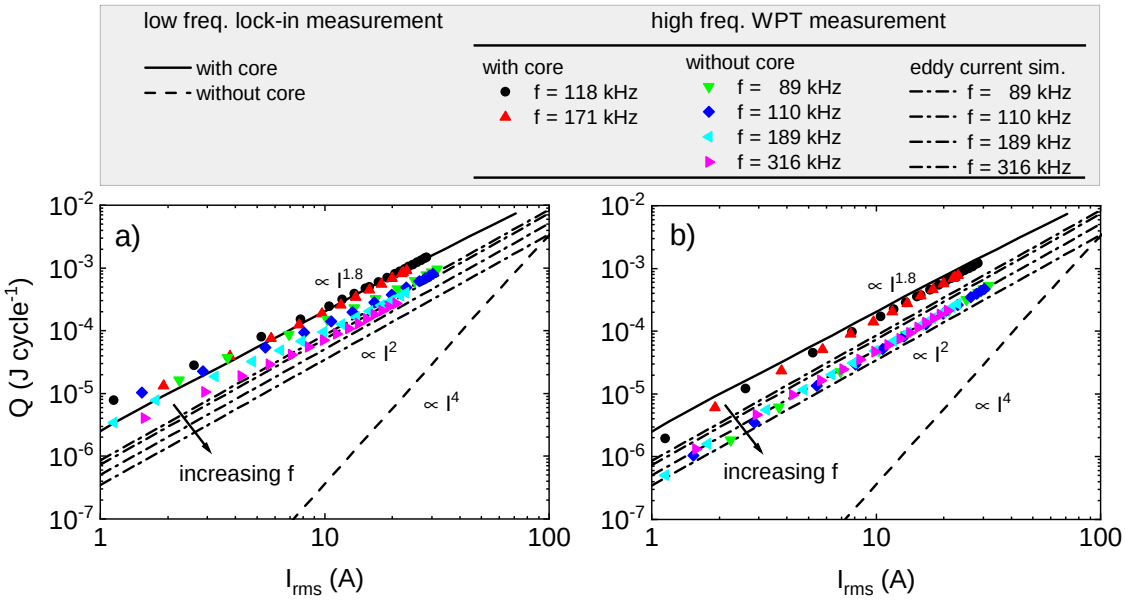

Figure 8.9: Measured high-frequency AC loss of the stabilized coil pair (Tape B), with and without magnetic core. The loss per cycle and coil is extracted from DC-to-DC loss measurements of the WPT system. In (a), the result is based on the assumption that the loss in the room temperature electronics is small and the complete loss of the WPT system is mostly dissipated in the transmission coils [Eq. (8.2)]. In (b), the precision of the result is further increased by subtracting the estimated conduction loss, of the inverter and of the rectifier [Eq. (8.3)]. All data are compared to the low-frequency lock-in measurements and to the numerical eddy current simulations. The legend is valid for (a) and (b). Explanation is given in the main text.

tape has a maximum in the studied frequency range. Nevertheless, we should mention that the quantitative agreement between measurement and simulation is less accurate for the non-stabilized coil pair than for the stabilized one. For even better simulation results, we assume that it would be necessary to apply more sophisticated simulation methods, where the interactions between the superconducting and normal conducting layers of the HTS tapes are taken into account.

The key figures of merit of the realized high-frequency WPT system are summarized in Tab. 8.1.

Despite the fact that all of the above experiments have been performed in the high-frequency regime, where the loss of the coils is dominated by eddy currents, the presented system shows an outstanding performance. The weight- and the volume-related power densities of our system exceed the best literature results (compare Tab. 1.1) by a factor of 2.8* and 2.0, respectively. Due to the fact that we did not reach the target performance of $P_{\mathrm{out}} = 11\,\mathrm{kW}$, our initial goal of reaching an area-related power density of $\alpha = 3\,\mathrm{kW/dm^2}$ was not achieved. Nevertheless, our result of $\alpha = 1.59\,\mathrm{kW/dm^2}$ exceeds all of the commercially available state-of-the-art systems and is comparable to the best literature values.

* The reported coil weight includes the coil former, the HTS winding, the spacer material between the turns, and the (non-optimized) copper contacts ($m_{\mathrm{copper}} = 448\,\mathrm{g}$). Without the copper contacts, the weight related power density is $\rho = 9.9\,\mathrm{kW/kg}$, which exceeds the literature result even by a factor of 5.

parameter	symbol	value
Output power	P_{out}	6.04 kW
Efficiency	η	97.4 %
Coupling constant	κ	0.45
DC voltage	$U_{\mathrm{DC,in}}$, $U_{\mathrm{DC,out}}$	225 V
DC current	$I_{\mathrm{DC,in}}$, $I_{\mathrm{DC,out}}$	27 A
Frequency	f	110 kHz
Coil radius	r_{out}	11 cm
Coil thickness	t_{coil}	2 cm
Coil weight	m_{coil}	1.058 kg
Area-related power density	α	1.59 kW/dm^2
Weight-related power density	ρ	5.71 kW/kg
Volume-related power density	γ	7.95 kW/dm^3

Table 8.1: Key figures of merit of the realized high-frequency WPT system with HTS coils on transmitter and receiver side.

We expect that the efficiency and the accessible power levels could be further increased by reducing the operating frequency below f_{tr}. At such low frequencies, the eddy current loss is expected to vanish and only the hysteresis loss remains.
A direct comparison of the high- and the low-frequency regime would be very interesting. Clearly, the next reasonable step would be to perform further WPT experiments with the same coil pairs as above, but this time at reduced frequencies. As discussed in Sec. 8.3.2, we face however the challenge that at lower frequencies, larger current amplitudes are required to transfer the same amount of energy. If we use the 1st Gen. coils ($L = 20.5\,\mu$H) at frequencies of $f = 10$ kHz, the optimum load resistance would be reduced to $R_{\mathrm{L,opt}} = 0.8\,\Omega$. At such a low load resistance, the required current amplitudes, to reach the same output power as above (6 kW), would be $I_{\mathrm{DC,in}} = I_{\mathrm{DC,out}} = 86$ A. Besides the fact that this value is far beyond the limitations of our WPT system, it would make the results of the high- and low-frequency regimes incomparable. The current amplitudes only remain low, if the inductance of the coil is increased. For this reason, we use in the following measurements the 2nd Gen. coils.

8.3.4 Low-Frequency Measurements with 2nd Gen. Coils

After having observed that the eddy current loss in the coils restricts us from achieving higher power levels, we studied the performance of our WPT system in the low-frequency regime. We have used the 2nd Gen. coils to perform measurements in the range from $f = 4.3$ kHz to $f = 33.5$ kHz.
Before discussing the results in detail, we remind the reader of the results from Sec. 8.2. There, we have performed low-frequency loss measurements on standalone coils (1st Gen., samples #1.1 and #1.2). We have proven that these coils can carry AC currents of $I_{\mathrm{rms}} = 70$ A at $f = 4.6$ kHz, without running into a quench. Due to the fact that the 1st Gen. coils and the 2nd Gen. coils have the same intertape spacing, they exhibit the same AC loss per unit length and it is evident that they should show an equal behavior.
This being said, it was more than surprising to observe that the performance of the 2nd Gen.

coils in the WPT system was not as good as expected. Even at the lowest frequency of 4.3 kHz, we observed a breakdown of superconductivity at a coil current of only $I_{\mathrm{rms}} = 25\,\mathrm{A}$. We have repeated all measurements on two independent coil pairs*. With the second coil pair, we were able to reach slightly higher coil currents, but the overall performance of both sample batches was similar. The result is even more puzzling when considering that the boil-off rate in the liquid nitrogen bath, which is a measure of the loss in the coils, was very low during all low-frequency experiments. In the following, we analyze the results in detail.

We present the measured DC-to-DC efficiency of the full system at different frequencies in Fig. 8.10. During each of the presented measurements, the output power was increased until one of the transmission coils quenched.

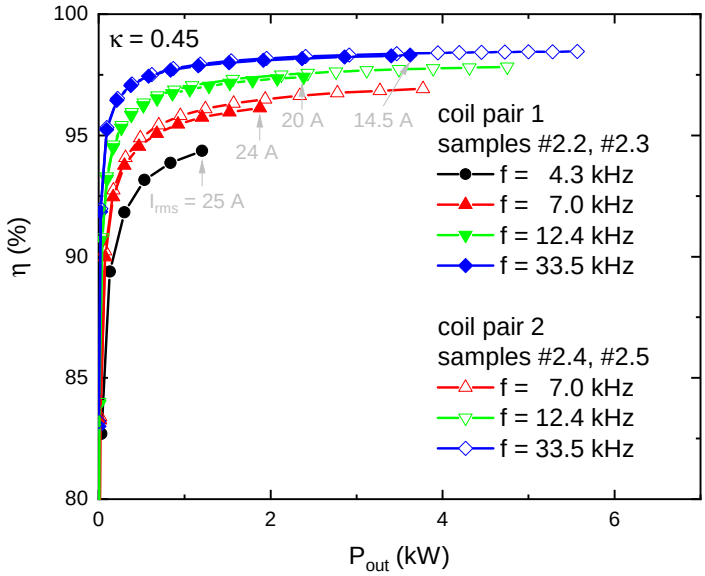

Figure 8.10: Full system DC-to-DC efficiency in the low-frequency regime (2^{nd} Gen. transmission coils). In this regime, the efficiency of the full system is dominated by the normal conducting room temperature electronics. The experimentally verified Q-factors beyond 10 000 did not increase the performance of our WPT system as expected. Large output powers could not be achieved, because the AC losses in the coils resulted in a coil quench. The current amplitudes, which triggered the quench are indicated in the figure for each frequency. The measurements have been repeated with two independent coil pairs and are reproducible. The results are discussed in detail in the main text.

We observe that the efficiency and the accessible power levels increase with increasing frequency. This result is in contradiction with the expectation and will be explained in the following.
The efficiency characteristics can most likely be explained by the losses in the normal conducting room temperature electronics. At 4.3 kHz, we have proven experimentally that the Q-factors of the coils reach values beyond 10 000. We would therefore expect the best efficiency at this very frequency, but the system actually behaves worst. We conclude that the system can only benefit from the large Q-factors, if all components are optimized for low-frequency operation. As the performance of the WPT system depends mostly on the loss per cycle, the influence of the DC

* Coil pair 1 consists of samples #2.2 and #2.3. Coil pair 2 consists of samples #2.4 and #2.5.

conduction losses in the normal conducting components increases with decreasing frequency. This limitation of the efficiency could be removed by optimizing the setup*. However, it does not explain the quench behavior of the transmission coils.

The quench in the transmission coils can only be explained with the losses that are actually dissipated *inside* the coils. In order to gain deeper understanding, we have analyzed the current amplitudes in the coils at the moment of the quench. In coil pair 1, we observed the following dependency on the frequency. At frequencies of 4.3 kHz, 7 kHz, 12.4 kHz and 33.5 kHz the quench appeared at 25.4 A, 24 A, 20 A, and 14.5 A†. In coil pair 2, the achievable current amplitudes were slightly higher. By assuming that the dominant loss mechanism is the hysteresis loss, we can estimate the heat load during the quench events with the results from Sec. 8.2 ($P/l = Qf$). We find that all four quench events in coil pair 1 happened at very similar loss rates of $P/l = 12 \pm 2\,\mathrm{mW/m}$. In coil pair 2, we have recorded only two reliable quench events, which happened at $P/l = 35 \pm 3\,\mathrm{mW/m}$. This result provides strong evidence that the hysteresis loss indeed causes the self-heating of the coils.

Considering the fact that we were able to operate the 1st Gen. coils at loss rates of $P/l = 2.8\,\mathrm{W/m}$, we study the quench behavior of the 2nd Gen. coils in more detail.

We consider two possible explanations.

The easiest explanation (and the best case scenario) would be to assume that the AC performance was limited by small damages in the fabricated coils. The verification, if this assumption is true, remains open. As we have not measured the critical currents before the WPT experiments, we can not distinguish if damages have already been present before the WPT experiments, or if the coils have been damaged during the WPT experiments‡. We can only state that all four samples have definitely been damaged after the WPT experiments. After having finished all relevant experiments, we performed DC tests on each individual sample and we observed that none of them was able to carry large DC currents. The samples #2.2 and #2.3 quenched at DC currents of 30 A and 35 A. The samples #2.4 and #2.5 quenched at DC currents of 65 A and 67 A. The DC resistance (including the contact resistance) of all samples was in the range between $R_{\mathrm{DC}} = 60\,\mu\Omega$ and $R_{\mathrm{DC}} = 220\,\mu\Omega$. The measured resistance values prove clearly that the damages, which trigger the coil quench, are very localized. The resistance per unit length of the thin silver layer is $R_{\mathrm{Ag}}^{77K} = 74\,\mathrm{m\Omega/m}$. So the total length of damaged tape in the coils is between 1 mm and 3 mm. The rest of the 30 m long winding must be superconducting to explain the low value of the measured resistance.

The second viable explanation for the early quench of the 2nd Gen. coils could possibly be found by studying the thermal properties. The coil former of the 1st Gen. coils was designed in such a way that the HTS winding is in direct contact with the liquid nitrogen. As the fluid is able

* Possible optimizations of the room temperature electronics for a successful low-frequency operation could include: Low resistance MOSFETs/IGBTs; replacement of the passive rectifier design by an active one; higher copper cross section in the cables, which connect the room temperature electronics; low loss resonance capacitors.

† At the first glance it might seem confusing that larger output powers are achieved with lower coil currents, but the result is consistent if we consider all parameter interdependencies. According to Eq. (2.12), we must increase the load resistance proportional to the frequency. With the increased load resistance, lower currents are sufficient to dissipate the same or even more output power in the load.

‡ For the detailed discussion about the challenges of non-destructive I_{c} measurements in HTS coils, we refer the reader to Sec. 8.1

to creep into the thin gaps between the HTS tape and the EPDM spacers, the heat removal occurs directly at the solid/liquid interface by evaporation of liquid nitrogen. In the 2nd Gen. coils, on the other hand, the HTS winding is embedded into the Stycast resin, the coils are completely sealed and the HTS winding is not in direct contact with the liquid nitrogen. In this case, the heat removal occurs by thermal conduction through solids and depends strongly on the properties of the involved materials. A detailed discussion of the thermal mechanisms in cryogenic environments would certainly exceed the scope of this work. Nevertheless, we conclude this section by giving a simple estimation of the heat flux rates in both coil designs. A schematic cross sectional view of both coil designs is shown in Fig. 8.11.

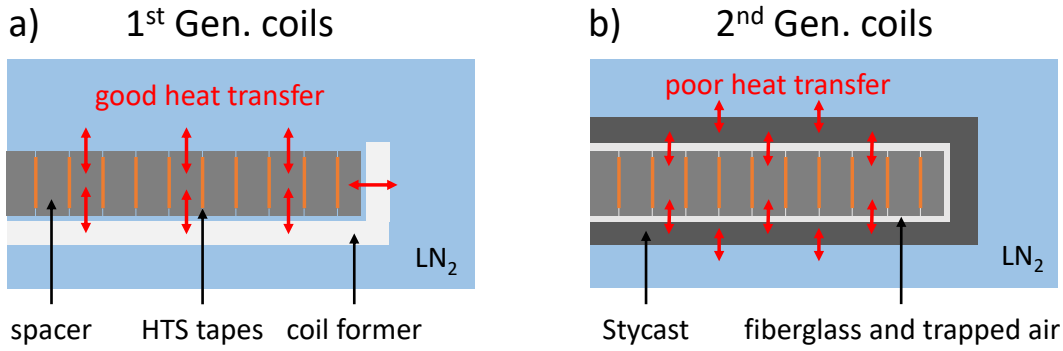

Figure 8.11: Cross sectional view of (a) 1st Gen. and (b) 2nd Gen. coils. In (a), the HTS winding is in direct contact with the liquid nitrogen bath. In (b) the HTS winding is embedded into a Stycast resin. The reduced thermal connection to the liquid nitrogen bath could explain the coil quench at low AC currents.

According to [139], a solid/liquid interface is the most efficient way to cool a sample. As long as the temperature difference between the sample and the liquid nitrogen is $\Delta T \leq 10\,\mathrm{K}$, the fluid is in the nucleate-boiling regime* and the heat flux per unit area across the interface (in units of $\mathrm{W/m^2}$) is given by $\dot{q}/A \cong 5 \times 10^2 \Delta T^{2.5}$ [139]. At an exemplary temperature difference of $\Delta T = 1\,\mathrm{K}$, the heat flux is $\dot{q}/A \approx 500\,\mathrm{W/m^2}$.
For an HTS tape of width $w = 12\,\mathrm{mm}$, the corresponding heat flux per side and unit length is $\dot{q}/l = 6\,\mathrm{W/m}$. At such large heat flux rates, the AC losses can easily be extracted from the winding. This explains the good performance of the 1st Gen. coils.

For the case of the solid/solid interface, where the heat load must be carried away by conduction through solids, the heat flux per unit area (in units of $\mathrm{W/m^2}$) is given by $\dot{q}_{\mathrm{cond}}/A = \lambda \cdot \Delta T/x$, where x is the thickness, λ is the thermal conductivity and ΔT is the temperature difference between both ends of the conducting material [139].

* At larger temperature differences $\Delta T > 10\,\mathrm{K}$, the fluid enters the film-boiling regime, where the solid surface becomes insulated with a film of gas. In this regime, the cooling efficiency is strongly reduced and ΔT jumps (at constant heat flux) to hundreds of degrees [139].

The thermal conductivities of the EPDM spacer and the Stycast resin are $\lambda_{\mathrm{EPDM}} = 0.09\,\mathrm{W/mK}$ [184] and $\lambda_{\mathrm{stycast}} = 1.01\,\mathrm{W/mK}$ [185], respectively. If we evaluate the heat flux for a characteristic length scale of $x = 5\,\mathrm{mm}$ (average length between HTS tape and liquid nitrogen) and for a temperature difference of $\Delta T = 1\,\mathrm{K}$, we find $\dot{q}_{\mathrm{cond,EPDM}}/A = 18\,\mathrm{W/m^2}$ and $\dot{q}_{\mathrm{cond,stycast}}/A = 200\,\mathrm{W/m^2}$. For an HTS tape of width $w = 12\,\mathrm{mm}$, which is in direct contact with EPDM spacer, the heat flux per side and unit length is $\dot{q}_{\mathrm{cond,EPDM}}/l = 0.2\,\mathrm{W/m}$. If the same tape is in direct contact with Stycast resin, the heat flux per side and unit length is $\dot{q}_{\mathrm{cond,stycast}}/l = 2.4\,\mathrm{W/m}$.
This calculation shows that the EPDM spacer strongly decouples the HTS winding from the cold bath. The heat flux through the EPDM spacer is reduced by a factor of 30, compared to the direct immersion into liquid nitrogen. If the HTS tape was in direct contact with the Stycast resin, i.e. if the resin would creep into the thin gaps between the HTS tape and the EPDM spacer during the molding process, the heat flux would only be reduced by a factor of 2, compared to the direct immersion into liquid nitrogen.
Due to the relatively high viscosity of the Stycast resin and due to the fact that we have applied a molding process without vacuum technique, it is evident that the HTS winding is not properly embedded into the Stycast resin in our prototypes. The complete heat load which is generated by the AC loss is therefore forced to pass through the EPDM spacers. The situation gets even worse if we consider that the thermal conduction path contains several solid/solid interfaces (HTS/EPDM, EPDM/fiberglass, fiberglass/Stycast), which could pose additional barriers. Considering these calculations, it is not surprising that the 2$^{\mathrm{nd}}$ Gen. coils quenched at heat loads of only a few mW/m.

Both of the above conclusions suggest that the accessible power levels could be increased by further optimizing the coil design. The remaining challenges are of technical nature. First, the reliability of the fabrication process must be improved, so that the fabricated prototypes do not suffer from reduced critical currents. The compatibility between the Theva tape and the Stycast resin should be checked in more detail. Second, the thermal coupling between the HTS winding and the liquid nitrogen bath must be improved, so that heat loads in the order of 1 W/m can be removed from the winding. A possible solution could be to investigate different spacer materials with increased thermal conductivity, or to establish a molding process where no spacer material at all is required, because the Stycast resin actually fills the gaps between the tapes. Finally, one could try to perforate the Stycast or to include dedicated cooling channels, such that the liquid nitrogen is in direct contact with the HTS winding. However, if we allow liquid nitrogen to flow into the coil, the HTS winding would also be exposed to external influences and might deteriorate over time. Especially during the warm-up phase of a thermal cycle, humidity from the air condenses on the cold surface of the coil. For a perforated coil, it will be particularly difficult to keep the HTS winding dry to avoid oxidation of the tape.

Chapter 9

Summary and Outlook

In this thesis, we presented the design and the operation of a WPT system with superconducting transmission coils on the transmitter and on the receiver side. For the first time, we have demonstrated that such a system is able to transfer significant power levels in the kW regime. Compared to all previous efforts, reported in literature, we have increased the accessible power levels by nearly two orders of magnitude. This result represents a large step for superconducting WPT systems and has paved the way towards a broad and interesting field of research. Even though the realized output levels of 6 kW are still relatively low, we are confident that the scalability to higher power levels will be shown in the years to come. Once the system has been scaled up, we expect that it becomes competitive to conventional technology and might have a broad impact on the landscape of future charging technology.

Summary

The main results of this thesis are summarized in the following.
In **Chap. 2**, we have introduced the fundamentals of wireless power transfer. We have given an overview of the available WPT methods, and we have shortly discussed the importance of standardization and interoperability between different WPT systems. We have clarified that we will develop our superconducting WPT systems, without restricting ourselves by the limits of the existing standards. We have reviewed the design guidelines and the properties of an inductively coupled magnetic resonant system. Thereby we have discussed, in detail, the current-voltage characteristics and the efficiency characteristics of such a system. We have presented an analytical set of equations, which describes the system behavior and allows to study the influence of the operation frequency, load conditions, quality factors and coupling factors. The requirement of optimum impedance matching in the system introduces a parameter interdependency between L, ω and κ, which forces us to operate low-inductance coils at high frequencies and vice versa. We have concluded this chapter by discussing the operation principle of the power electronics. We have estimated the power losses in the inverter and in the rectifier under the assumption that the switching losses in the semiconductor devices can be neglected.

In **Chap. 3**, we have introduced the fundamentals of superconductivity. We have classified the different types of superconductors, and we have reviewed the phenomenological model, which describes their behavior correctly, without explaining the microscopic origin. In detail, we have discussed the mechanisms of current transport in type II superconductors. We have presented the properties of commercially available HTS tapes, and we have discussed that the manufacturing processes differs from supplier to supplier. We have made the decision to use exclusively HTS tapes from the manufacturer Theva Dünnschichttechnik. For these tapes, we have analyzed the magnetic field dependence of the critical current density. We have applied a method from the literature to describe the available experimental data with analytical equations. The analytical model can now be implemented into numerical simulation software to estimate the reduction of the critical current in HTS coils. We have concluded this chapter by providing a literature review of successfully developed superconducting large scale devices. We have discussed in detail, for what reasons only very few of these applications have been accepted by the market, and which trends can be expected in the future.

In **Chap. 4**, we have introduced and discussed the different loss mechanisms in copper wires and HTS tapes. We have presented, for both conductor types, complete analytical models to calculate the AC losses under different working conditions.
For copper wires, we have reviewed and implemented a model from literature to calculate the skin- and proximity factors of solid copper wire, ideal litz wire and commercially available litz wire. The model allows to calculate the frequency dependent ohmic loss in litz wires of arbitrary cross section and litz configuration (number of strands, bundles, sub-bundles). This set of equations is a powerful tool to optimize classical copper coils regarding their cost/performance ratio and to predict their derating at elevated frequencies. We have validated the applicability of the model for conventional copper coils in Ref. [117].
For HTS tapes, we have discussed the fact that lossless current transport is only possible under DC conditions. Under AC conditions, a frequency independent hysteresis loss appears in the superconducting layer and a frequency dependent eddy current loss appears in the metallic layers of the HTS tape. Depending on the thickness and conductivities of the metal layers, a characteristic transition frequency separates the low- and the high-frequency regimes. Whereas in the low-frequency regime, the hysteresis loss dominates the total AC loss of the tape, in the high-frequency regime the eddy current loss becomes significant. In detail, we have introduced the Norris-, the Brandt- and the Schönborg equations to calculate the frequency independent hysteresis loss, which is caused by flux motion in the superconducting volume. The available equations allow an exact prediction of the losses under the action of transport current, perpendicular field and the combination of both. We have further introduced and studied the Müller equations, which allow to calculate the eddy current loss in metal strips in the direct vicinity of a superconducting layer. Our analysis has shown that the eddy current loss is small compared to the hysteresis loss, as long as $f < f_{\mathrm{tr}}$. This result is also valid for the case of thick copper stabilizers. Additionally, we have performed numerical simulations of the eddy current loss in metal strips. The performed simulations help to understand the behavior of HTS tapes at the transition from the low- into the high-frequency regime. The results suggest that the shielding currents, which are at low frequencies confined to the superconducting layer, start to migrate

into the normal conducting layers with increasing frequency.
By applying the introduced models, we were able to compare the performance of copper wires and HTS tapes. We have shown that the application of HTS tapes can be beneficial at plenty of realistic AC operating conditions. Especially in the low-frequency regime, HTS tapes outperform classical litz wires by several orders of magnitude and great improvement of the performance of WPT coils can be expected. If the superconducting hysteresis loss alone is considered, HTS tapes can even be advantageous at frequencies in the order of a few 100 kHz. If eddy current losses are considered additionally or if the current and field amplitudes are large, the application of HTS tapes at high frequencies becomes very challenging and the benefits over litz wires are lost in most cases.

In **Chap. 5**, we have presented a detailed description of the AC power loss in ferromagnetic core materials. We have introduced and discussed the properties of soft power ferrites, and we have performed an experimental low temperature characterization of a selected material (DMR95, DMEGC). We have used three different methods to study three different sample shapes.
We have seen that the saturation flux density increases with decreasing temperature. The measurement results follow the Bloch law, with a $(1 - T/T_0)^{3/2}$ dependence. Further, we have seen that the relative permeability decreases and the power loss increases with decreasing temperature. In detail, we have observed that the power loss in an anisotropic ferrite sample depends strongly on the field orientation. In parallel field, the loss is much larger than in perpendicular field. This can be explained by the fact that the effective permeability, and hence also the magnetization of the sample differs in parallel and in perpendicular field. When plotting the power loss against the internal flux density, both measurements agree with each other. Additionally, we have found that the measurements agree quantitatively with the literature result from [146]. The power loss at 77 K follows the Steinmetz equation with a field dependence of $B^{1.8}$. The Steinmetz parameters, to calculate the power loss in units of $\mathrm{W/m^3}$, are $C_\mathrm{m} = 240$, $\alpha = 1$ and $\beta = 1.8$. The intrinsic permeability at 77 K is $\mu_\mathrm{r}^{77K} = 35$.
Such a low permeability, combined with a high loss, makes it very impractical to use a ferrite core at low temperatures. Due to a lack of alternative materials, the best option for a superconducting WPT coil would be to avoid the magnetic core at all. In order to reach the required inductance and in order to reduce the stray fields of a WPT system, however, very often a magnetic core is necessary. In this case, there are only two options. Either, the additional loss of a cold core is accepted, or additional efforts must be made to develop a coil design with a warm core, where only the superconducting winding is cooled.

In **Chap 6**, we have designed and optimized the superconducting transmission coils of the WPT system. We have introduced the fundamental winding scheme of single pancake coils and we have studied the influence of the different coil parameters on the AC loss. We have introduced and applied a semianalytical and a fully analytical calculation method to estimate the superconducting AC loss in the winding. Based on this analysis, we have shown that the AC loss in the coil can be strongly reduced by introducing an intertape spacing between the individual turns of the winding. We have found the optimum number of turns to maximize the Q-factor in a limited winding space. Contrary to the common consensus in literature, we

have shown that the superconducting hysteresis loss is not necessarily a show-stopper for the application of HTS coils at significant AC frequencies. If the intertape spacing is as large as the width of the tape, the coil enters the single tape limit. In this limit, the loss in the coil is identical to the loss of an infinitely long straight tape in its self-field.
However, our results reveal also that the best possible coil design can not be chosen for our WPT system, because it would result in a very high working frequency. We have found a difficult trade-off between two risk cases. If the number of turns is chosen large, we achieve a large inductance and can operate the coil at low frequencies, but the intertape spacing becomes small and we run the risk that the AC loss causes a breakdown of superconductivity during operation. If the number of turns is chosen small, we can reduce the AC loss to the single tape limit, but the inductance is small and the coil must be operated at high frequencies, where we run the risk that eddy current losses could become significant.
We have defined two optimized winding designs (called 1st Gen. and 2nd Gen.) for the operation at high- and at low frequencies. The 1st Gen. coil is designed to achieve a high power density of $\alpha = 3\,\mathrm{kW/dm^2}$ at a frequency of 100 kHz. The 2nd Gen. coil is intended to study the performance of the WPT system at a frequency of 9 kHz. In order to obtain comparable results, both coils have the same intertape spacing and exhibit therefore the same loss per cycle and unit length. This was achieved by accepting an increased coil area and a reduced power density in the 2nd Gen. coil.
We have concluded this chapter with a short discussion about alternative simulation methods, which are typically applied in literature to determine the losses of superconducting coils. We have shown that the calculation of the exact current distribution inside the HTS tapes is not required for the WPT coils that are considered in this thesis. Because the individual turns are sufficiently spaced from each other, shielding effects can be neglected and the assumption of uniform current density reproduces the magnetic field distribution correctly. The speed-up in computation time, which comes along with this simplification, is remarkable.

In **Chap. 7**, we have presented the fabrication techniques, which have been applied to manufacture the superconducting WPT coils. In detail, we have shown how to fabricate single pancake coils with intertape spacing. For the 1st Gen. coils, we have demonstrated that functional prototypes can be realized by mounting the winding, the current feeds and the ferrite core into a 3D printed coil former. Even though this technique worked well for the 1st Gen. prototypes (10 turns, 11 cm radius), we assumed that the thermal expansion of the coil former would cause problems, if the number of turns and the coil radius is increased. Therefore, we have developed, for the 2nd Gen. coils (30 turns, 23 cm radius), a molding process, where the winding is embedded into a Stycast resin and no coil former is required. In order to verify the compatibility between Theva tapes and the Stycast resin, we have performed pretests on a short tape sample and on a small coil. Both pretests have successfully shown that only small reductions of the critical current must be expected. After the pretests, we fabricated several functional 2nd Gen. coils. The resulting coils are completely sealed and have proven sufficient stability during thermal cycling. The developed molding technique could be a promising candidate for a commercial solution.

In **Chap. 8**, we have presented the experimental results. We have characterized two of our

fabricated coils (1^{st} Gen. and 2^{nd} Gen.) under DC conditions, to verify that the fabrication process produces functional prototypes. We were able to show that both samples are perfectly superconducting and can carry large current amplitudes of $I_{tr} > 200\,A$. Furthermore, we have performed low-frequency AC loss measurements with a lock-in technique at the Institute of Electrical Engineering in Bratislava. First, we have measured the loss in short Theva tape samples, to verify that these tapes generally behave as expected. The results have shown that the tilted *ab* planes of the crystal lattice in Theva tapes do not affect the validity of the AC loss equations. Second, we have measured the AC loss in the fabricated 1^{st} Gen. coils, to verify that our calculations from Chap. 6 are correct. We have seen that the measurements indeed agree very nicely with the calculation. Compared to the loss in a tightly wound coil, the loss in our coil design, with intertape spacing, was reduced by a factor of 10. The measured low-frequency loss was purely hysteretic and at 4.6 kHz ($f \approx 0.7 f_{tr}$), we observed the onset of eddy current loss in the stabilized coil. At low current amplitudes, the Q-factor of the coils reached values of 70 000. At the desired operating current of $I_{rms} = 36\,A$ the Q-factor was 1800. We have verified that the 1^{st} Gen. coils can carry large AC currents at loss rates of $P/l = 2.8\,W/m$, without running into a quench. With these outstanding properties, the developed coil is a very promising candidate for any type of AC application and should be further investigated in future work.
Finally, we have applied the fabricated coils to our fully functional WPT system and we have performed several high-power experiments.
First, we have performed a pre-characterization of the system. We have determined the coupling factors between the different coil pairs, with and without magnetic core, and we have found the optimum working points of different system configurations.
Second, we have applied the 1^{st} Gen. coils to operate the WPT system in the high-frequency regime. We have measured the DC-to-DC efficiency at different frequencies and we have used the results to extract the high-frequency AC loss of the transmission coils. We were able to operate the system at an output power of 6 kW, with a maximum DC-to-DC efficiency of $\eta = 97.44\,\%$ ($\kappa = 0.45$). Higher power levels were not accessible, because we reached the thermal limit of the HTS coils. Our analysis showed that the loss in both, stabilized and non-stabilized coils was dominated by eddy current loss. As a consequence, the extremely high Q-factors, which have been measured at low frequencies, are not accessible in the high-frequency regime. Nevertheless, our transmission coils reached power densities of $\alpha = 1.59\,kW/dm^2$, $\rho = 5.71\,kW/kg$ and $\gamma = 7.95\,kW/dm^3$. The weight- and volume-related power densities exceed the best literature results by a factor of 2.8 and 2.0, respectively. The area-related power density exceeds all commercially available state-of-the-art systems and is comparable to the best literature values.
Last, we studied the performance of the WPT system in the low-frequency regime. By reducing the frequency below (f_{tr}), we expected to remove the eddy current loss and hoped to be able to reach larger power levels. In order to keep the current amplitudes in the system low, a decrease of the frequency has to be compensated with an increase of the coil inductance. It was therefore not possible to apply the same 1^{st} Gen. coils in both frequency regimes. In the low-frequency regime, we have applied the 2^{nd} Gen. coils. Surprisingly, we have observed an unexpected result and the verification of the low-frequency performance remains open. The thermal limit of the 2^{nd} Gen. coils was reached at even lower output powers than before. Our analysis of the quench behavior suggested that the dominating loss mechanism was hysteresis loss. Even though the 1^{st}

Gen. coils have demonstrated that they can be operated at loss rates of $P/l = 2.8\,\mathrm{W/m}$, the 2nd Gen. coils quenched at loss rates of only a few mW/m. We concluded that the reasons for the bad performance of the 2nd Gen. coils could be either small local damages in the HTS winding, or the negative influence of the Stycast resin on the thermal coupling between the HTS winding and the cold nitrogen bath. We assume that the remaining challenges are of technical nature and that the accessible power levels could be increased by further improving the coil design.

Outlook

In order to increase the accessible power levels, and to make our system competitive to conventional technology, two show-stoppers must be removed.
First, we suggest that future work should focus on improving the reliability of the fabrication process. One single local defect of the HTS tape, anywhere in the coil, is sufficient to trigger a quench. The compatibility of the Stycast resin with Theva tapes and with the applied EPDM rubber should therefore be studied in more detail.
Second, we suggest that future work should try to increase the thermal coupling between the HTS winding and the liquid nitrogen bath. A promising approach could be the application of a vacuum technique during the molding process. This would help to avoid the trapped air between the winding and the fiberglass layer and would certainly remove a heat barrier. If this is not sufficient, different spacer materials, with improved heat transfer capability, could be applied. The best results are however expected, if a new molding technique is developed, where the Stycast resin fills the gaps between the turns and no spacer material at all is required.
Considering the difficulties that come along with the molding process, another viable solution could be to further pursue the approach of the 1st Gen. coils, where the HTS winding is mounted into a mechanical support structure. It is however highly questionable if the mechanical stability and the reliability of such a coil can be improved to a sufficiently high level that it can be used in a commercial solution.
For a broad application in the industry, the efficient cooling of the coils, without losing the argument of high power density represents another key challenge. The cooling vessels cannot be made of metal. The walls of metal vessels would otherwise heat up in the magnetic field, identical to a pot on an induction stove. Additionally, the required regular access to liquid nitrogen could be an obstacle for autonomous machines.
Based on the results of this thesis, we have defined several other interesting research topics, that could be studied in future work:

- Development and characterization of completely non-metallic HTS tapes, to avoid eddy current losses at high frequencies.
- Application of filamented HTS tapes, or Roebel tapes [186], to decrease the AC loss in the HTS coils.
- Application of multiple HTS tapes in parallel, or Corc cables [187], to increase the current carrying capacity of the HTS coils.
- Development of a completely non-metallic cryostat system.

Appendix A

Simulation Methods

All magnetic field simulations in this thesis have been performed with the commercially available FEM software Ansys Maxwell (version 2018.0). Depending on the symmetry of the problem, we have used both, 2D and 3D designs. The field quantities have always been solved in the frequency domain with the built-in magnetic eddy current solver. In the following, we present all simulation setups in detail.

A.1 Simulation of the Eddy Current Loss in Infinitely Long Metal Strips

For the simulation of the eddy current loss in infinitely long m-strips (compare Sec. 4.2.2), we have used a 2D model with xy-geometry. The rectangular cross section of the m-strip is defined in the xy-plane and the simulation assumes infinite extension into z-direction. The transport current through the m-strip is defined to be zero and the perpendicular magnetic field is imposed by external boundary conditions. The electromagnetic field quantities are solved inside and outside of the m-strip. The solution region is several times larger than the dimensions of the m-strip and is limited by a balloon boundary condition, which imitates infinite extension into space. The mesh size is defined automatically by the adaptive meshing option. The solver starts with a coarse mesh, and refines the mesh size around small geometries in several simulation steps. The high aspect ratio of HTS tapes generally makes a correct meshing difficult. For extremely thin layers with $w_\mathrm{m} = 12\,\mathrm{mm}$ and $t_\mathrm{m} < 2\,\mu\mathrm{m}$, the software throws a fatal error and can not run the simulation. For $t_\mathrm{m} > 2\,\mu\mathrm{m}$, the automatic meshing option results in at least two nodes across the thickness of the strip and all parameter variations can be solved. We depict the resulting mesh grid around a thin m-strip with an aspect ratio of approximately 1:1000 in Fig. A.1 (a), and we show a close up of the edge of the m-strip in Fig. A.1 (b).
The conductor type is set to solid and the calculation of eddy currents in the m-strip is enabled. The electromagnetic field quantities are solved in a frequency range from 10 Hz to 1 MHz. The type of the frequency sweep is logarithmic with three samples per decade. The eddy current loss per unit length is given by the predefined solution parameter *SolidLoss*.

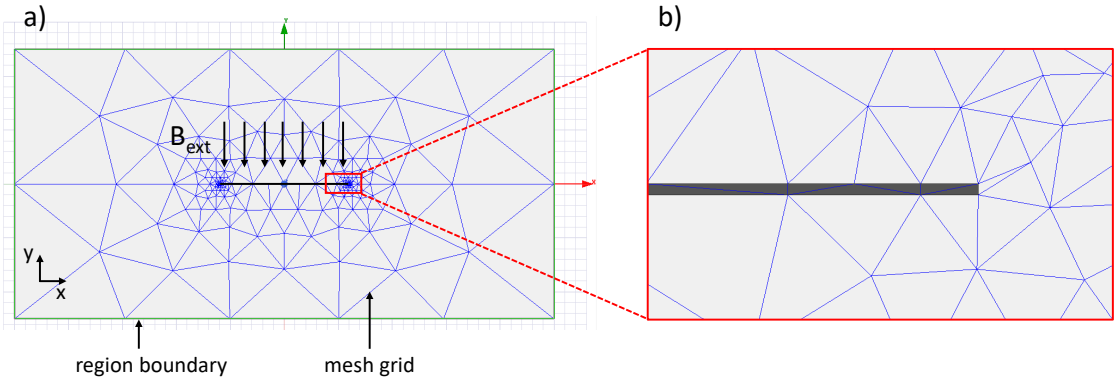

Figure A.1: Simulation of eddy current loss in m-strips under the action of external magnetic field. (a) Overview of the applied 2D model. The cross section of the m-strip is defined in the xy-plane. The simulation assumes infinite extension into z-direction. (b) The close-up of the m-strip shows that the automatic meshing option results in at least two calculation nodes across the thickness of the strip.

A.2 Simulation of Rotational Symmetric Planar WPT Coils

For the simulation of planar WPT coils, we have simplified the spiral shaped coil winding to a rotational symmetric problem of concentric turns (compare Fig. 6.1), and we have used a 2D model with rz-geometry. The cross sections of the transmitter and the receiver coils are defined in the rz-plane and the simulation assumes rotational symmetry around the z-axis. Identical to the simulation of infinitely long m-strips, the solution region is several times larger than the dimensions of the coils and is limited by a balloon boundary condition, which imitates infinite extension into space. The mesh size is defined automatically by the adaptive meshing option.
The HTS tape is implemented according to the bilayer model. The HTS layer carries the complete transport current and the metal layer carries zero transport current. The conductor type of the HTS layer is stranded (uniform current density) and the conductor type of the metal layer is solid. The calculation of eddy currents in the metal layer can be enabled or disabled. The sinusoidal currents in the transmitter and in the receiver coils are phase shifted by 90°. The geometry of the coils is completely parametrized. The number of turns, the inner coils radius, the outer coil radius, the distance between the individual turns, the distance between the coils, the thickness of the magnetic core and the permeability of the ferrite material can be systematically varied in (multi-)parameter sweeps. We show an overview of the simulation setup in Fig. A.2 (a).
The simulation setup was used for multiple purposes. First, we used it to determine the equivalent circuit parameters of the different coil variations. With the predefined solution parameters (*Matrix1.L* and *Matrix1.CplCoef*), the inductance and the magnetic coupling factor can be determined within a few seconds.
Second, we used the simulation setup to determine the hysteresis loss of the HTS coil in the low-frequency regime. Therefore, we disabled the simulation of eddy currents in the metal layers and solved the magnetic field distribution around the coils as shown in Fig. A.2 (b). We then exported the $\vec{B}$-field at the positions of the individual turns, as shown in Fig. A.2 (c). Based

on this field computation, we calculated an effective value of the perpendicular magnetic field for each turn by averaging the absolute value of the perpendicular field component across the width of the tape. We then used the Schönborg equation to calculate the hysteresis loss in each turn. The calculation has been performed in an automated post processing routine with the commercially available software Mathematica.
Last, we used the simulation setup to determine the eddy current loss of the coil in the high-frequency regime. In this regime, any effects related to superconductivity are insignificant. The eddy currents in each turn are driven by the self-field of the alternating transport current in the turn of study, and by the external field generated by all the other turns. We enabled the simulation of eddy currents in the metal layers and ran the simulations in a frequency range from 10 Hz to 1 MHz. The type of the frequency sweep was logarithmic with three samples per decade. The predefined solution parameter *SolidLoss* takes all effects into account and allows to determine the total eddy current loss of all turns simultaneously.

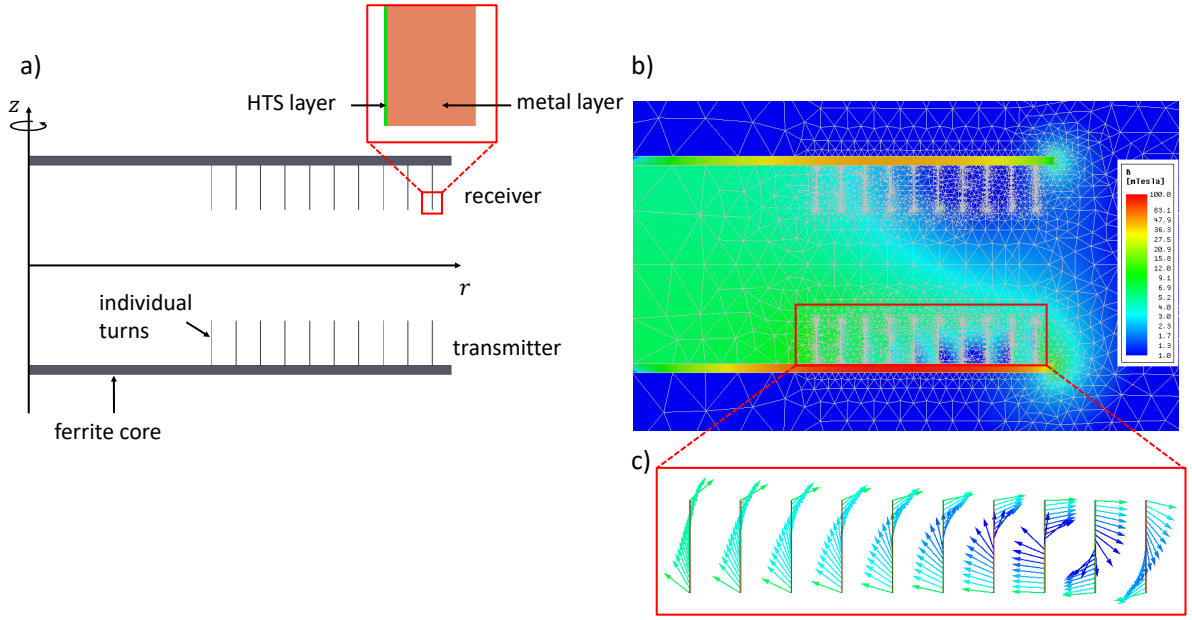

Figure A.2: Simulation of rotational symmetric planar WPT coils. (a) Overview of the applied 2D model. The cross sections of the transmitter and the receiver coils are defined in the rz-plane and the simulation assumes rotational symmetry around the z-axis. The HTS tape is implemented according to the bilayer model. The sinusoidal currents in the transmitter and in the receiver coils are phase shifted by 90°. (b) The magnetic field distribution ($|\vec{B}|$) is plotted logarithmically for the time instant $t = 0$, where the current amplitude in the transmitter coil is maximum and the current in the receiver coil is zero. The meshing grid is indicated with gray lines. The automatic meshing option results in a very fine mesh around the individual turns and around the edges of the ferrite core. (c) Detailed analysis of the $\vec{B}$-field at the positions of the individual turns.

A.3 Simulation of Non-Rotational Symmetric Planar WPT Coils

In order to optimize the weight-related power density of the coils, we introduced in Sec. 6.1 a segmented ferrite core. With such a core, the rotational symmetry of the coil is broken and

full 3D simulations became necessary. The fundamental simulation settings are identical to the rotational symmetric simulations, discussed above. Due to the 3D geometry, the required simulation time increases however strongly. We show a selection of simulated coil geometries in Fig. A.3. The subfigures (a) to (c) show design variations with increasing number of ferrite segments and (d) to (f) show design variations with increasing ferrite thickness.

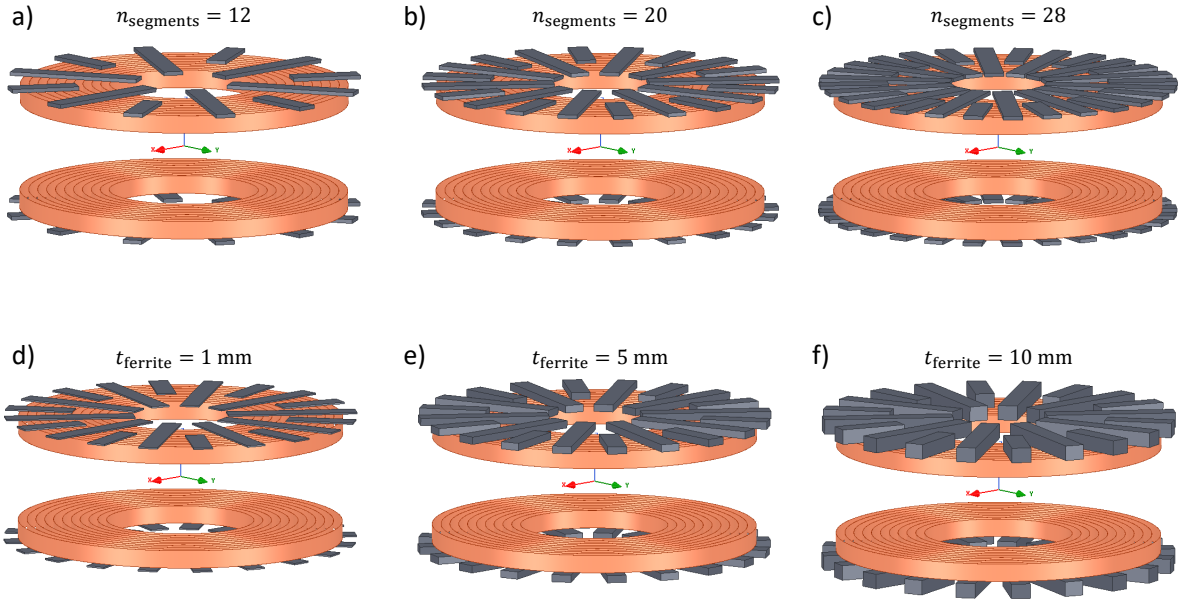

Figure A.3: Simulation of non-rotational symmetric planar WPT coils with a segmented ferrite core. In order to simulate the influence of different core geometries, the coil design was drawn in a 3D model. (a) to (c) show design variations with increasing number of ferrite segments and (d) to (f) show design variations with increasing ferrite thickness.

A.4 Comparison of Simulation Methods (uniform vs. non-uniform current density in HTS tapes)

In order to verify under which conditions the assumption of uniform current density gives accurate results we have compared our simulations to an alternative approach, which takes the exact non-uniform current distribution in the HTS layer into account. We have applied both methods to a typical benchmark problem (stack of 20 parallel HTS tapes) and we have solved the magnetic field distribution inside and outside of the stack.

The simulations, based on uniform current density, have been performed with Ansys Maxwell with the same settings as described above. For the simulations, based on non-uniform current density, we had to include the physics of superconductivity into the simulation software. This is typically achieved by implementing the $E(J)$ power law into the field formulation. As the software Ansys Maxwell is focused on classical simulation problems, the field formulation is not accessible for the normal user and we had to use a different simulation software. The multiphysics simulation suite Comsol (AC/DC module) offers the desired functionality and was therefore chosen. The exact implementation of the $E(J)$ power law into the field formulation is

based on [188] and will not be discussed here in detail. We used a reference model, which is freely available from [189].
We have varied the spacing between the individual tapes in the stack and we have compared both simulation methods. We show the results at spacings of $d = 0.2\,\mathrm{mm}$ and $d = 12\,\mathrm{mm}$ in Fig. A.4.

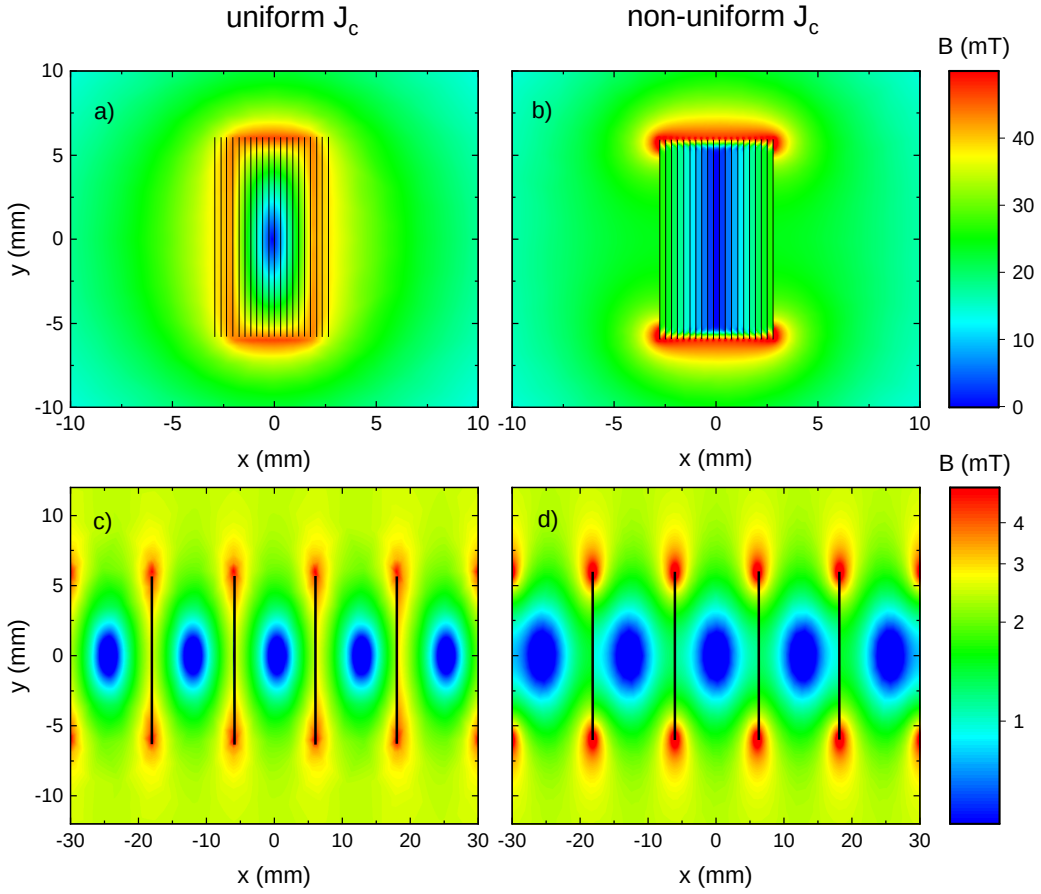

Figure A.4: Comparison of simulation results, based on uniform and non-uniform current density. The magnetic field distribution of a stack of 20 HTS tapes with a width of $w = 12\,\mathrm{mm}$ is computed with both methods for an intertape spacing of $d = 0.2\,\mathrm{mm}$ in (a) and (b), and for $d = 12\,\mathrm{mm}$ in (c) and (d). All tapes have a critical current of $I_\mathrm{c} = 600\,\mathrm{A}$ and carry the same transport current of $I_\mathrm{tr} = 50\,\mathrm{A}$. The tapes are insulated from each other and coupling currents are neglected.

For the case of tightly stacked tapes, Fig. A.4 (a) and (b) reveal that the calculation of the exact, non uniform current density is indeed necessary to obtain the correct field distribution. Due to the shielding effect of the individual tapes, the center of the stack is mostly free of field. The simplified method of assuming a uniform current density is not valid in this case.
For the case of an increased intertape spacing, Fig. A.4 (c) and (d), reveal that the calculation of the exact, non uniform current density is not necessary. In this case both simulation methods give the same result.
Due to the fact that all coil designs, discussed in this thesis, are realized with a large intertape

spacing, the determination of the exact current distribution is not required and does not bring improved accuracy for the loss calculation.
Considering the very strong increase in computation speed, which comes along with the assumption of uniform current density, our simulation method allows to systematically optimize superconducting AC machines. While state-of-the-art simulation methods typically need hours or days to solve one geometry, our method can solve hundreds of variations in the same time.

Bibliography

[1] J. Rogelj et al., "Scenarios towards limiting global mean temperature increase below 1.5 degree celsius", Nature Climate Change **8**, 325 (2018).

[2] Council of the European Union, "Taking the lead on climate change", (2020), URL `https://www.consilium.europa.eu/en/eu-climate-change/`.

[3] Frank Wienstroth, "BMW Group steps up electromobility: E-drives for half a million electrified vehicles", (July 2020), URL `https://www.press.bmwgroup.com/global/article/detail/T0310309EN/bmw-group-steps-up-electromobility:-e-drives-for-half-a-million-electrified-vehicles?language=en`.

[4] Jörn Roggenbuck, "Emden plant embarks on new era of e-mobility", (July 2020), URL `https://www.volkswagen-newsroom.com/en/press-releases/emden-plant-embarks-on-new-era-of-e-mobility-6177`.

[5] IEA, "Global EV Outlook", (2020), URL `https://www.iea.org/reports/global-ev-outlook-2020`.

[6] J. Neubauer and E. Wood, "The impact of range anxiety and home, workplace, and public charging infrastructure on simulated battery electric vehicle lifetime utility", Journal of Power Sources **257**, 12 (2014).

[7] C. T. Rim and C. Mi, *Wireless power transfer for electric vehicles and mobile devices* (John Wiley & Sons, Hoboken NJ, 2017), ISBN 9781119329053.

[8] L. Patnaik, P. S. Huynh, D. Vincent and S. S. Williamson, "Wireless Opportunity Charging as an Enabling Technology for EV Battery Size Reduction and Range Extension: Analysis of an Urban Drive Cycle Scenario", IEEE PELS Workshop on Emerging Technologies: Wireless Power Transfer (Wow) pp. 1–5 (2018).

[9] N. Borges Carvalho, A. Georgiadis, A. Costanzo, H. Rogier, A. Collado, J. A. Garcia, S. Lucyszyn, P. Mezzanotte, J. Kracek, D. Masotti, A. J. S. Boaventura, M. de las Nieves Ruiz Lavin, M. Pinuela, D. C. Yates, P. D. Mitcheson, M. Mazanek, and V. Pankrac, "Wireless Power Transmission: R&D Activities Within Europe", IEEE Transactions on Microwave Theory and Techniques **62**, 1031 (2014).

[10] D. Kim, A. Abu-Siada, and A. Sutinjo, "State-of-the-art literature review of WPT: Current limitations and solutions on IPT", Electric Power Systems Research **154**, 493 (2018).

[11] W. Jiang, S. Xu, N. Li, Z. Lin, and B. W. Williams, in *2015 IEEE 11th International Conference on Power Electronics and Drive Systems* (IEEE, 09.06.2015 - 12.06.2015), pp. 562–566, ISBN 978-1-4799-4402-6.

[12] X. Shu, W. Xiao, and B. Zhang, "Wireless Power Supply for Small Household Appliances Using Energy Model", IEEE Access **6**, 69592 (2018).

[13] "Wireless charging for a smooth and safe power transfer from shore to the ferry", (2019), URL `https://ipt-technology.com`.

[14] "Martha's Vineyard Buses Get Wirelessly Charged Up With 200-kW System", (2018), URL `https://momentumdynamics.com`.

[15] "WAVE Drayage Electrification Project", (2019), URL `https://waveipt.com`.

[16] R. Bosshard, J. W. Kolar, J. Muhlethaler, I. Stevanovic, B. Wunsch, and F. Canales, "Modeling and eta-alpha-Pareto Optimization of Inductive Power Transfer Coils for Electric Vehicles", IEEE Journal of Emerging and Selected Topics in Power Electronics **3**, 50 (2015).

[17] Xiao Yuan Chen, Jian Xun Jin, "Resonant Circuit and Magnetic Field Analysis of Superconducting Contactless Power Transfer", Proceedings of 2011 IEEE International Conference on (2011).

[18] D. W. Kim, Y. D. Chung, H. K. Kang, Y. S. Yoon, and T. K. Ko, "Characteristics of Contactless Power Transfer for HTS Coil Based on Electromagnetic Resonance Coupling", IEEE Transactions on Applied Superconductivity **22**, 5400604 (2012).

[19] W. Zuo, S. Wang, Y. Liao, and Y. Xu, "Investigation of Efficiency and Load Characteristics of Superconducting Wireless Power Transfer System", IEEE Transactions on Applied Superconductivity **25**, 1 (2015).

[20] X. Y. Chen, J. X. Jin, L. H. Zheng, and Z. H. Wu, "A Rotary-Type Contactless Power Transfer System Using HTS Primary", IEEE Transactions on Applied Superconductivity **26**, 1 (2016).

[21] R. Narayanamoorthi and A. V. Juliet, "Capacitor-Less High-Strength Resonant Wireless Power Transfer Using Open Bifilar Spiral Coil", IEEE Transactions on Applied Superconductivity **29**, 1 (2019).

[22] W. Li, T. W. Ching, C. Jiang, T. Wang, and Le Sun, "Quantitative Comparison of Wireless Power Transfer Using HTS and Copper Coils", IEEE Transactions on Applied Superconductivity **29**, 1 (2019).

[23] H. Yu, G. Zhang, L. Jing, Q. Liu, W. Yuan, Z. Liu, and X. Feng, "Wireless Power Transfer With HTS Transmitting and Relaying Coils", IEEE Transactions on Applied Superconductivity **25**, 1 (2015).

[24] H. K. Kang, Y. D. Chung, and S. W. Yim, "Conceptual design of contactless power transfer into HTS receiver coil using normal conducting resonance antenna", Cryogenics **63**, 209 (2014).

[25] R. Inoue, D. Miyagi, M. Tsuda, and H. Matsuki, "High-Efficiency Transmission of a Wireless Power Transmission System for Low-Frequency Using REBCO Double-Pancake Coils", IEEE Transactions on Applied Superconductivity **27**, 1 (2017).

[26] G. Zhang, H. Yu, L. Jing, J. Li, Q. Liu, and X. Feng, "Wireless Power Transfer Using High Temperature Superconducting Pancake Coils", IEEE Transactions on Applied Superconductivity **24**, 1 (2014).

[27] O. Foote, "A Review of High-Power Wireless Power Transfer", 2017 IEEE Transportation Electrification Conference and Expo (ITEC) pp. 234–340 (2017).

[28] R. Bosshard, "Multi-Objective Optimization of Inductive Power Transfer Systems for EV Charging", Phd thesis, ETH Zurich (2015).

[29] Conductix-Wampfler GmbH, "Fahrerloses Transportsystem - Hochzeitsband", (2006), URL `https://www.conductix.de/sites/default/files/downloads/REF9000-0009-D_Fahrerlose_Transportsysteme_GM_China.pdf`.

[30] Su Y. Choi, Beom W. Gu, Seog Y. Jeong, and Chun T. Rim, "Advances in Wireless Power Transfer Systems for Roadway-Powered Electric Vehicles", IEEE Journal of Emerging and Selected Topics in Power Electronics **3**, 18 (2015).

[31] Su Y. Choi, Seog Y. Jeong, Beom W. Gu, Gyu C. Lim, and Chun T. Rim, "Ultraslim S-Type Power Supply Rails for Roadway-Powered Electric Vehicles", IEEE TRANSACTIONS ON POWER ELECTRONICS (2015).

[32] C. C. Mi, G. Buja, S. Y. Choi, and C. T. Rim, "Modern Advances in Wireless Power Transfer Systems for Roadway Powered Electric Vehicles", IEEE Transactions on Industrial Electronics **63**, 6533 (2016).

[33] B. Goeldi, J. Tritschler, and S. Reichert, "Measurement Results of a 22 kW Bidirectional Inductive Charger", Proceedings of PCIM Europe (2015).

[34] R. Bosshard and J. W. Kolar, "Multi-Objective Optimization of 50 kW/85 kHz IPT System for Public Transport", IEEE Journal of Emerging and Selected Topics in Power Electronics **4**, 1370 (2016).

[35] Jason Pries, Veda Prakash Galigekere, Omer C. Onar, Gui-jia Su, Randy Wiles, Larry Seiber, Jonathan Wilkins, Saeed Anwar, Shenli Zou, "Coil Power Density Optimization and Trade-off Study for a 100kW Electric Vehicle IPT Wireless Charging System", Proceedings of IEEE Energy Conversion Congress pp. 1196–1201 (2018).

[36] Veda Prakash Galigekere, Jason Pries, Omer C. Onar, Gui-Jia Su, Saeed Anwar, Randy Wiles, Larry Seiber, and Jonathan Wilkins, "Design and Implementation of an Optimized

100 kW Stationary Wireless Charging System for EV Battery Recharging", Proceedings of IEEE Energy Conversion Congress pp. 3587–3592 (2018).

[37] BRUSA Elektronik AG, "ICS - Inductive Charging System ICS115", (2020), URL https://www.brusa.biz/fileadmin/Diverses/Download/Datenblaetter/BRUSA_DB_EN_ICS115.pdf.

[38] Wiferion, "Induktives Laden mit 12kW – etaLINK 12000",, URL https://www.wiferion.com/produkte/etalink-12000-induktives-batterie-laden-12-kw-leistung.

[39] INTIS, "Fachartikel - INTIS Demonstrations- und Kundenprojekte", (2020), URL http://www.intis.de/downloads.html.

[40] Timo Pape, "Kompakter & schneller: FIA veröffentlicht Gen3-Spezifikationen für künftiges Formel-E-Auto", (2019), URL https://e-formel.de/news/kompakter-schneller-fia-veroeffentlicht-gen3-spezifikationen-fuer-kuenftiges-formel-e-auto-7892.html.

[41] Daniel Schuster, "Audi präsentiert e-tron FE07 für Formel-E-WM", (2020), URL https://www.audi-mediacenter.com/de/audi-in-der-formel-e-2021-13376.

[42] THEVA Dünnschichttechnik GmbH:, "Rekord-Performance bei HTS-Bandleitern: Stromtragfähigkeit von 1350 Ampere erreicht", (2020), URL https://www.theva.de/wp-content/uploads/2020/08/200811_PI_Theva_RekordHTS_De_F.pdf.

[43] M. Staines, K. P. Thakur, L. S. Lakshmi, and S. Rupp, "Screening of Eddy Current Loss in Metal Layers of Coated HTS Conductors", IEEE Transactions on Applied Superconductivity **19**, 2851 (2009).

[44] B. Shen, J. Li, J. Geng, L. Fu, X. Zhang, C. Li, H. Zhang, Q. Dong, J. Ma, and T. A. Coombs, "Investigation and comparison of AC losses on stabilizer-free and copper stabilizer HTS tapes", Physica C: Superconductivity and its Applications **541**, 40 (2017).

[45] R. Inoue, D. Miyagi, M. Tsuda, and H. i. Matsuki, "Magnetization Loss Characteristics of a GdBCO Tape in kHz Frequency Band", IEEE Transactions on Applied Superconductivity **28**, 1 (2018).

[46] P. Zhou, G. Ma, and L. Quéval, "Transition frequency of transport ac losses in high temperature superconducting coated conductors", Journal of Applied Physics **126**, 063901 (2019).

[47] Nikola Tesla, "World System of Wireless Transmission of Energy", Telegraph and Telegraph Age (1927).

[48] Nikola Tesla, *Experiments with Alternate Currents of Very High Frequency and Their Application to Methods of Artificial Illumination* (Wildside Press, 1891), ISBN 978-0809501625.

[49] W. C. Brown, “The History of Power Transmission by Radio Waves”, IEEE Transactions on Microwave Theory and Techniques **32** (1984).

[50] R. S. Mroczkowski, “A perspective on connector reliability”, Proceedings of the 50th IEEE Holm Conference on Electrical Contacts (2004).

[51] Naval Sea Systems Command, “Connectors - Failure Mechanisms and Anomalies”„ URL `https://www.navsea.navy.mil/Portals/103/Documents/NSWC_Crane/SD-18/PDFs/Products/Connectors/ConnectorsFailure.pdf`.

[52] G. Lee, H. Gwak, Y.-S. Kim, and W.-S. Park, in *2013 IEEE Wireless Power Transfer (WPT)* (IEEE, 15.05.2013 - 16.05.2013), pp. 100–102, ISBN 978-1-4673-5010-5.

[53] S. Ditze, A. Endruschat, T. Schriefer, A. Rosskopf, and T. Heckel, in *2016 IEEE International Symposium on Circuits and Systems (ISCAS)* (IEEE, 22.05.2016 - 25.05.2016), pp. 1622–1625, ISBN 978-1-4799-5341-7.

[54] Y. D. Chung, C. Y. Lee, D. W. Kim, H. Kang, Y. G. Park, and Y. S. Yoon, “Conceptual Design and Operating Characteristics of Multi-Resonance Antennas in the Wireless Power Charging System for Superconducting MAGLEV Train”, IEEE Transactions on Applied Superconductivity **27**, 1 (2017).

[55] Angelos Amditis, “Final Report Summary - FABRIC (FeAsiBility analysis and development of on-Road chargIng solutions for future electric vehiCles)”„ URL `https://cordis.europa.eu/project/id/605405/reporting`.

[56] “IPT Rail 85 kHz - Product Overview”, (2020), URL `https://ipt-technology.com/product-ipt-rail-85-khz/`.

[57] “A framework for wireless power technologies”, (2018), URL `https://wi-charge.com/downloads/`.

[58] “Guidelines for Limiting Exposure to Electromagnetic Fields (100 kHz to 300 GHz)”, Health physics **118**, 483 (2020).

[59] Wireless Power Consortium, “The Qi Wireless Power Transfer System Power Class 0 Specification”, (2017), URL `https://www.wirelesspowerconsortium.com/knowledge-base/specifications/download-the-qi-specifications.html`.

[60] Cliff Raskind, “Wireless Charging Tracking & Trends - Strategy Analytics”, WPC Annual Meeting (2020).

[61] Wireless Power Consortium, “MEDIUM POWER WIRELESS CHARGING: EMERGING APPLICATIONS, CONSIDERATIONS AND OPPORTUNITIES”, (2020), URL `https://www.wirelesspowerconsortium.com/medium-power/`.

[62] Wireless Power Consortium, “KI CORDLESS KITCHEN: FROM CONCEPT TO INDUSTRY STANDARD”, (2020), URL `https://www.wirelesspowerconsortium.com/kitchen/`.

[63] Society of Automotive Engineers, “Standard J2954”, (2017).

[64] Society of Automotive Engineers, “SAE J2954/2 Wireless Power Transfer & Alignment for Heavy Duty Applications”, (2020), URL https://www.sae.org/standards/content/j2954/2/.

[65] R. L. Steigerwald, “A comparison of half-bridge resonant converter topologies”, IEEE Transactions on Power Electronics **3**, 174 (1988).

[66] Y. H. Sohn, B. H. Choi, E. S. Lee, G. C. Lim, G.-H. Cho, and C. T. Rim, “General Unified Analyses of Two-Capacitor Inductive Power Transfer Systems: Equivalence of Current-Source SS and SP Compensations”, IEEE Transactions on Power Electronics **30**, 6030 (2015).

[67] D. Huwig, S. Horras, and P. Wambsgans, “Grundlagen der induktiven Energieübertragung, Qi-Standard und Systemdesign”, Elektronik wireless power congress (2012).

[68] C.-S. Wang, G. A. Covic, and O. H. Stielau, “Power Transfer Capability and Bifurcation Phenomena of Loosely Coupled Inductive Power Transfer Systems”, IEEE Transactions on Industrial Electronics **51**, 148 (2004).

[69] Eberhard Waffenschmidt, “Limitation of inductive power transfer”, 13th European Conference on Power Electronics and Applications (2009).

[70] R. W. Erickson and D. Maksimović, *Fundamentals of Power Electronics* (Kluwer Academic Publishers, Boston, MA, 2004), second edition ed., ISBN 9780792372707, URL http://dx.doi.org/10.1007/b100747.

[71] B. Andreycak, “Zero Voltage Switching Resonant Power Conversion”„ URL https://www.ti.com/lit/ml/slup089/slup089.pdf.

[72] R. Gross and A. Marx, *Festkörperphysik*, De Gruyter Studium (De Gruyter, Berlin and Boston, 2014), 2nd ed., ISBN 978-3-11-035870-4.

[73] Infineon, “Silicon Carbide Schottky Diode IDW40G120C5B”„ URL https://www.infineon.com/cms/de/product/power/diodes-thyristors/coolsic-schottky-diodes/idw40g120c5b/.

[74] J. Bardeen, L. N. Cooper, and and J. R. Schrieffer, “Theory of Superconductivity”, Phys. Rev. **108**, 1175 (1957).

[75] D. Larbalestier, “High-Tc superconducting materials for electric power applications”, Nature **414**, 368 (2001).

[76] J. E. Kunzler, E. Buehler, F. S. L. Hsu, and J. H. Wernick, “Superconductivity in Nb3Sn at High Current Density in a Magnetic Field of 88 kgauss”, Phys. Rev. Lett. **6**, 89 (1961).

[77] J. G. Bednorz and K. A. Müller, “Possible highTc superconductivity in the Ba−La−Cu−O system”, Zeitschrift für Physik B Condensed Matter **64**, 189 (1986).

[78] M. K. Wu, J. R. Ashburn, C. J. Torng, P. H. Hor, R. L. Meng, L. Gao, Z. J. Huang, Y. Q. Wang, and and C. W. Chu, "Superconductivity at 93 K in a new mixed-phase Y-Ba-Cu-O compound system at ambient pressure", Phys. Rev. Lett. **58**, 908 (1987).

[79] L. E. Conroy, A. N. Chirstensen, and J. Bottiger, "Preparation and Characterization of High-T, Oxides. YBaCuO, and REBaCuO", Acta Chemica Scandinavica **41**, 501 (1987).

[80] H. Maeda, Y. Tanaka, M. Fukutomi, T. Asano, K. Togano, H. Kumakura, M. Uehara, S. Ikeda, K. Ogawa, S. Horiuchi, and Y. Matsui, "New high-Tc superconductors without rare earth element", Physica C: Superconductivity **153-155**, 602 (1988).

[81] A. Schilling, M. Cantoni, J. D. Guo, and H. R. Ott, "Superconductivity above 130 K in the Hg–Ba–Ca–Cu–O system", Nature **363**, 56 (1993).

[82] F. London and H. London, "The electromagnetic equations of the supraconductor", Porc. Roy. Soc. Lond. **A149** (1935).

[83] L. N. Cooper, "Bound Electron Pairs in a Degenerate Fermi Gas", Phys. Rev. **104**, 1189 (1956).

[84] Paul Seidl, ed., *Applied Superconductivity, Handbook on Devices and Applications* (Wiley, 2015).

[85] A. I. Larkin and Y. N. Ovchinnikov, "Pinning in type II superconductors", Journal of Low Temperature Physics **34**, 409 (1979).

[86] F. Grilli, E. Pardo, A. Stenvall, D. N. Nguyen, W. Yuan, and F. Gomory, "Computation of Losses in HTS Under the Action of Varying Magnetic Fields and Currents", IEEE Transactions on Applied Superconductivity **24**, 78 (2014).

[87] Theva Dünnschichttechnik GmbH, "Datasheet: THEVA PRO-LINE: HTS wires produced by e-beam PVD",.

[88] S. Kalsi, *Applications of high temperature superconductors to electric power equipment* (Wiley and IEEE Press, Hoboken N.J. and Piscataway NJ, 2011), ISBN 0470167688.

[89] Theva Dünnschichttechnik GmbH, "Datasheet: THEVA PRO-LINE: HTS wire, general properties",.

[90] Y. B. Kim, C. F. Hempstead, and and A. R. Strnad, "Critical Persistent Currents in Hard Superconductors", Phys. Rev. Lett **9** (1962).

[91] F. Gömöry, J. Šouc, M. Vojenčiak, and B. Klinčok, "Phenomenological description of flux pinning in non-uniform high-temperature superconductors in magnetic fields lower than the self-field", Superconductor Science and Technology **20**, S271 (2007).

[92] E. Pardo, M. Vojenčiak, F. Gömöry, and J. Šouc, "Low-magnetic-field dependence and anisotropy of the critical current density in coated conductors", Superconductor Science and Technology **24**, 065007 (2011).

[93] A. Bergen, R. Andersen, M. Bauer, H. Boy, M. t. Brake, P. Brutsaert, C. Bührer, M. Dhallé, J. Hansen, H. ten Kate, J. Kellers, J. Krause, E. Krooshoop, C. Kruse, H. Kylling, M. Pilas, H. Pütz, A. Rebsdorf, M. Reckhard, E. Seitz, H. Springer, X. Song, N. Tzabar, S. Wessel, J. Wiezoreck, T. Winkler, and K. Yagotyntsev, "Design and in-field testing of the world's first ReBCO rotor for a 3.6 MW wind generator", Superconductor Science and Technology **32**, 125006 (2019).

[94] M. Zhang, J.-H. Kim, S. Pamidi, M. Chudy, W. Yuan, and T. A. Coombs, "Study of second generation, high-temperature superconducting coils: Determination of critical current", Journal of Applied Physics **111**, 083902 (2012).

[95] V. Grosse, "private communication", (17.10.2018).

[96] Werner Prusseit, "Superconductor Industry in Germany: Status and Perspectives", IEEE/CSC & ESAS EUROPEAN SUPERCONDUCTIVITY NEWS FORUM **4** (2008).

[97] P. Tixador, M. Bauer, C.-E. Bruzek, A. Calleja, G. Deutscher, B. Dutoit, F. Gomory, L. Martini, M. Noe, X. Obradors, M. Pekarcikova, and F. Sirois, "Status of the European Union Project FASTGRID", IEEE Transactions on Applied Superconductivity **29**, 1 (2019).

[98] Heinz Arnold, "Münchens Super-Projekt: Das längste supraleitende Kabel der Welt", Markt & Technik (01.06.2019).

[99] G. Klaus, W. Nick, H.-W. Neumuller, G. Nerowski, and W. McCown, "Advances in the development of synchronous machines with high-temperature superconducting field winding at Siemens AG", Proceedings of IEEE Power Engineering Society p. 7 pp (2006).

[100] S. S. Kalsi, K. Weeber, H. Takesue, C. Lewis, H.-W. Neumueller, and R. D. Blaugher, "Development status of rotating machines employing superconducting field windings", Proceedings of the IEEE **92**, 1688 (2004).

[101] K. Sivasubramaniam, T. Zhang, M. Lokhandwalla, E. T. Laskaris, J. W. Bray, B. Gerstler, M. R. Shah, and J. P. Alexander, "Development of a High Speed HTS Generator for Airborne Applications", IEEE Transactions on Applied Superconductivity **19**, 1656 (2009).

[102] R. Fair, C. Lewis, J. Eugene, and M. Ingles, "Development of an HTS hydroelectric power generator for the hirschaid power station", Journal of Physics: Conference Series **234**, 032008 (2010).

[103] M. Leghissa, B. Gromoll, J. Rieger, M. P. Oomen, H.-W. Neumueller, R. Schlosser, H. Schmidt, W. Knorr, M. Meinert, and U. Henning, "Development and application of superconducting transformers", Physica C **372-376**, 1688 (2002).

[104] C. S. Weber, C. T. Reis, D. W. Hazelton, S. W. Schwenterly, M. J. Cole, J. A. Demko, E. F. Pleva, S. Mehta, T. Golner, and N. Aversa, "Design and Operational Testing of a 5/10-MVA HTS Utility Power Transformer", IEEE Transactions on Appiled Superconductivity **15**, 2210 (2005).

[105] N. D. Glasson, M. P. Staines, Z. Jiang, and N. S. Allpress, "Verification Testing for a 1 MVA 3-Phase Demonstration Transformer Using 2G-HTS Roebel Cable", IEEE Transactions on Applied Superconductivity **23**, 5500206 (2013).

[106] J. Bock, F. Breuer, H. Walter, S. Elschner, M. Kleimaier, R. Kreutz, and M. Noe, "CURL 10: Development and Field-Test of a 10 kV/10 MVA Resistive Current Limiter Based on Bulk MCP-BSCCO 2212", IEEE Transactions on Appiled Superconductivity **15**, 1955 (2005).

[107] H.-P. Kraemer, W. Schmidt, H. Cai, B. Gamble, D. Madura, T. MacDonald, J. McNamara, W. Romanosky, G. Snitchler, N. Lallouet, F. Schmidt, and S. Ahmed, "Superconducting Fault Current Limiter for Transmission Voltage", Physics Procedia **36**, 921 (2012).

[108] Y. Xin, W. Z. Gong, H. Hong, X. Y. Niu, J. Y. Zhang, A. R. Ren, and B. Tian (AIP Publishing LLC, 2014), AIP Conference Proceedings, pp. 1042–1048.

[109] J. A. Demko, I. Sauers, D. R. James, M. J. Gouge, D. Lindsay, M. Roden, J. Tolbert, D. Willen, and C. T. Nielsen, "Triaxial HTS Cable for the AEP Bixby Project", IEEE Transactions on Applied Superconductivity **17**, 2047 (2007).

[110] H. Yumura, Y. Ashibe, H. Itoh, M. Ohya, M. Watanabe, T. Masuda, and C. S. Weber, "Phase II of the Albany HTS Cable Project", IEEE Transactions on Applied Superconductivity **19**, 1698 (2009).

[111] J. F. Maguire, F. Schmidt, S. Bratt, T. E. Welsh, J. Yuan, A. Allais, and F. Hamber, "Development and Demonstration of a HTS Power Cable to Operate in the Long Island Power Authority Transmission Grid", IEEE Transactions on Applied Superconductivity **17**, 2034 (2007).

[112] M. Stemmle, F. Merschel, M. Noe, and A. Hobl, in *2013 IEEE International Conference on Applied Superconductivity and Electromagnetic Devices* (IEEE, 25.10.2013 - 27.10.2013), pp. 323–326, ISBN 978-1-4799-0070-1.

[113] M. Albach, *Induktivitäten in der Leistungselektronik* (Springer Fachmedien Wiesbaden, Wiesbaden, 2017), ISBN 978-3-658-15080-8.

[114] A. Rosskopf, E. Bar, and C. Joffe, "Influence of Inner Skin- and Proximity Effects on Conduction in Litz Wires", IEEE Transactions on Power Electronics **29**, 5454 (2014).

[115] D. Barth, B. Klaus, and T. Leibfried, in *2017 IEEE Wireless Power Transfer Conference (WPTC)* (IEEE, 10.05.2017 - 12.05.2017), pp. 1–4, ISBN 978-1-5090-4585-3.

[116] H. Rossmanith, M. Doebroenti, M. Albach, and D. Exner, "Measurement and Characterization of High Frequency Losses in Nonideal Litz Wires", IEEE Transactions on Power Electronics **26**, 3386 (2011).

[117] C. Utschick, C. Merz, and C. Som, "AC Loss Behavior of Wireless Power Transfer Coils", 2019 IEEE Wireless Power Transfer Conference (WPTC) pp. 120–125 (2019).

[118] S. Stavrev, B. Dutoit, N. Nibbio, and L. Lay, "Eddy current self-field loss in Bi-2223 tapes with a.c. transport current", Physica C **307**, 105 (1998).

[119] C. P. Bean, "Magnetization of Hard Superconductors", Phys. Rev. Lett **8**, 250 (1962).

[120] W. T. Norris, "Calculation of hysteresis losses in hard superconductors carrying ac: isolated conductors and edges of thin sheets", Journal of Physics D: Applied Physics **3** (1970).

[121] E. H. Brandt, M. V. Indenbom, and A. Forkl, "Type-II Superconducting Strip in Perpendicular Magnetic Field", EPL **22**, 735 (1993).

[122] N. Schönborg, "Hysteresis losses in a thin high-temperature superconductor strip exposed to ac transport currents and magnetic fields", Journal of Applied Physics **90**, 2930 (2001).

[123] F. Grilli and S. P. Ashworth, "Measuring transport AC losses in YBCO-coated conductor coils", Superconductor Science and Technology **20**, 794 (2007).

[124] B. Shen, C. Li, J. Geng, X. Zhang, J. Gawith, J. Ma, Y. Liu, F. Grilli, and T. A. Coombs, "Power dissipation in HTS coated conductor coils under the simultaneous action of AC and DC currents and fields", Superconductor Science and Technology **31**, 075005 (2018).

[125] R. Inoue, D. Miyagi, M. Tsuda, and H. Matsuki, "AC Loss Characteristics in kHz frequency band of a High Temperature Superconductor Coil for a Wireless Power Transmission System", IEEE Transactions on Applied Superconductivity p. 1 (2017).

[126] S. P. Ashworth, M. Maley, M. Suenaga, S. R. Foltyn, and J. O. Willis, "Alternating current losses in YBa2Cu3O7−x coated conductors on technical substrates", Journal of Applied Physics **88**, 2718 (2000).

[127] F. Grilli and A. Kario, "How filaments can reduce AC losses in HTS coated conductors: a review", Superconductor Science and Technology **29**, 083002 (2016).

[128] E. Pardo, F. Gömöry, J. Šouc, and J. M. Ceballos, "Current distribution and ac loss for a superconducting rectangular strip with in-phase alternating current and applied field", Superconductor Science and Technology **20**, 351 (2007).

[129] J. Ogawa, M. Shiokawa, M. Ciszek, and O. Tsukamoto, "AC losses in YBCO coated conductors carrying AC transport currents in perpendicular AC external magnetic field", IEEE Transactions on Appiled Superconductivity **13**, 1735 (2003).

[130] Y. Mawatari and K. Kajikawa, "Hysteretic ac loss of superconducting strips simultaneously exposed to ac transport current and phase-different ac magnetic field", Applied Physics Letters **90**, 022506 (2007).

[131] D. N. Nguyen, P. V. P. S. S. Sastry, D. C. Knoll, G. Zhang, and J. Schwartz, "Experimental and numerical studies of the effect of phase difference between transport current and perpendicular applied magnetic field on total ac loss in Ag-sheathed (Bi,Pb)2Sr2Ca2Cu3Ox tape", Journal of Applied Physics **98**, 073902 (2005).

[132] M. Vojenčiak, J. Šouc, J. M. Ceballos, F. Gömöry, B. Klinčok, E. Pardo, and F. Grilli, "Study of ac loss in Bi-2223/Ag tape under the simultaneous action of ac transport current and ac magnetic field shifted in phase", Superconductor Science and Technology **19**, 397 (2006).

[133] K.-H. Müller, "AC power losses in flexible thick-film superconducting tapes", Physica C: Superconductivity **281**, 1 (1997).

[134] J. Passi and M. Lahtinen, "AC Losses in Multifilamentary Bi-2223/Ag Superconducting Tapes", IEEE TRANSACTIONS ON MAGNETICS **32** (1996).

[135] N. Magnusson, "Semi-empirical model of the losses in HTS tapes carrying AC currents in AC magnetic fields applied parallel to the tape face", Physica C **349**, 225 (2001).

[136] M. Majoros, L. Ye, A. V. Velichko, T. A. Coombs, M. D. Sumption, and E. W. Collings, "Transport AC losses in YBCO coated conductors", Superconductor Science and Technology **20**, S299 (2007).

[137] P. Zhou, C. Wang, H. Qian, L. Queval, Z. Luo, Y. Deng, J. Li, Y. Li, and G. Ma, "Frequency-dependent Transport AC Losses of Coated Superconductors up to Tens of Kilohertz", IEEE Transactions on Applied Superconductivity p. 1 (2019).

[138] J. Lu, E. S. Choi, and H. D. Zhou, "Physical properties of Hastelloy C-276 at cryogenic temperatures", Journal of Applied Physics **103**, 064908 (2008).

[139] J. W. Ekin, *Experimental techniques for low-temperature measurements: Cryostat design, material properties, and superconductor critical-current testing* (Oxford Univ. Press, Oxford, 2007), reprinted ed., ISBN 9780198570547.

[140] H. Zhang, M. Yao, K. Kails, P. Machura, M. Mueller, Z. Jiang, Y. Xin, and Q. Li, "Modelling of Electromagnetic Loss in HTS Coated Conductors over a Wide Frequency Band", Superconductor Science and Technology (2019).

[141] J. B. Goodenough, "Summary of losses in magnetic materials", IEEE Transactions on Magnetics **38**, 3398 (2002).

[142] E. C. Snelling, *Soft Ferrites - Properties and Applications* (Newnes-Butterworth, 1969).

[143] C. Steinmetz, "On the law of hysteresis", Proceedings of the IEEE **72**, 197 (1984).

[144] G. F. Dionne, "Microwave Ferrites for Cryogenic Applications", Le Journal de Physique IV **07**, C1 (1997).

[145] S. S. Gerber, "Performance of high-frequency high-flux magnetic cores at cryogenic temperatures", Proceedings of IECEC pp. 249–254 (2002).

[146] J. H. Claassen, "Inductor Design for Cryogenic Power Electronics", IEEE Transactions on Appiled Superconductivity **15**, 2385 (2005).

[147] G. F. Dionne, "Properties of ferrites at low temperatures (invited)", Journal of Applied Physics **81**, 5064 (1997).

[148] I. M. Obaidat, B. Issa, B. A. Albiss, and Y. Haik, "Temperature Dependence of Saturation Magnetization and Coercivity in Mn 0.5 Zn 0.5 Gd 0.02 Fe 1.98 O 4 Ferrite Nanoparticles", IOP Conference Series: Materials Science and Engineering **92**, 012012 (2015).

[149] M. Daniil, H. M. Fonda, and M. A. Willard, "Crystal Structure and Magnetic Properties of (Fe,Si,Al)-Based Nanocomposite Magnets Designed for Cryogenic Applications", Metallurgical and Materials Transactions E **2**, 139 (2015).

[150] M. Daniil, K. E. Knipling, H. M. Fonda, and M. A. Willard, "Non-equilibrium materials design: a case study of nanostructured soft magnets for cryogenic applications", New Journal of Physics **16**, 055016 (2014).

[151] M. A. Willard and T. M. Heil, "Cryogenic hysteretic loss analysis for (Fe,Co,Ni)–Zr–B–Cu nanocrystalline soft magnetic alloys", Journal of Applied Physics **101**, 09N113 (2007).

[152] S. Geprägs, "Electric-field control of magnetization in multifunctional hybrid devices", Phd thesis, Technische Universität München (2011).

[153] J. Šouc, F. Gömöry, and M. Vojenčiak, "Calibration free method for measurement of the AC magnetization loss", Superconductor Science and Technology **18**, 592 (2005).

[154] I. Mészáros, "Magnetization curve modelling of soft magnetic alloys", Journal of Physics: Conference Series **268**, 012020 (2011).

[155] F. Bloch, "Zur Theorie des Ferromagnetismus", Zeitschrift für Physik **61**, 206 (1930).

[156] W. A. Roshen and D. E. Turcotte, "Planar inductors on magnetic substrates", IEEE Transactions on Magnetics **24**, 3213 (1988).

[157] M. Budhia, G. A. Covic, and J. T. Boys, "Design and Optimization of Circular Magnetic Structures for Lumped Inductive Power Transfer Systems", IEEE Transactions on Power Electronics **26**, 3096 (2011).

[158] K.-H. Müller, "AC losses in stacks and arrays of YBCO/hastelloy and monofilamentary Bi-2223/Ag tapes", Physica C: Superconductivity **312**, 149 (1999).

[159] J. R. Clem, J. H. Claassen, and Y. Mawatari, "AC losses in a finite Z stack using an anisotropic homogeneous-medium approximation", Superconductor Science and Technology **20**, 1130 (2007).

[160] F. Grilli, V. Zermeno, M. Vojenciak, E. Pardo, A. Kario, and W. Goldacker, "AC Losses of Pancake Coils Made of Roebel Cable", IEEE Transactions on Applied Superconductivity **23**, 5900205 (2013).

[161] G. Liu, G. Zhang, and L. Jing, "Experimental and numerical study of the frequency-dependent transport ac losses of the YBa2CuO7 coil with and without flux diverters", Superconductor Science and Technology **32**, 055002 (2019).

[162] F. Gomory, J. Souc, E. Pardo, E. Seiler, M. Soloviov, L. Frolek, M. Skarba, P. Konopka, M. Pekarcikova, and J. Janovec, "AC Loss in Pancake Coil Made From 12 mm Wide REBCO Tape", IEEE Transactions on Applied Superconductivity **23**, 5900406 (2013).

[163] I.-S. Jeong, H.-S. Choi, and M.-S. Kang, "Application of the Superconductor Coil for the Improvement of Wireless Power Transmission Using Magnetic Resonance", Journal of Superconductivity and Novel Magnetism **28**, 639 (2015).

[164] C. Utschick, C. Som, J. Souc, V. Grose, F. Gomory, and R. Gross, "Superconducting Wireless Power Transfer Beyond 5 kW at High Power Density for Industrial Applications and Fast Battery Charging", IEEE Transactions on Applied Superconductivity **31**, 5500110 (2021).

[165] F. Grilli, "Numerical modeling of HTS applications", IEEE Transactions on Applied Superconductivity p. 1 (2016).

[166] J. Šouc, E. Pardo, M. Vojenčiak, and F. Gömöry, "Theoretical and experimental study of AC loss in high temperature superconductor single pancake coils", Superconductor Science and Technology **22**, 015006 (2009).

[167] E. Pardo, "Modeling of coated conductor pancake coils with a large number of turns", Superconductor Science and Technology **21**, 065014 (2008).

[168] M. D. Ainslie, V. M. Rodriguez-Zermeno, Z. Hong, W. Yuan, T. J. Flack, and T. A. Coombs, "An improved FEM model for computing transport AC loss in coils made of RABiTS YBCO coated conductors for electric machines", Superconductor Science and Technology **24**, 045005 (2011).

[169] L. Prigozhin and V. Sokolovsky, "Computing AC losses in stacks of high-temperature superconducting tapes", Superconductor Science and Technology **24**, 075012 (2011).

[170] E. Pardo and F. Grilli, "Numerical simulations of the angular dependence of magnetization AC losses: coated conductors, Roebel cables and double pancake coils", Superconductor Science and Technology **25**, 014008 (2012).

[171] V. M. R. Zermeño and F. Grilli, "3D modeling and simulation of 2G HTS stacks and coils", Superconductor Science and Technology **27**, 044025 (2014).

[172] W. Yuan, A. M. Campbell, and T. A. Coombs, "A model for calculating the AC losses of second-generation high temperature superconductor pancake coils", Superconductor Science and Technology **22**, 075028 (2009).

[173] K. Kajikawa, K. Funaki, K. Shikimachi, N. Hirano, and S. Nagaya, "Numerical and theoretical evaluations of AC losses for single and infinite numbers of superconductor strips with direct and alternating transport currents in external AC magnetic field", Physica C: Superconductivity and its Applications **470**, 1321 (2010).

[174] J. Pitel, A. Korpela, J. Lehtonen, and P. Kovac, "Mathematical model of voltage–current characteristics of Bi(2223)/Ag magnets under an external magnetic field", Superconductor Science and Technology **15**, 1499 (2002).

[175] E. Pardo, A. Sanchez, and C. Navau, "Magnetic properties of arrays of superconducting strips in a perpendicular field", Physical Review B **67**, 368 (2003).

[176] F. Grilli, S. P. Ashworth, and S. Stavrev, "Magnetization AC losses of stacks of YBCO coated conductors", Physica C: Superconductivity **434**, 185 (2006).

[177] C. Barth, N. Bagrets, K.-P. Weiss, C. M. Bayer, and T. Bast, "Degradation free epoxy impregnation of REBCO coils and cables", Superconductor Science and Technology **26**, 055007 (2013).

[178] H. Song, P. Brownsey, Y. Zhang, J. Waterman, T. Fukushima, and D. Hazelton, "2G HTS Coil Technology Development at SuperPower", IEEE Transactions on Applied Superconductivity **23**, 4600806 (2013).

[179] H.-J. Shin, K. L. Kim, Y. H. Choi, O. J. Kwon, S. Hahn, Y. Iwasa, and H. G. Lee, "Effects of Impregnating Materials on Thermal and Electrical Stabilities of the HTS Racetrack Pancake Coils Without Turn-to-Turn Insulation", IEEE Transactions on Applied Superconductivity **23**, 7700404 (2013).

[180] U. Besi Vetrella, G. Celentano, M. Marchetti, G. Messina, L. Morici, P. Sabatino, R. Viola, and A. Della Corte, "HTS Coils Fabrication From Commercial 2G YBCO Tapes: Measurements and Simulation", IEEE Transactions on Applied Superconductivity **24**, 1 (2014).

[181] S. Zanegin, N. Ivanov, D. Shishov, I. Shishov, K. Kovalev, and V. Zubko, "Manufacturing and Testing of AC HTS-2 Coil for Small Electrical Motor", Journal of Superconductivity and Novel Magnetism **33**, 355 (2020).

[182] S. Safran, J. Souc, and F. Gömöry, "AC loss characterization of single pancake BSCCO coils by measured different methods", Physica C: Superconductivity and its Applications **541**, 45 (2017).

[183] E. Pardo, J. Šouc, and M. Vojenčiak, "AC loss measurement and simulation of a coated conductor pancake coil with ferromagnetic parts", Superconductor Science and Technology **22**, 075007 (2009).

[184] Resogoo, "Technisches Datenblatt: Zellkautschuk EPDM"„ URL `https://www.resogoo.com/mediafiles/158067158227584721591.pdf`.

[185] Henkel, "Technical Data Sheet: LOCTITE STYCAST 2850FT"„ URL `http://tds.henkel.com/tds5/Studio/ShowPDF/243%20NEW-EN?pid=STYCAST%202850FT&format=MTR&subformat=HYS&language=EN&plant=WERCS`.

[186] R. A. Badcock, N. J. Long, M. Mulholland, S. Hellmann, A. Wright, and K. A. Hamilton, "Progress in the Manufacture of Long Length YBCO Roebel Cables", IEEE Transactions on Applied Superconductivity **19**, 3244 (2009).

[187] D. C. van der Laan, J. D. Weiss, C. H. Kim, L. Graber, and S. Pamidi, "Development of CORC ® cables for helium gas cooled power transmission and fault current limiting applications", Superconductor Science and Technology **31**, 085011 (2018).

[188] V. M. Rodriguez-Zermeno, N. Mijatovic, C. Traeholt, T. Zirngibl, E. Seiler, A. B. Abrahamsen, N. F. Pedersen, and M. P. Sorensen, "Towards Faster FEM Simulation of Thin Film Superconductors: A Multiscale Approach", IEEE Transactions on Applied Superconductivity **21**, 3273 (2011).

[189] V. Zermeno, "2-D homogeneous model to estimate AC losses in coated conductor stacks and coils",, URL `www.htsmodelling.com`.

List of Publications

1. C. Utschick, C. Som, J. Souc, V. Große, F. Gömöry, and R. Gross, "Superconducting Wireless Power Transfer Beyond 5 kW at High Power Density for Industrial Applications and Fast Battery Charging", IEEE Transactions on Applied Superconductivity **31**, 5500110 (2021).
   DOI: 10.1109/TASC.2021.3056195

2. C. Utschick, C. Merz and C. Som, "AC Loss Behavior of Wireless Power Transfer Coils", IEEE Wireless Power Transfer Conference (WPTC), pp. 120-125 (2019).
   DOI: 10.1109/WPTC45513.2019.9055524

3. "Contactless high performance power transmission", Technical University of Munich, Corporate Communications Center, press release (2021)
   URL: https://www.tum.de/nc/en/about-tum/news/press-releases/details/36486/.

Acknowledgments

I want to thank all the people who contributed to this thesis and supported me during the last three years, especially

- Prof. Dr. Rudolf Gross, for supervising my thesis, for his invaluable advice and for his deep interest in my research topic. Our extensive scientific discussions have truly guided me in the last three years.
- Cem Som, for giving me the opportunity to do my thesis at the company Würth Elektronik eiSos and for sharing his vast knowledge on various topics concerning wireless power transfer.
- Andreas Unterreitmeier, for his continuous support in the lab and for realizing the 11 kW power electronics. Without his effort, this thesis would not have been possible.
- Dr. Veit Grosse, for providing excellent support regarding the development of HTS coils, for giving me access to the labs of the company Theva Dünnschichttechnik and for always organizing liquid nitrogen, when needed.
- Dr. Fedor Gömöry and Jan Souc, for giving me the possibility of performing measurements at the Institute of Electrical Engineering in Bratislava. Their experience with AC loss measurements helped significantly to understand the behavior of the transmission coils.
- Dr. Mathias Opel, for providing access to the SQUID magnetometer at the Walther-Meissner-Institute and for supporting me during the measurements.
- The complete Wireless Power Team at the company Würth Elektronik eiSos, for being great office-mates.
- Our working students, Stefan, Jonas, Daniel, Christian, Michael and Bazil, for having always a fun time in the lab and at the coffee machine.
- All my friends, for their constant support and encouragement. Most importantly, for staying in regular contact during the second half of this thesis, which was marked by the corona crisis and social distancing.

- My family, for supporting me throughout my whole life, for believing in me and in my dreams and for their unconditional support, whenever I needed it.
- Anna, for her love and support during all ups and downs of the past years. Most importantly for her endless patience and her ability of cheering me up and motivating me. It wouldn't be the same without you!